# Mechanical response of soft matter systems: biological tissues and wrinkled structures

Sijie Tong

A Dissertation
Presented to the Faculty
of Princeton University
in Candidacy for the Degree
of Doctor of Philosophy

Recommended for Acceptance
by the Department of
Mechanical and Aerospace Engineering
Adviser: Andrej Košmrlj

September 2023

# Abstract

In recent years, there has been a significant growing interest in developing an understanding of soft materials due to their rich properties and wide applications. In this thesis, I present a study on the mechanical response properties of two types of soft materials: biological tissues and wrinkled structures.

Epithelial tissues consist of thousands of cells moving in groups, which is commonly simulated with the vertex model. While previous studies have predominantly focused on the rheological properties of the vertex model at long time scales, we systematically study the full dynamic range of shear and bulk rheology and measure the dynamical response modulus. We show that the linear viscoelastic responses of the vertex model could be mapped to standard spring-dashpot models.

I further develop a normal mode formalism that can describe the linear viscoelastic properties of soft elastic systems with different microscopic dissipation mechanisms. We show that the motion along each normal mode behaves independently as a spring-dashpot model. The values of spring constants and dashpot viscosity can be naturally related to the corresponding eigenvalues and the projection of external driving without the need for any fitting parameter. Besides, we show that extending the vertex model to include different types of microscopic dissipation mechanisms has non-trivial effects on rheology, which are captured by the normal mode formalism.

Finally, I present the linear response theory of wrinkled structures. While the formation and evolution of wrinkled structures are well understood, more is needed to know how they respond to external forces and achieve their functions in various applications. Thus, we study how wrinkled structures respond to infinitesimal surface forces. We find that the linear response diverges near the onset of the wrinkling instability, which can be understood in terms of the dominant characteristic Fourier mode of wrinkles. However, the coupling between different Fourier modes becomes

significant away from the instability threshold, affecting the mechanical response of the structures.

# Acknowledgements

Here are acknowledgements.

To.

# Contents

# List of Tables

# List of Figures

# Chapter 1

# Introduction

Soft materials, including polymers, gels, foams, liquid crystals, and biological tissues, typically consist of building blocks much larger than atoms or molecules but smaller than the system's overall size. Due to the weak interaction of building blocks at the mesoscopic level, soft materials exhibit rich mechanical and rheological properties such as low elastic moduli, nonlinearity, dissipative, slow dynamics, and sensitivity to external stimuli [1, 2, 3, 4]. Over the last few decades, not only has there been a great interest in studying the complex behaviors of various kinds of soft materials but the rich properties of soft materials have been exploited to develop a wide range of applications. One way to probe soft materials' properties is to measure their response to external stimuli. For example, the rheometer measures fluids' response to applied forces to study their rheology. Besides, many soft matter applications involve response to external stimuli from environments to achieve specific functions. Thus, it is crucial to understand the response properties of soft materials.

This work focuses on understanding the mechanical response properties of two types of soft materials: biological tissues and wrinkled structures. An introduction of the specific problem and perspective is given below.

## 1.1 Mechanical response of biological tissues

The development and maintenance of tissues requires close coordination of mechanical and biochemical signaling [5, 6, 7]. There is, for instance, mounting evidence for the key role played by tissue material properties and their regulation during embryonic development [8]. Tissues must be able to adjust their mechanical properties in response to internal and external stimuli. In particular, epithelial tissues, which line all cavities in the body and demarcate organs, must sustain substantial mechanical stresses while also supporting numerous biological processes such as selective diffusion and absorption/secretion of molecules [9]. In homeostasis, epithelia must maintain their shape and resist deformation while remaining flexible. The tissue must also be able to regenerate and repair itself, often with fast turnover, e.g., in gut epithelia [10]. Furthermore, in morphogenesis, the epithelial tissue must take up a specific shape and function [11], but this shape is lost during metastasis when cancer cells invade surrounding healthy tissues [12]. All of these processes require that cells be able to move, often over distances much larger than the cell size. During cell migration, however, the epithelial tissue must maintain its integrity. It is, therefore, not surprising that epithelia exhibit rich viscoelastic behavior [13]. Unlike passive viscoelastic materials, an epithelial tissue can actively tune its rheological response, making the study of its rheology not only important for understanding biological functions but also an interesting problem from the perspective of the physics of active matter systems [4].

Collective cell migration has been extensively studied in biology [14] and biophysics [15]. In vitro studies of confluent cell monolayers [16, 17, 18, 19, 20] focused on the physical aspects of force generation and transmission and showed that cell migration is an inherently collective phenomenon. Some aspects of collective cell migration are remarkably similar to the slow dynamics of structural glasses [21, 22, 23, 24, 25, 26, 27]. This suggests that many of the observed

behaviors share common underlying mechanisms and can be understood, at least at mesoscales (i.e., distances beyond several cell diameters), using physics of dense active systems [28]. A particularly intriguing observation is that tuning cell density [29, 21, 30], strength of cell-cell and cell-substrate interactions [31], or cell shape parameters [24, 32] can stop collective migration. In other words, the epithelium undergoes a fluid to solid transition. Signatures of such behavior have been reported in several in vitro [22, 33] and developmental systems [34, 35, 36]. This suggests that important aspects of morphogenetic development may rely on epithelial tissue's ability to undergo phase transitions [8].

How an epithelial tissue responds to external and internal mechanical stresses depends on its rheological (i.e., material) properties. While there have been numerous studies focusing on the rheology of a single cell [37, 38, 39], much less is known about tissue rheology, particularly during development. In order to develop a comprehensive understanding of epithelial tissue mechanics, such insight is key. Though single cell measurements are valuable, the mechanics of an epithelial tissue can be drastically different from that of its constituent cells. The stiffness of cell monolayers, for example, is orders of magnitude higher than the stiffness of constituent cells, while the time dependent mechanical behaviors of monolayers in response to deformation vary depending on the magnitude of loading [40]. Embryonic cell aggregates have been shown to behave elastically (i.e., solid-like) at short timescales, but they flow like fluids at long timescales, which facilitates both the robustness needed to maintain integrity and the flexibility to morph during development [13]. Experiments have characterized the mechanical behaviors of epithelial tissues at various loading conditions, which led to a phenomenological description that models the relaxation properties of epithelial monolayers based on fractional calculus [41]. Notably, a recent particle-based model that includes cell division and apoptosis provided a plausible microscopic model for nonlinear rheological response [42]. Particle-based models are, however, unable to

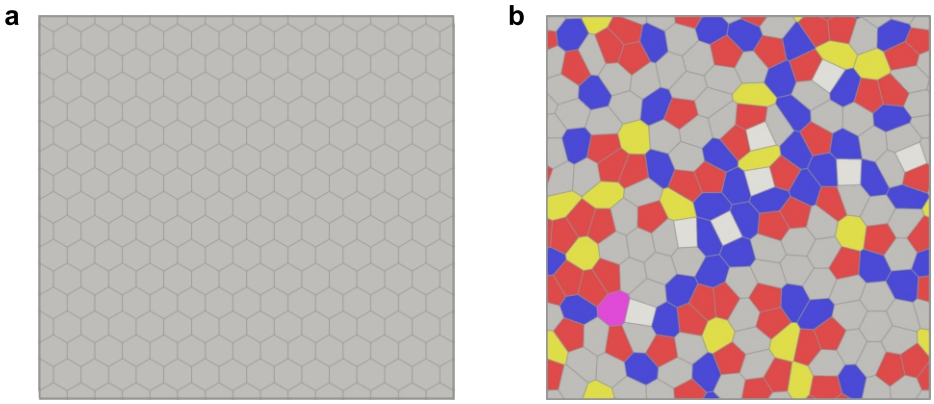


Figure 1.1: In the vertex model, epithelial tissue is represented as a polygon tiling of the plane subject to periodic boundary conditions. We studied the rheology of the vertex model for both (a) regular hexagonal and (b) disordered tilings. Colors represent the number of neighbors of each cell; 4-white, 5-red, 6-gray, 7-blue, 8-yellow.

capture geometric aspects such as cell shape. It is, therefore, necessary to investigate rheological response in geometric models.

### 1.1.1 Mechanical properties of vertex model tissue

The vertex model [43, 44, 45] and more recent, closely related Voronoi models [24, 46, 47] have played an important role in modeling mechanics of epithelial tissues since they account for the shapes of individual cells and provide a link to cellular processes, such as cell-cell adhesion, cell motility, and mitosis [45]. These geometric models are also able to demonstrate rich and unusual nonlinear mechanical behavior [48, 49]. Using the vertex model, Bi, et al. predicted that epithelial tissues can undergo rigidity transition at constant density by tuning cell properties. [23] These unexpected results have been observed in-vitro in human bronchial cell monolayers, [22] and have sparked interest in understanding how biological systems can take advantage of the presence of phase transitions and the accompanying tissue rheology. [8, 50] Understanding mechanical and rheological properties of the vertex model and the closely related self-propelled Voronoi model [24, 46, 32] has, therefore, attracted significant attention. [48, 51, 52, 53]

While the mechanical properties of the vertex and Voronoi models have been extensively studied, most works to date focused on the long-time behavior. These include studies of the quasistatic shear modulus [23], effective diffusion constant of cells related to the tissue viscosity [24], correlations between a structural property called "softness" and the likelihood of topological rearrangements of cells [54], and steady state flow profiles around a sphere dragged through the tissue [55]. The rheological properties of the vertex model that cover a broad range of timescales, however, have not yet been systematically explored. In Chapter 2, I present a detail study of the linear rheological properties of the vertex model for both regular hexagonal and disordered cell configurations (see Fig 1.1) over a wide range of driving frequencies. The contents of Chapter 2 have been published in the journal *PLOS Computational Biology* [52].

### 1.1.2 Understanding rheological properties of the vertex model using normal mode analysis

In Chapter 3, we develop a semi-analytic formalism to study the shear rheology of the vertex model for epithelial tissues. The method developed is general and can be used for investigating the linear rheological response of a broad class of soft and biological matter over the full range of driving frequencies. Our approach is based on the well-known decomposition in terms of normal modes. [56] We show that each normal mode is equipped with a characteristic relaxation timescale. Displacements along each normal mode produce stresses due to elastic deformation and internal dissipation, which are in force balance with loads due to external dissipation. Interestingly, the rheological behavior of a given normal mode can be described as a combination of a standard linear solid element due to elastic stresses and a Jeffreys model element due to the internal dissipative stresses. The rheological behavior of the system is then fully determined by connecting in parallel all the viscoelastic elements corresponding

to individual normal modes. This behavior is generic and does not depend on the details of the microscopic model for dynamics. The method discussed in Chapter 3 shares similarities with several recent studies, [57, 58, 59] but it complements them by allowing treatment of various dissipative mechanisms.

We applied the normal mode formalism to study the linear response of the vertex model, [60, 44, 61] which is widely used to describe the mechanical properties of epithelial tissues. Most studies to date [62, 63, 64, 53] focused on the quasistatic regime including with large deformations, where plastic relaxation facilitated by cell rearrangements via T1 events leads to a strong non-linear response. Here, we take the opposite limit and explore the dynamic linear response of the vertex model over a wide range of driving frequencies and three different microscopic models of dissipation. In Chapter 2, we numerically investigated the linear viscoelastic response of the vertex model with external dissipation. We found that even in the linear regime, the vertex model shows complex viscoelastic response, especially in the fluid phase, with multiple competing time scales. In Chapter 3, we demonstrated that the complex viscoelastic response of the vertex model can be accurately captured by normal modes. In addition, we show that internal and external dissipative mechanisms can result in a markedly different rheological response, emphasizing the importance of dissipation for the rheological behavior of model epithelial tissues. The contents of Chapter 3 have been published in the journal *Physical Review Research* [65].

## 1.2 Mechanical response of wrinkled structures

In the last few decades, surface wrinkling of thin films bound to compliant substrates has been well studied through experimental and theoretical analysis [66, 67, 68, 69, 70, 71, 72, 73, 74]. Although in the past, Wrinkling phenomena, as one kind of mechanical instability, have been considered a mode of mechanical failure. In recent

years, many studies have exploited wrinkling instability to apply in various fields ranging from flexible electronics to biomedical engineering [75, 76, 77]. The study of wrinkling instability has also helped to understand the pattern formation of confined systems in biology [78, 79, 80, 81].

Many studies have developed applications that exploit structures with tunable surface morphology through wrinkling instability. For example, structures with tunable drag [82], wetting [83] and adhesion properties [84]. Besides, wrinkling instability is used to make templates for DNA wire formation [85]. In all these applications, wrinkled structures interact with the environment to provide specific functions. Although these experimental studies demonstrate the proofs of concepts, there is much less quantitative understanding of how wrinkled structures deform in response to their interactions with the environment. To understand the mechanical response behavior of wrinkled structures, we systematically studied how the structures respond to infinitesimal surface forces in Chapter 4. Using the perturbation method, we developed a linear response theory of wrinkled structures, which is verified with numerical simulations. Although large external forces might induce some interesting response behavior, for example, wrinkle-to-fold transition [86, 74] and self-similar wrinkling patterns [87], the study of large response behavior in the nonlinear regime is out of the scope of this work.

There are a few mechanisms that can lead to wrinkling phenomena [88]. One can compress the film and substrate together or effectively compress the film only by pre-stretching the substrate or pre-compressing the film. Another way is to introduce differential growth or expansion in the structure [67]. These mechanisms generate equivalent wrinkling phenomena when the strain is small, and the film is much stiffer than the substrate. For the simplicity of our theoretical model, we consider that the film is compressed by a uni-axial strain $\eta_x > 0$, which is illustrated in Fig. 1.2(a). Once the strain $\eta_x$ is above a critical threshold $\eta_{x,cr}$, wrinkling instability occurs. We

then studied the linear response behavior of wrinkled structures due to infinitesimal forces. We applied infinitesimal point forces at the film's top surface either in the vertical or horizontal direction, as shown in Fig. 1.2(b,c). The contents of Chapter 4 are under preparation to be submitted for publication.

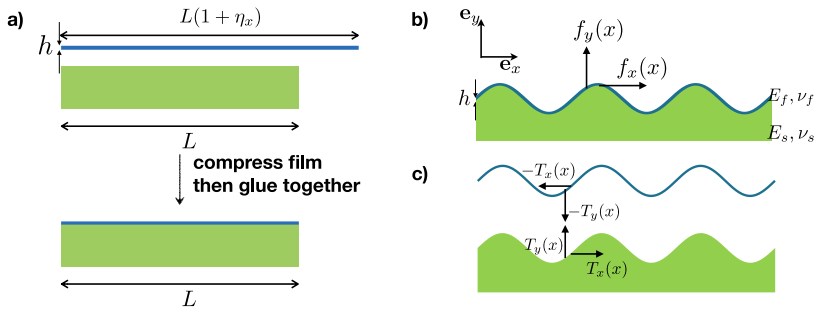


Figure 1.2: A schematic of the wrinkling instability and linear response of a wrinkled structure to point forces. (a) A thin stiff film is compressed by the strain $\eta_x$ and then glued together with the soft substrate. Wrinkling instability occurs when the compressive strain $\eta_x$ is above a critical threshold $\eta_{x,cr}$. (b,c) A schematic of the geometry and notations for the problem. (c) Interactions between film and substrate are described by the traction $T_x(x)$ and $T_y(x)$ at the interface.

## 1.3 Thesis outline

The remaining part of the thesis is organized as follows. In Chapter 2, we study the linear viscoelastic properties of the vertex model, which is commonly used to model the mesoscopic mechanical properties of epithelial tissues. In Chapter 3, we develop a normal mode formalism to describe the shear rheology of the vertex model over the full dynamical range in the overdamped linear response regime. In Chapter 4, we describe the mechanical response of wrinkled structures at the onset of instability and moderately above the instability threshold. In Chapter 5, I present a summary of all these works and point out some future directions.

# Chapter 2

# Linear viscoelastic properties of the vertex model for epithelial tissues

In this chapter, we present the linear viscoelstic properties of a model epithelial tissue adhered to a substrate. We study the response of the vertex model with the regular hexagonal and disordered cell configurations (see Fig 1.1) to applied oscillatory shear and bulk deformations of small amplitude, i.e., in the linear response regime. We measure the response stresses and use them to compute the storage and loss moduli in both the solid and fluid phases. We show that the dynamical response of the vertex model can be fitted to standard spring-dashpot viscoelastic models over seven decades in the driving frequency and that the solid-fluid transition can be tuned by applying pre-deformation to the system. Thus we argue that the vertex model makes a suitable basis for studies of dynamics of epithelial tissues beyond the quasistatic limit.

The structure of this chapter is summarised as follows. In section 2.1, we introduce the vertex model and how we set up the simulations and probe the rheology. In

section 2.2, we present the shear and bulk rheology of the vertex model for both regular hexagonal and disordered cell configurations over a wide range of driving frequencies. The linear viscoelastic responses of the vertex model are mapped to standard spring-dashpot models. Besides, we show in section 2.2.3 that the solid-fluid transition can be tuned by applying pre-deformation to the system.

## 2.1 Model and Methods

### 2.1.1 Vertex model

In the vertex model, the state of an epithelial tissue is approximated as a polygonal tiling of the plane (Fig 1.1). The degrees of freedom are vertices, i.e., meeting points of three or more cell-cell junctions. In the simplest formulation, junctions are assumed to be straight lines. The energy of the vertex model is a quadratic function of cell areas and perimeters [44], i.e.,

$$E = \sum_C \left[ \frac{K_C}{2} \left( A_C - A_{C0} \right)^2 + \frac{\Gamma_C}{2} \left( P_C - P_{C0} \right)^2 \right], \tag{2.1}$$

where $K_C$ and $\Gamma_C$ are the area and perimeter elastic moduli, and $A_C$ and $A_{C0}$ are the actual and preferred areas of cell $C$, respectively. Similarly, $P_C$ and $P_{C0}$ are the actual and preferred perimeters of the same cell. In this work, we assumed $K_C$, $\Gamma_C$, $A_{C0}$, and $P_{C0}$ to be identical for all cells (i.e., $K_C \equiv K, \Gamma_C \equiv \Gamma, A_{C0} \equiv A_0, P_{C0} \equiv P_0$). Further, we fixed the values of $K$ and $A_0$, and measured the energy in units of $KA_0^2$, stresses in units of $KA_0$, and lengths in units of $A_0^{1/2}$. Since the ratio between the perimeter and area elastic moduli does not qualitatively change the behavior of the vertex model [44, 23], we fixed that ratio to $\Gamma/(KA_0) \approx 0.289$ for all simulations. The only variable parameter in simulations was the preferred cell perimeter $P_0$, which sets the dimensionless cell-shape parameter, defined as the ratio $p_0 = P_0/\sqrt{A_0}$.

The cell-shape parameter, $p_0$, plays a central role in determining whether the system behaves as a fluid or solid [23]. Bi, *et al.* [23] argued that the rigidity transition occurs at $p_0 = p_c \approx 3.812$ for a disordered polygonal tiling, while Merkel, *et al.* [51] reported $p_0 = p_c \approx 3.92$. For a regular hexagonal tiling, the transition point is at $p_c = \sqrt{8\sqrt{3}} \approx 3.722$ [89]. In the fluid phase, the energy barrier for neighbor exchanges vanishes and cells can flow past each other [90]. As $p_0$ is reduced below $p_c$, the energy barrier becomes finite, neighbor exchanges cease and the system becomes solid. While the transition point for regular hexagonal tilings can be understood in terms of the mechanical stability and the excess perimeter [48, 91], the mechanism that leads to a larger value for random tilings is more subtle and only partly understood [92]. For example, recent studies [51, 93] have shown that the rigidity transition of random tilings depends on the procedure used to generate the tilings. The presence of vertices with coordination greater or equal to four, as well as the presence of cells with five or less neighbors, increases the critical value of the cell-shape parameter $p_0$ [93].

### 2.1.2 Simulation setup

We first studied the rheology of regular hexagonal tilings (Fig 1.1a) subject to periodic boundary conditions. The shape of the simulation box was chosen to be as close to a square as allowed by the geometry of a hexagon, and the area of the box was such that it accommodated $N$ cells of area $A_C$ that matched the preferred areas $A_0$. Most simulations started with hexagonal tiling with $N_x = 15$ cells in the horizontal direction (i.e., $N = 240$ cells in total, Fig 1.1a). Simulations of larger system sizes ($N_x = 37$, 51, i.e., $N = 1406$, 2652 total cells, respectively) were performed for a subset of values of $p_0$ to explore the finite size effects. No quantitative differences between the system with $N = 240$ cells and larger systems were observed.

For the solid phase with $p_0 \lesssim 3.722$, the ground state of the energy in Eq. (2.1) is the honeycomb lattice [89], and it was directly used to investigate rheological prop-

erties. Note that there was some residual hydrostatic stress due to the mismatch of actual cell perimeters $P_C$ from their preferred values $P_0$, which could be eliminated by appropriate rescaling of the simulation box. This hydrostatic stress, however, does not qualitatively affect the rheological behavior of the system (see Appendix A, Sec. A.4 for further discussion). For the fluid phase with $p_0 \gtrsim 3.722$, the hexagonal tiling corresponds to a saddle point of the energy in Eq. (2.1) [89]. A small random perturbation was applied to each vertex, i.e., each vertex was displaced from its original position in the hexagonal tiling by a vector $\delta\mathbf{r}_i = \delta x_i \mathbf{e}_x + \delta y_i \mathbf{e}_y$, where $\delta x_i$ and $\delta y_i$ were Gaussian random variables with zero mean and standard deviation $1.5 \times 10^{-4}\sqrt{A_0}$; the system was then relaxed using the FIRE algorithm [94] to reach a local energy minimum with the relative accuracy of $10^{-12}$. Note that the energy landscape in the fluid phase has many local minima and a large number of soft modes (see Appendix A, Sec. A.8). We repeated simulations to investigate rheological properties for multiple configurations corresponding to different local energy minima.

The study of the rheological properties of the vertex model for a regular hexagonal tiling is appealing since one can make comparisons to analytical treatments. The regular hexagonal tiling is, however, a rather crude approximation of real epithelial tissues, which are typically irregular [95]. Therefore, we also investigated the rheology of the vertex model of disordered tilings (Fig 1.1b). The disordered tilings were created as follows (see see Fig. A.1 for a schematic illustration). We used the random sequential addition algorithm [96] to place $N = 200$ seed points inside a square box of size $L = 15$ without overlaps. We then created periodic images of the seed points and used SciPy to build the periodic Voronoi tessellation [97]. The preferred area of each cell was set to $A_0 = L^2/N$. The energy of the system given in Eq. (2.1) was then relaxed using the FIRE algorithm to reach a local minimum. During the energy minimization, T1 transitions (exchanges of cell neighbors) were allowed but were not common. We generated an ensemble of 10 different random initial configurations

using different values of the random number generator seed and repeated rheology simulations for each of those configurations to probe the rheology for a range of values of $p_0$.

### 2.1.3 Dynamics and probing the rheology

In order to probe the dynamic response of the vertex model, we need to specify the microscopic equations of motion for vertices. Assuming the low Reynolds number limit, which is applicable to most cellular systems due to their slow speed, inertial effects can be neglected [98]. The equations of motion are then a force balance between friction with the substrate and elastic forces $\mathbf{F}_i$ due to deformations of cell shapes, i.e.,

$$\gamma \dot{\mathbf{r}}_i = \mathbf{F}_i. \tag{2.2}$$

Here, we assume that friction between the tissue and the substrate arises from binding and unbinding of adhesion molecules. In particular, on time scales much longer than the characteristic unbinding time, the tissue–substrate adhesive bonds undergo stick-and-slip processes leading to a form of viscous friction [99, 100, 101]. In the above Eq. (2.2), $\mathbf{r}_i$ is the position vector of vertex $i$ in a laboratory frame of reference, $\mathbf{F}_i = -\nabla_{\mathbf{r}_i} E$ is the mechanical force on vertex $i$ due to deformation of cells surrounding it, $\gamma$ is the friction coefficient, and dot denotes the time derivative. Therefore, each vertex experiences dissipative drag proportional to its instantaneous velocity. We fixed the value of $\gamma$ in simulations, which sets the unit of time as $\gamma/(KA_0)$. Furthermore, we neglected thermal fluctuations and hence omit the stochastic term in Eq. (2.2). This is a reasonable assumption since typical energy scales in tissues significantly exceed the thermal energy, $k_B T$, at room temperature $T$, where $k_B$ is the Boltzmann constant. It is, however, worth noting that there are other sources of stochasticity in epithelia (e.g., fluctuations of the number of force-generating molecular motors)

which are important for tissue scale behaviors [102]. Here, we did not consider such effects but note that they could be directly included in the model as additional forces in Eq. (2.2).

We applied an oscillatory affine deformation to investigate the rheological behavior of the vertex model. The affine deformation can be described by a deformation gradient tensor defined as $\hat{\boldsymbol{F}} = \partial \mathbf{x}/\partial \mathbf{X}_0$, where the mapping $\mathbf{x} = \mathbf{x}(\mathbf{X}_0, t)$ maps the reference configuration $\mathbf{X}_0$ to a spatial configuration $\mathbf{x}$ at time $t$. Note that the affine deformation was applied to all vertices inside the bounding box as well as to the periodic images of vertices, which ensured deformation of cells across periodic boundaries. Specifically, for a vertex $i$ with a position vector $\mathbf{r}_i(t)$ in a deformed configuration, we also consider its periodic images at positions $\mathbf{r}_i(t) + m_1\mathbf{a}_1(t) + m_2\mathbf{a}_2(t)$, where $\mathbf{a}_{1,2}(t)$ are the unit cell vectors of the periodic box and $m_{1,2}$ are integers. For cells that cross the periodic boundary, junction lengths are computed using the minimum image convention. Note that the unit cell vectors of the periodic box transform as $\mathbf{a}_{1,2}(t) = \hat{\boldsymbol{F}}(t)\mathbf{a}_{1,2}(0)$ due to the affine deformation.

The deformation gradient of simple shear is $\hat{\boldsymbol{F}}(t) = \left(\begin{smallmatrix} 1 & \epsilon(t) \\ 0 & 1 \end{smallmatrix}\right)$ and of biaxial deformation is $\hat{\boldsymbol{F}}(t) = \left(\begin{smallmatrix} 1+\epsilon(t) & 0 \\ 0 & 1+\epsilon(t) \end{smallmatrix}\right)$, where $\epsilon(t) = \epsilon_0 \sin(\omega_0 t)$ and $\omega_0$ is the frequency of the oscillatory deformation. In all simulations, we used a small magnitude of deformation, i.e., $\epsilon_0 = 10^{-7}$, so that we probed the linear response and the measured moduli were independent of the magnitude of the deformation. In every time step after the affine deformation was applied, the system evolved according to the overdamped dynamics in Eq. (2.2). During the oscillatory deformations, T1 transitions were allowed but were not common. Equations of motion were integrated using the first-order Euler method [103] with the time step $\Delta t \approx 0.00866\gamma/(KA_0)$ when the frequency of oscillatory deformation $\omega_0\gamma/(KA_0) < 29.02$, but with a smaller time step $\Delta t \approx 0.000866\gamma/(KA_0)$ when $\omega_0\gamma/(KA_0) > 29.02$ so that there were enough sampling points (at least 25) over one period of oscillatory deformation.

The response stress tensor, $\hat{\boldsymbol{\sigma}}_C(t)$, for each cell $C$ was computed using the formalism introduced in Refs. [104, 105, 106] as

$$\hat{\boldsymbol{\sigma}}_C = -\Pi_C \hat{\boldsymbol{I}} + \frac{1}{2A_C} \sum_{e \in C} \mathbf{T}_e \otimes \mathbf{l}_e, \tag{2.3}$$

where the summation is over all junctions $e$ belonging to cell $C$. Here, $\Pi_C = -\frac{\partial E}{\partial A_C} = -K(A_C - A_0)$ is the hydrostatic pressure inside a cell, $\hat{\boldsymbol{I}}$ is the unit tensor, and $\mathbf{T}_e = \frac{\partial E}{\partial \mathbf{l}_e} = \Gamma(P_C - P_0)\mathbf{l}_e/|\mathbf{l}_e|$ is the tension along the junction $e$ with $\mathbf{l}_e$ being a vector joining the two vertices on it [104, 105, 106]. The average stress tensor $\hat{\boldsymbol{\sigma}}(t) = \sum_C w_C \hat{\boldsymbol{\sigma}}_C(t)$, with $w_C = A_C / \sum_C A_C$, was used as a measure for the response of the system. Measurements of the response stresses for each cell [see Eq. (2.3)] and the entire system were taken 25 times within each cycle of oscillatory deformation.

To ensure that we were probing the steady state, we performed the following analysis. For example, in the case of shear deformation, the shear stress signal $\tau(t) = \hat{\sigma}_{xy}(t)$ was divided into blocks of length $T = 3T_0$, each containing 3 cycles of the time period $T_0 = 2\pi/\omega_0$ of the driving shear deformation. Within each block $n$, we performed the Fourier transform of $\tau(t)$ and obtained $\tilde{\tau}_n(\omega)$ as

$$\tilde{\tau}_n(\omega) = \frac{1}{T} \int_{(n-1)T}^{nT} \tau(t) e^{i\omega t} dt, \tag{2.4}$$

where $n$ is a positive integer. Similar Fourier transform analysis was performed for the strain, $\epsilon(t)$, of which the Fourier transform is denoted as $\tilde{\epsilon}(\omega)$. The length of the simulation was chosen such that it contained a sufficient number of blocks in order for the $\tilde{\tau}_n(\omega_0)$ to reach a steady state value $\tilde{\tau}(\omega_0)$. The obtained steady state value of $\tilde{\tau}(\omega_0)$ was used to calculate the dynamic shear modulus $G^*(\omega_0) = \tilde{\tau}(\omega_0)/\tilde{\epsilon}(\omega_0)$ at a given frequency $\omega_0$ of applied shear strain. We ensured that simulations ran long enough to reach a steady state. An analogous procedure was applied to the hydrostatic stress, $\sigma(t) = \frac{1}{2}[\hat{\sigma}_{xx}(t) + \hat{\sigma}_{yy}(t)]$, in the case of the bulk deformation.

Please refer to Appendix A, Sec. A.3 for a representative example of the steady state analysis.

## 2.2 Results

### 2.2.1 Response to shear deformations

The hexagonal ground state in the solid phase and states corresponding to local energy minima in the fluid phase were used to investigate the rheological behavior by applying an oscillatory affine shear deformation to the substrate (Fig 2.1a and 2.1b). Due to the binding and unbinding of adhesive molecules, deformation of the tissue follows the deformation of the substrate on short timescales, and then tissue can relax on longer timescales. Thus, at each time step, we first applied the affine shear deformation to the simulation box and all vertices, which was followed by internal relaxation of the vertices according to Eq. (2.2). The affine simple shear deformation can be described by a deformation gradient tensor, $\hat{\boldsymbol{F}} = \left(\begin{smallmatrix} 1 & \epsilon(t) \\ 0 & 1 \end{smallmatrix}\right)$, where $\epsilon\left(t\right) = \epsilon_0 \sin\left(\omega_0 t\right)$. Sufficiently small amplitude $\epsilon_0 = 10^{-7} \ll 1$ was used to probe the linear response properties.

We measured the response stresses as described in the Model and Methods section above. The dynamic shear modulus $G^*\left(\omega_0\right) = \tilde{\tau}(\omega_0)/\tilde{\epsilon}(\omega_0)$ was then calculated at a given frequency $\omega_0$ of applied shear strain, where $\tilde{\tau}(\omega)$ and $\tilde{\epsilon}(\omega)$ are the Fourier transforms of the response shear stress $\tau(t) = \hat{\sigma}_{xy}\left(t\right)$ and the applied strain $\epsilon(t)$, respectively (see Model and Methods). We ensured that simulations ran long enough to reach a steady state (see Model and Methods and Appendix A, Sec. A.3). The real part of the dynamic shear modulus, $G' = \mathrm{Re}\left(G^*\right)$, is the storage shear modulus and the imaginary part, $G'' = \mathrm{Im}\left(G^*\right)$, is the loss shear modulus. The storage shear modulus corresponds to the in-phase response and measures the elastic (i.e., reversible) response of the system, while the loss shear modulus corresponds to the out-of-phase response and measures the system's irreversible dissipation [107] (see also

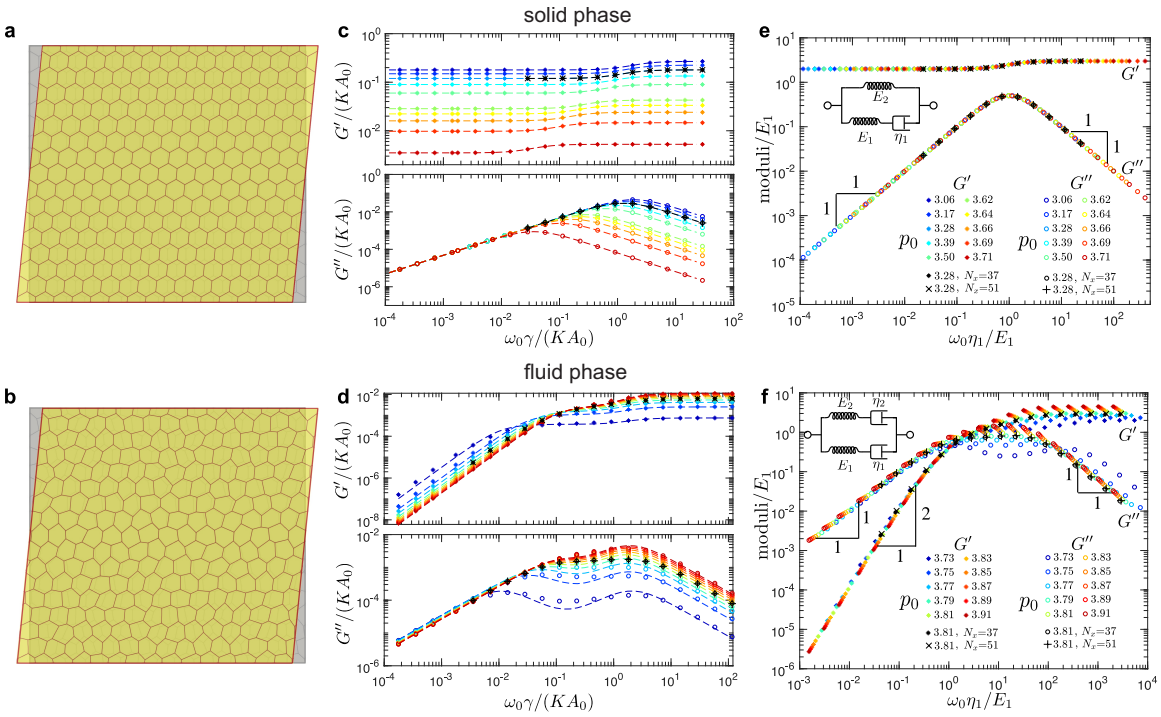


Figure 2.1: Storage and loss shear moduli in the solid (top row) and fluid phase (bottom row) for hexagonal tilings. (a-b) An overlay of the representative reference (grey) and sheared (yellow) configurations in (a) the solid and (b) the fluid phase. The magnitude of the shear is highly exaggerated for demonstration purposes. (c-d) Representative storage ($G'$) and loss ($G''$) shear moduli as functions of the shearing frequency, $\omega_0$, for different values of the cell-shape parameter, $p_0$. Dashed curves are the fits based on (c) the Standard Linear Solid (SLS) model in the solid phase [see Eq. (2.5)] and (d) the Burgers model in the fluid phase [see Eq. (2.8)]. (e-f) The collapse of the moduli curves for different values of $p_0$ for (e) the solid phase and (f) the fluid phase. The insets show the representation of (e) the SLS model and (f) the Burgers model in terms of the springs and dashpots. The majority of the data corresponds to the system of nearly square shape with $N_x = 15$ cells in the horizontal direction, and we also show examples of larger systems with $N_x = 37$ and $N_x = 51$ cells in the horizontal direction.

Appendix A, Sec. A.2). For systems under an oscillatory simple shear, storage and loss shear moduli were obtained for different values of $p_0$ and different system sizes in the solid and the fluid phases for a broad range of driving frequencies $\omega_0$ spanning over seven orders of magnitude, as shown in Fig 2.1c and 2.1d. Most simulations were performed for systems with nearly square shapes with $N_x = 15$ cells in the horizontal

direction. We repeated several simulations for systems with $N_x = 37$ and $N_x = 51$, which showed that the finite size effects are negligible (Fig 2.1c-f).

In the solid phase there are two different regimes (see Fig 2.1c). At low frequencies, $\omega_0$, the storage shear modulus $G'$ has a constant value, while the loss shear modulus scales as $G'' \propto \omega_0$. At high frequencies, the storage shear modulus $G'$ has a higher constant value, while the loss shear modulus scales as $G'' \propto \omega_0^{-1}$. Such rheological behavior is characteristic of the Standard Linear Solid (SLS) model [107]. Storage and loss shear moduli for the SLS model are [107], respectively,

$$G'_{\mathrm{SLS}}(\omega_0) = \frac{E_2 + \frac{\eta_1^2}{E_1^2}\omega_0^2 (E_1 + E_2)}{1 + \frac{\eta_1^2}{E_1^2}\omega_0^2}, \tag{2.5a}$$

$$G''_{\mathrm{SLS}}(\omega_0) = \frac{\omega_0 \eta_1}{1 + \frac{\eta_1^2}{E_1^2}\omega_0^2}, \tag{2.5b}$$

where we used the representation of the SLS model (Fig 2.1e, inset) that consists of a spring with elastic constant $E_2$ connected in parallel with a Maxwell element, which comprises a spring with elastic constant $E_1$ and a dashpot with viscosity $\eta_1$ connected in series. The above expressions in Eqs. (2.5) were used to fit the storage and loss shear moduli obtained from simulations. The fitted curves, represented with dashed lines in Fig 2.1c, show an excellent match with the simulation data, indicating that the SLS model is indeed appropriate to describe the shear rheology in the solid phase. This was also confirmed in Fig 2.1e, where we collapsed the storage and loss shear moduli for different values of the shape parameter, $p_0$, by rescaling the moduli and frequencies with the fitted values of spring and dashpot constants. Note that the SLS response in the solid phase is consistent with recent experiments on suspended MDCK monolayers [108].

As the value of the $p_0$ increases, we observe that the storage shear modulus reduces at all frequencies and that the loss shear modulus reduces at high frequencies. Further-

more the crossover between the two regimes shifts towards lower frequencies (Fig 2.1c). This is because the elastic constants $E_1$ and $E_2$ decrease linearly with increasing $p_0$ and they become zero exactly at the solid-fluid transition with $p_0 = p_c \approx 3.722$ (Fig 2.2a). The dashpot constant $\eta_1$ is nearly independent of $p_0$ (Fig 2.2b) and scales with the friction parameter $\gamma$, which is the only source of dissipation in the vertex model. The crossover between the two regimes for both the storage and loss shear moduli corresponds to a characteristic timescale, $\eta_1/E_1$, which diverges as $\sim \gamma(KA_0)^{-1}(p_c - p_0)^{-1}$ as $p_0$ approaches the solid-fluid transition (Fig 2.2c) due to the vanishing elastic constant (Fig 2.2a). Note that the values of the elastic constants $E_1$ and $E_2$ can be estimated analytically. In the quasistatic limit ($\omega_0 \to 0$), the external driving is sufficiently slow that the system can relax internally. In this limit, Murisic, *et al.* [109] showed that the storage shear modulus is

$$G'(\omega_0 \to 0) = E_2 = \frac{1}{2} KA_0 \Big(1 - \big[\alpha(p_0, \Gamma/KA_0)\big]^2\Big), \tag{2.6}$$

where $\alpha(p_0, \Gamma/KA_0)$ is a scaling factor chosen such that the hydrostatic stress vanishes once the system box size is rescaled from $L$ to $\alpha L$ (see Appendix A, Sec. A.4). In the high frequency limit ($\omega_0 \to \infty$), on the other hand, the system follows the externally imposed affine deformation and has no time for internal relaxation. Thus, by considering the energy cost for a hexagonal tiling under affine deformation, we obtained the storage shear modulus (see Appendix A, Sec. A.7)

$$G'(\omega_0 \to \infty) = E_1 + E_2 = 3\sqrt{3}\Gamma \left(1 - \frac{p_0}{p_c}\right). \tag{2.7}$$

The above Eqs. (2.6) and (2.7) were used to extract the values of elastic constants $E_1$ and $E_2$, which showed excellent agreement with the fitted values from simulations (Fig 2.2a).

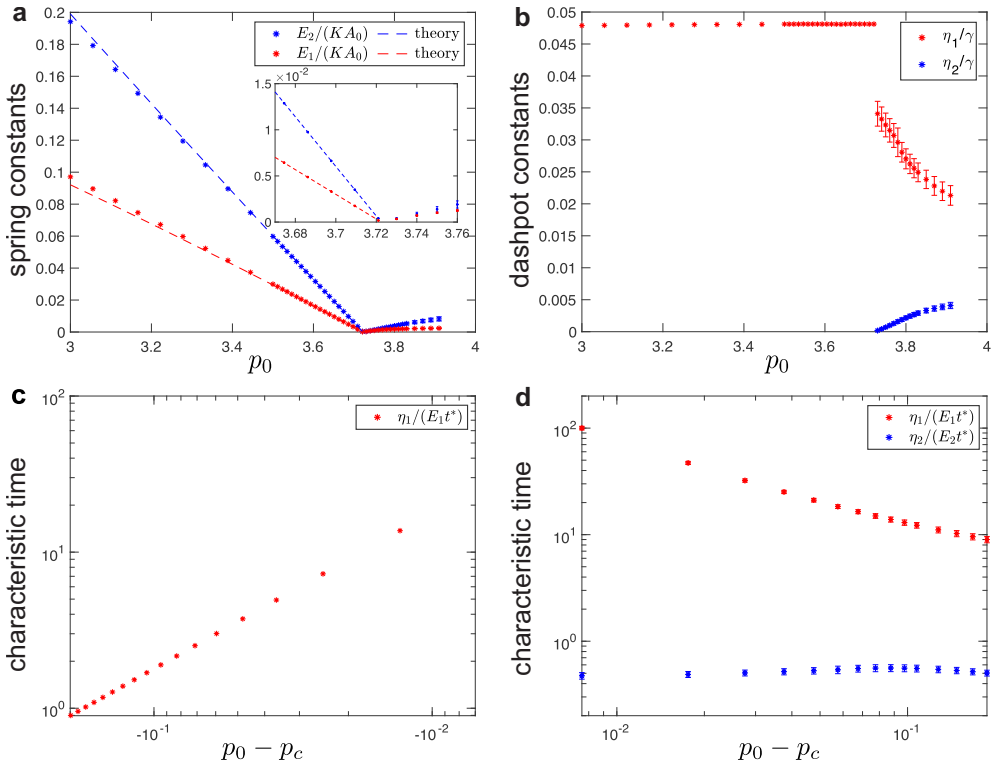


Figure 2.2: (a-b) Fitted values of spring-dashpot models for hexagonal tilings under simple shear. (a) Elastic constants as a function of target cell-shape parameter, $p_0$. In the solid phase (i.e., for $p_0 < p_c \approx 3.722$), fitted values of the spring constants show excellent match with the analytical predictions obtained from Eqs. (2.6) and (2.7) (dashed lines). Inset shows the spring constants near the critical point. (b) Dashpot viscosity constants as a function of the target cell-shape parameter, $p_0$. (c-d) Characteristic timescales in (c) the solid and (d) fluid phase for hexagonal tilings obtained from the fitted values of the elastic constant and the dashpot viscosity. The normalization factor $t^* = \gamma/(KA_0)$ sets the unit of time. For the fluid phase (i.e., for $p_0 > p_c \approx 3.722$), errorbars correspond to the standard deviation for simulations that were repeated for configurations that correspond to different local energy minima.

In the fluid phase, the storage and loss shear moduli show a markedly different behavior (Fig 2.1d). There are three different regimes with two crossover frequencies, which correspond to two characteristic timescales. At low frequencies, $\omega_0$, the storage shear modulus $G' \propto \omega_0^2$ and the loss shear modulus $G''(\omega_0) \propto \omega_0$. The storage modulus approaches 0 for $\omega_0 \to 0$, which indicates that the system is indeed a fluid. At high frequencies the storage shear modulus has a constant value, while the loss shear modulus scales as $G''(\omega_0) \propto \omega_0^{-1}$. To capture this behavior we used the Burgers model, which consists of two Maxwell models connected in parallel (Fig 2.1f, inset), to fit the shear moduli measured in the simulations. The storage and loss shear moduli for a Burgers model are [107], respectively,

$$G'_{\text{Burg}}(\omega_0) = \frac{p_1 q_1 \omega_0^2 - q_2 \omega_0^2 (1 - p_2 \omega_0^2)}{p_1^2 \omega_0^2 + (1 - p_2 \omega_0^2)^2}, \tag{2.8a}$$

$$G''_{\text{Burg}}(\omega_0) = \frac{p_1 q_2 \omega_0^3 + q_1 \omega_0 (1 - p_2 \omega_0^2)}{p_1^2 \omega_0^2 + (1 - p_2 \omega_0^2)^2}, \tag{2.8b}$$

where $p_1 = \eta_1/E_1 + \eta_2/E_2$, $p_2 = \eta_1\eta_2/(E_1E_2)$, $q_1 = \eta_1 + \eta_2$, $q_2 = \eta_1\eta_2(E_1+E_2)/(E_1E_2)$. The dashed curves in Fig 2.1d show fits of the storage and loss shear moduli for a range of values of $p_0$, which show good agreement with simulations. Unlike for the solid phase, it is not possible to collapse the data for storage and loss shear moduli onto single universal curves because the fluid phase is characterized by two independent timescales $\eta_1/E_1$ and $\eta_2/E_2$. Thus we show two different collapses for the storage and loss shear moduli in the low frequency range (Fig 2.1f) and in the high frequency range (Fig. A.5 in the Appendix A, Sec. A.5).

As the value of the $p_0$ decreases, we observe that both the storage and loss shear moduli reduce at intermediate and high frequencies, but they increase at low frequencies (Fig 2.1d). We also observe that the first crossover shifts towards lower frequencies, while the second crossover remains at approximately the same frequency. This is because the elastic constants $E_1$ and $E_2$ decrease linearly toward zero as $p_0$ approaches

the solid-fluid transition at $p_c \approx 3.722$ (Fig 2.2a). The dashpot constant $\eta_2$ also decreases linearly toward zero, while the dashpot constant $\eta_1$ increases but remains finite as $p_0$ approaches the solid-fluid transition (Fig 2.2b). As a consequence, one of the characteristic timescales $\eta_1/E_1 \sim \gamma(KA_0)^{-1}(p_0 - p_c)^{-1}$ diverges, while the second timescale $\eta_2/E_2 \sim \gamma(KA_0)^{-1}$ remains finite as $p_0$ approaches the solid-fluid transition (Fig 2.2d). The diverging characteristic timescale captures the macroscopic behavior of the system, while the second timescale captures the microscopic details of the vertex model. Note that at the solid-fluid transition there is a discontinuous jump in the values of the dashpot constant $\eta_1$ (see Fig 2.2b). This is because at $p_0 = p_c$ the storage and loss shear moduli are identically equal to zero ($G'(\omega_0) = G''(\omega_0) \equiv 0$) due to the vanishing elastic constants ($E_1 = E_2 = 0$), while the dashpot constants can have arbitrary values [see Eqs. (2.5) and (2.8)]. Finally, we note that the values of the spring and dashpot constants are somewhat sensitive to the local energy minimum configuration used to probe the response in the fluid phase. The errorbars in Fig 2.2 show standard deviation for different configurations that were obtained by using the same magnitude of the initial perturbation (see Model and Methods). In Fig. A.6 in the Appendix A, Sec. A.6, we show how the values of the spring and dashpot constants are affected when configurations were obtained by using different magnitudes of the initial perturbation.

Cells in real epithelial tissues are, however, unlikely to have a perfect hexagonal shape and form a honeycomb tiling. The observed tilings are disordered, often with a rather specific distribution of the number of neighbor cells conserved across several species [110]. To mimic the geometry of real tissues, we constructed an ensemble of uncorrelated disordered tilings of polygons corresponding to local energy minima at different values of $p_0$ (see Fig 1.1b and Model and Methods). We then probed the shear rheology of each such configuration following the same procedure as for the hexagonal tilings. Fig 2.3 shows the average storage and shear moduli. We found

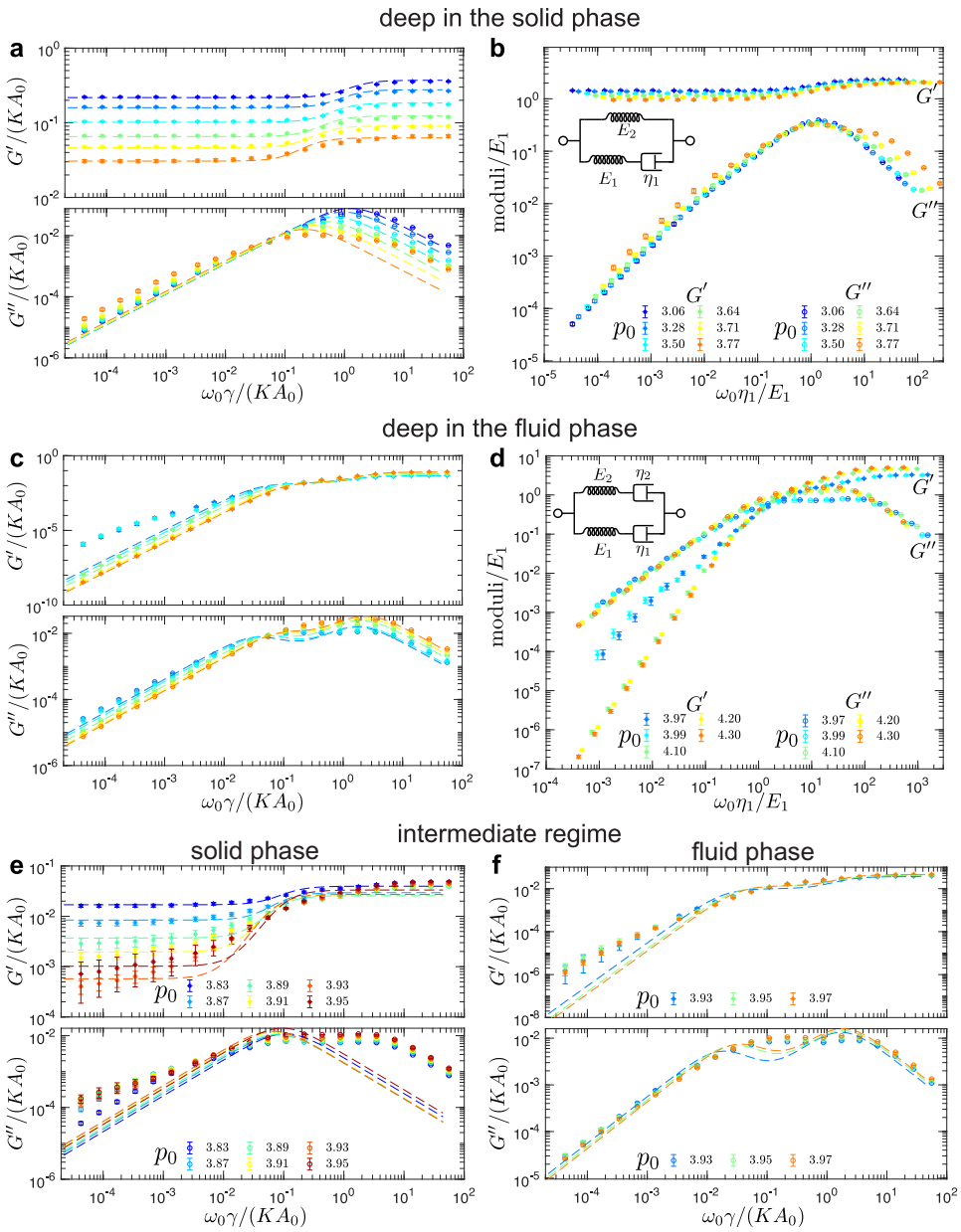


Figure 2.3: Average storage and loss shear moduli in the solid and fluid phase for disordered tilings. (a,c) Average storage ($G'$) and loss ($G''$) shear moduli as functions of the shearing frequency, $\omega_0$, for different values of the cell-shape parameter, $p_0$, (a) deep in the solid phase and (c) deep in the fluid phase. The error bars represent the standard error of the mean. (b,d) The collapse of the moduli curves for different values of $p_0$ for (b) the solid phase and (d) the fluid phase. The insets show the representation of (b) the Standard Linear Solid (SLS) model and (d) the Burgers model in terms of the springs and dashpots. (e,f) Average storage ($G'$) and loss ($G''$) shear moduli as functions of the shearing frequency, $\omega_0$, for intermediate values of the cell-shape parameter, $p_0$, in (e) the solid phase and (f) the fluid phase. Dashed curves are the fits based on (a,e) the SLS model in the solid phase [see Eq. (2.5)] and (c,f) the Burgers model in the fluid phase [see Eq. (2.8)].

that the critical value of $p_0$ for the solid-fluid transition was at $p_c \approx 3.93$, which is consistent with refs. [51, 93], but somewhat higher than what was reported in [23].

For $p_0 < p_c$ values corresponding to the system being deep in the solid phase (Fig 2.3a), the storage and loss moduli are described accurately by the Standard Linear Solid (SLS) model, the same as for the hexagonal tiling in the solid phase (Fig 2.1c). As $p_0$ increases, however, a second shoulder develops in the loss moduli (see $p_0 = 3.71$ and $p_0 = 3.77$ curves in Fig 2.3a), which indicates the presence of multiple time scales. The fits to the SLS model shown with the dashed lines also begin to deviate from the measured moduli. The scaling collapse is only possible for values of $p_0$ deep in the solid phase (Fig 2.3b). This supports the observation that SLS is no longer able to capture the rheology in the solid phase as $p_0$ approaches the critical point.

In the opposite limit, i.e., when the value of $p_0 > p_c$ is deep in the fluid phase (Fig 2.3c), the storage and loss moduli can be modeled with the Burgers model, the same as for the local energy minima states relaxed from the hexagonal tiling in the fluid phase (Fig 2.1d). The fits represented by the dashed lines, however, deviate from the measured moduli as $p_0$ decreases (see $p_0 = 3.97$ and $p_0 = 3.99$ curves in Fig 2.3c). Fig 2.3d shows the rescaling of the moduli and frequencies by the fitted spring and dashpot constants.

Near the critical value (i.e., for $p_0 = 3.93$ and $p_0 = 3.95$), the ensemble of random tilings contains the solid and the fluid configurations (see Fig. A.9 in the Appendix A, Sec. A.9), which was determined based on the presence or absence of non-trivial zero modes. We separated the solid and the fluid configurations and calculated average storage and loss shear moduli on each set. Fig 2.3e and 2.3f show the average storage and loss moduli for values of $p_0$ close to the critical value in the solid phase (Fig 2.3e) and the fluid phase (Fig 2.3f). The dashed curves are the fits based on the SLS model in the solid phase and the Burgers model in the fluid phase, which do not fully

capture the behavior of the measured moduli curves due to the presence of multiple time scales. As the value of $p_0$ approaches the critical value, the spread of the moduli increases, especially for low frequencies, which is captured by the size of error bars. This can also be seen in Fig. A.9 in the Appendix A, Sec. A.9, which presents the raw data of storage and loss shear moduli at different values of $p_0$.

In Fig 2.4, we summarize the fitted values of spring-dashpot models. The values of spring constants decrease as the system approaches the solid-fluid transition, while the values of dashpot constants diverge near the transition. In the intermediate regime (shaded regions in Fig 2.4), the SLS model (in the solid phase) and the Burgers model (in the fluid phase) cannot accurately fit the measured moduli due to the presence of additional timescales.

### 2.2.2 Response to bulk deformations

We further studied the bulk rheological properties of the hexagonal tilings by applying an oscillatory biaxial deformation to the substrate (Fig 2.5a and 2.5b) described by the deformation gradient $\hat{\boldsymbol{F}} = \begin{pmatrix} 1+\epsilon(t) & 0 \\ 0 & 1+\epsilon(t) \end{pmatrix}$, where $\epsilon(t) = \epsilon_0 \sin(\omega_0 t)$. We applied a sufficiently small amplitude $\epsilon_0 = 10^{-7} \ll 1$ to probe the linear response properties

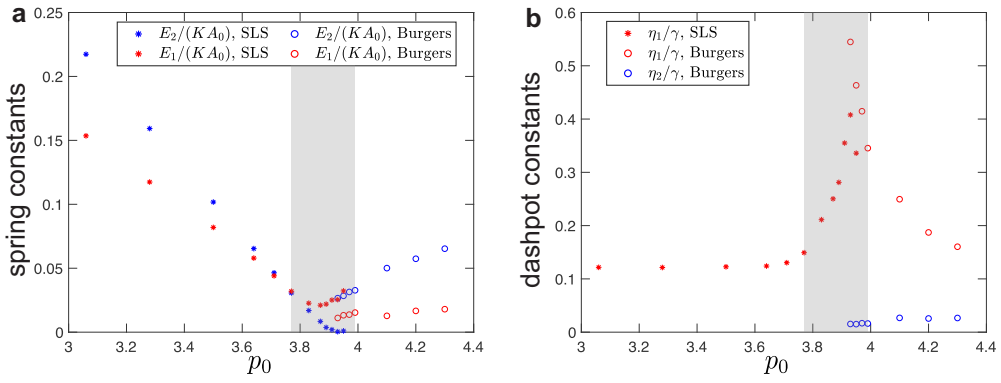


Figure 2.4: Fitted values of spring-dashpot models for disordered tilings under simple shear. (a) Elastic constants as a function of the target cell-shape parameter, $p_0$. (b) Dashpot viscosity constants as a function of the target cell-shape parameter, $p_0$. The shaded regions indicate the intermediate regime between the solid and fluid phases.

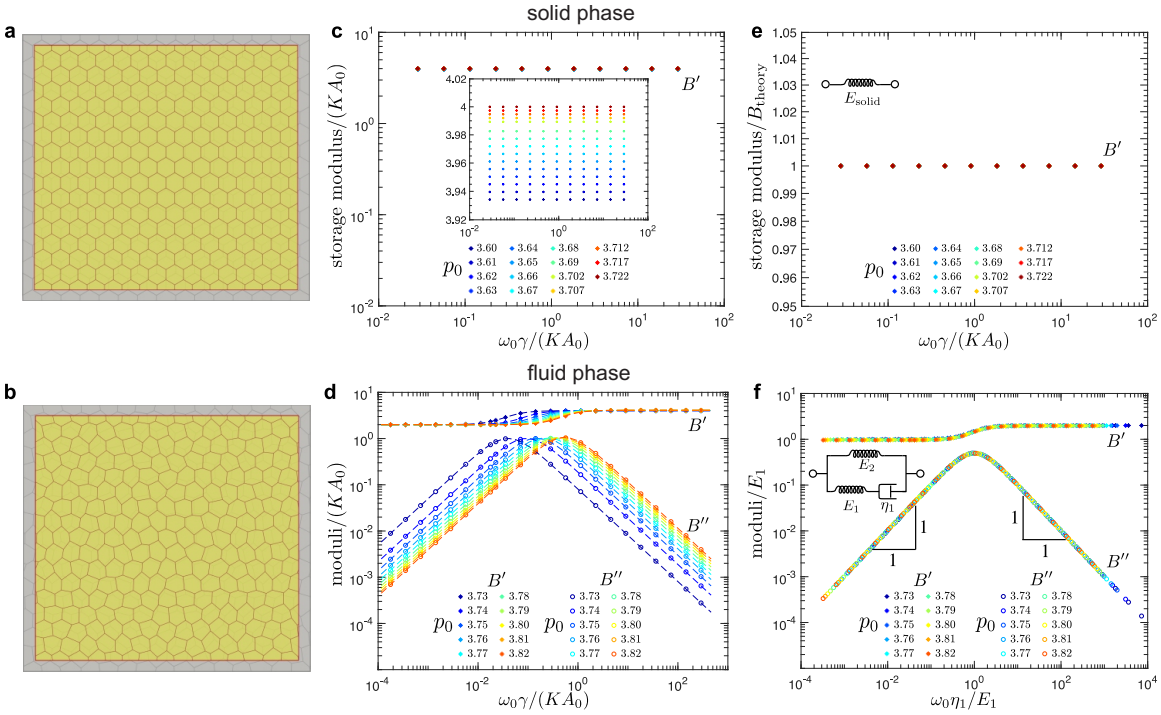


Figure 2.5: Loss and storage bulk moduli in the solid (top row) and fluid phase (bottom row) for hexagonal tilings. (a-b) An overlay of the representative reference (grey) and biaxially deformed (yellow) configurations in (a) the solid and (b) the fluid phase. The magnitude of the bulk deformation is highly exaggerated for demonstration purposes. (c-d) Representative storage ($B'$) and loss ($B''$) bulk moduli as functions of the deformation frequency, $\omega_0$, for different values of the cell-shape parameter, $p_0$. For the solid phase in (c), the loss bulk modulus $B'' \equiv 0$. For the fluid phase in (d), dashed curves are the fits based on the Standard Linear Solid (SLS) model [see Eq. (2.5)]. (e-f) The collapse of the moduli curves for different values of $p_0$ for (e) the solid phase and (f) the fluid phase. The insets show the representation of (e) the spring model and (f) the SLS model in terms of the springs and dashpots. In panel (e), $B_{\text{theory}}$ corresponds to the analytical prediction in Eq. (2.9) for the storage bulk modulus in the solid phase .

characterized by the average normal stress $\sigma(t) = \frac{1}{2}\left[\hat{\sigma}_{xx}(t) + \hat{\sigma}_{yy}(t)\right]$. As in the simple shear test, we then computed the dynamic bulk modulus as $B^*(\omega_0) = \tilde{\sigma}(\omega_0)/\tilde{\epsilon}(\omega_0)$ from which we obtained the storage bulk modulus $B' = \text{Re}\,(B^*)$ and the loss bulk modulus $B'' = \text{Im}\,(B^*)$ (see Fig 2.5c and 2.5d).

In the solid phase, the storage bulk modulus is independent of the driving frequency and the loss bulk modulus is zero. This is because in the solid phase, the hexagonal tiling is stable to biaxial deformation and there is no relative motion of

vertices with respect to the substrate, which is the sole source of dissipation. Thus the response of the system can be captured by a single spring $E_{\text{solid}}$ (Fig 2.5e, inset). The measured value of the storage bulk modulus matches the analytical prediction,

$$B_{\text{theory}} = 2KA_0 + \sqrt[4]{12}\Gamma p_0 \tag{2.9}$$

by Staple, *et al.* [89], where the hexagonal tiling is assumed to undergo affine deformation under biaxial deformation. Storage bulk moduli, normalized by $B_{\text{theory}}$, for different values of $p_0$ all collapse to 1 (Fig 2.5e).

In the fluid phase, the bulk response behavior of the system can be described by the SLS model (Fig 2.5f, inset). While it might appear counter-intuitive to model a fluid with the SLS model, this is a direct consequence of the fact that in the fluid state, the bulk modulus is finite but the shear modulus vanishes, i.e., the fluid flows in response to shear but resists bulk deformation. The fitted storage and loss bulk moduli for the SLS model [see Eq. (2.5)] show an excellent match with the simulation data (Fig 2.5d). This was also confirmed in Fig 2.5f, where we collapsed the storage and loss bulk moduli for different values of $p_0$.

The fitted values of elastic spring and dashpot viscosity constants for different values of $p_0$ are plotted in Fig 2.6. In the fluid phase, the storage bulk modulus in the high frequency limit $B'(\omega_0 \to \infty) = E_1 + E_2$ [see Eq. (2.5)] continuously increases from the value for the solid phase $B_{\text{theory}}$ [see Eq. (2.9)] as the system transitions from solid to fluid (Fig 2.6a). The storage bulk modulus in the quasistatic limit $B'(\omega_0 \to 0) = E_2$ [see Eq. (2.5)] emerges at the transition point with a finite value and increases as $p_0$ increases from $p_c$ (Fig 2.6a). Fig 2.6b shows that the dashpot constant $\eta_1$ diverges as the $p_0$ decreases toward $p_c$. Thus, the characteristic timescale $\eta_1/E_1$ also diverges (Fig 2.6c), but for a different reason than for the shear deformation, where the spring constant $E_1$ is vanishing (see Fig 2.2). Finally, we note that, unlike for the response

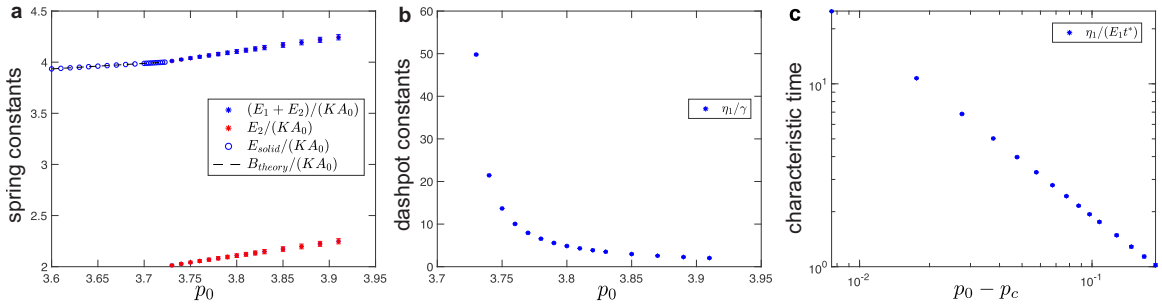


Figure 2.6: Fitted values of spring-dashpot models for the system under bulk deformation as a function of the target cell-shape parameter, $p_0$. (a) Elastic constants as a function of the target cell-shape parameter, $p_0$. In the solid phase ($p_0 < p_c \approx 3.722$), the bulk storage modulus $E_{\text{solid}}$ agrees with the analytical prediction $B_{\text{theory}}$ in Eq. (2.9) (dashed line). At the solid-fluid transition point ($p_0 = p_c \approx 3.722$), it continuously changes to the high frequency limit of the bulk storage modulus, i.e., $B'(\omega_0 \to \infty) = E_1 + E_2$, of the fluid phase. The low frequency limit of the bulk storage modulus is $B'(\omega_0 \to 0) = E_2$ in the fluid phase. (b) Dashpot viscosity constant as a function of the target cell-shape parameter, $p_0$. (c) Characteristic timescales in the fluid phase obtained from the fitted values of the elastic constant and the dashpot viscosity. The normalization factor $t^* = \gamma/(KA_0)$ sets the unit of time. For the fluid phase ($p_0 > p_c \approx 3.722$), errorbars correspond to the standard deviation for simulations that were repeated for configurations that correspond to different local energy minima.

to shear, the values of the spring and dashpot constants for bulk deformation are not sensitive to the local energy minimum configuration used to probe the response in the fluid phase, which is reflected by the very small errorbars in Fig 2.6. This is because the bulk moduli are dominated by the changes in cell areas.

The same procedures were applied to the ensemble of disordered tilings to probe the bulk rheology. Fig 2.7 shows the average storage and loss bulk moduli for different values of $p_0$. When the system is deep in the solid phase (Fig 2.7a) or deep in the fluid phase (Fig 2.7c), the bulk rheology can be described by the SLS model, which is confirmed by the fits (dashed curves) and the collapse in Fig 2.7b and 2.7d. The fitted values of spring and dashpot constants for different values of $p_0$ are shown in Fig 2.8. As $p_0$ approaches the value of solid-fluid transition, the fits based on the SLS model deviate from the measured moduli curves (Fig 2.7a and 2.7c). At intermediate frequencies the storage moduli have a lower slope than predicted by the SLS model

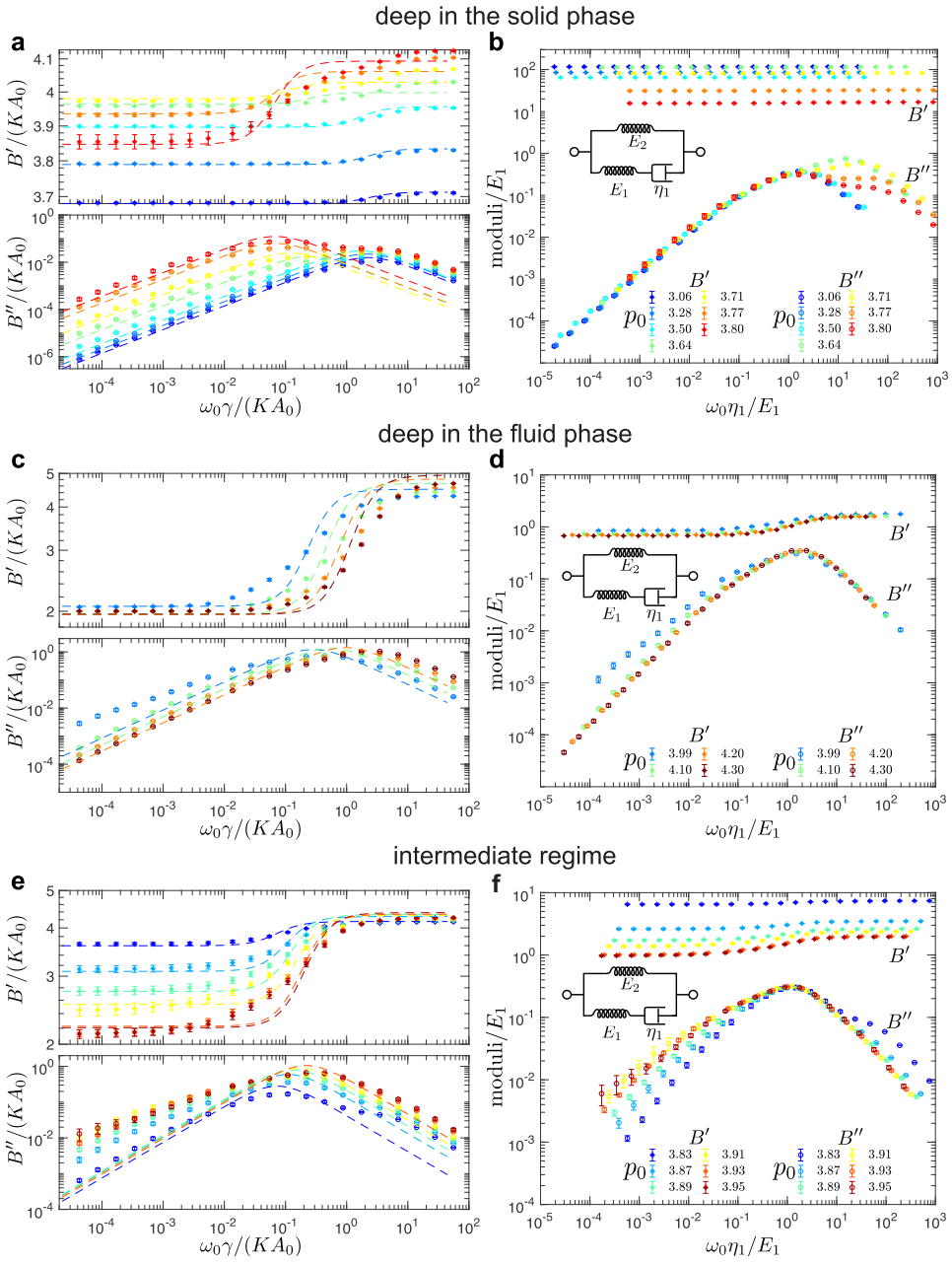


Figure 2.7: Average storage and loss bulk moduli in the solid and fluid phase for disordered tilings. (a,c) Average storage ($B'$) and loss ($B''$) bulk moduli as functions of the deformation frequency, $\omega_0$, for different values of the cell-shape parameter, $p_0$, (a) deep in the solid phase and (c) deep in the fluid phase. The error bars represent the standard error of the mean. (b,d) The collapse of the moduli curves for different values of $p_0$ for (b) the solid phase and (d) the fluid phase. The insets show the representation of the Standard Linear Solid (SLS) model in terms of the springs and dashpots. (e) Average storage ($B'$) and loss ($B''$) bulk moduli as functions of the deformation frequency, $\omega_0$, for intermediate values of the cell-shape parameter, $p_0$. (f) The collapse of the moduli curves for for intermediate values of the cell-shape parameter, $p_0$. Dashed curves in (a,c,e) are the fits based on the SLS model.

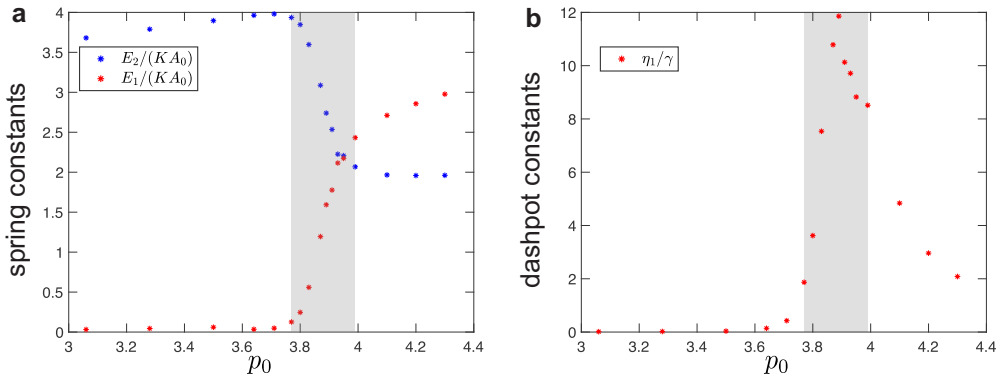


Figure 2.8: Fitted values of spring-dashpot models for disordered tilings under bulk deformation. (a) Elastic constants as a function of the target cell-shape parameter, $p_0$. (b) Dashpot viscosity constant as a function of the target cell-shape parameter, $p_0$. The shaded regions indicate the intermediate regime between the solid and fluid phases.

and the peak in the loss moduli is flattened and a second peaks starts to develop ($p_0 = 3.71$, 3.77, and 3.80 in Fig 2.7a and $p_0 = 3.99$ in Fig 2.7c). Fig 2.7e shows the storage and loss moduli for values of $p_0$ near the solid-fluid transition, and the collapsed data is shown in Fig 2.7f. As the value of $p_0$ approaches the critical value, the spread of the moduli increases, especially for low frequencies, which is seen in Fig. A.10 in the Appendix A, Sec. A.10, that presents the raw data of storage and loss bulk moduli at different values of $p_0$.

### 2.2.3 Response to a shear deformation of a uniaxially pre-deformed system

The solid-fluid transition for the regular hexagonal tiling occurs when $p_0 \approx 3.722$, above which the hexagonal tiling is unstable. This is consistent with the vanishing of the affine shear modulus in Eq. (2.7) at the transition point. If the regular hexagonal tiling is pre-compressed or pre-stretched uniaxially by a factor $a$, which is described by the deformation gradient $\hat{\boldsymbol{F}} = \left(\begin{smallmatrix} a & 0 \\ 0 & 1 \end{smallmatrix}\right)$, then the high frequency limit of the linear storage shear modulus that is dominated by affine deformation becomes (see Appendix

A, Sec. A.7),

$$G'_{\text{affine}}(a) = \frac{2\sqrt{2}\Gamma}{3^{7/4}a}\left(1+\frac{1}{(1+3a^2)^{\frac{3}{2}}}\right)\left(-3p_0+\sqrt[4]{192}\left(1+\sqrt{1+3a^2}\right)\right). \quad (2.10)$$

By setting the affine shear modulus to 0, we obtained the solid-fluid transition boundary in the $a - p_0$ plane as

$$p_c(a) = \sqrt{8\sqrt{3}}\,\frac{\left(1+\sqrt{1+3a^2}\right)}{3}. \quad (2.11)$$

The above analytical prediction for the phase boundary (Fig 2.9a, blue line) shows an excellent agreement with the stability analysis in terms of the eigenvalues of the Hessian matrix $\frac{\partial^2 E}{\partial \mathbf{r}_i \partial \mathbf{r}_j}$ of the energy function [111] (Fig 2.9a, red dots). A given configuration is stable if all eigenvalues of the Hessian matrix are positive and the loss of mechanical stability occurs when the lowest eigenvalue becomes 0. For a given $p_0$, the value of the lowest eigenvalue reduces with decreasing $a$, i.e., as the magnitude of compression is increased. Thus, the compression (stretching) shifts the solid-fluid transition towards the lower (higher) values of $p_0$ (see Fig 2.9a).

We also probed the response to oscillatory shear applied to uniaxially pre-compressed and pre-stretched systems. This analysis was done on the uniaxially deformed hexagonal tiling in the solid phase as well as a system in the fluid phase obtained by relaxing the unstable, uniaxially deformed hexagonal tiling after an initial random perturbation (see Model and Methods). The response to the shear deformation is qualitatively similar and can still be described by the SLS model in the solid phase and the Burgers model in the fluid phase. Fig 2.9b and 2.9c shows fitted values of the parameters for spring-dashpot models when the system is under uniaxial compression ($a = 0.95$), no pre-deformation ($a = 1.00$, i.e., same as Fig 2.2a and 2.2b), and uniaxial tension ($a = 1.05$). In both the solid and fluid phases, all spring elastic constants decrease to 0 as $p_0$ approaches the critical value predicted

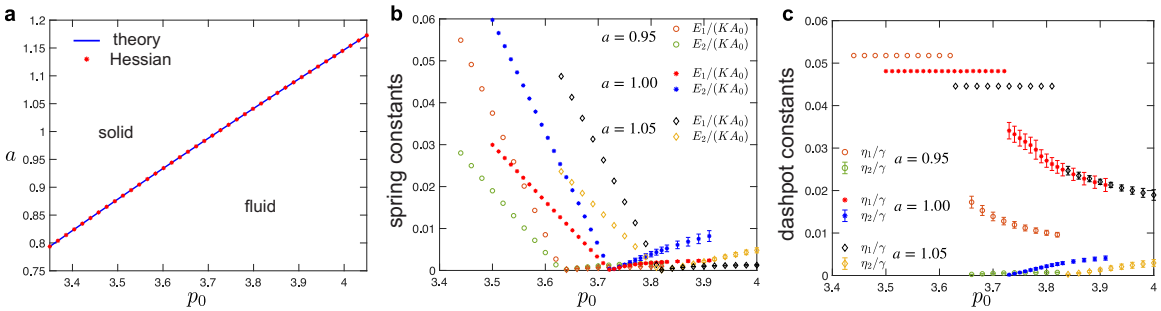


Figure 2.9: Tuning the solid to fluid transition by applying uniaxial pre-deformation. (a) The solid-fluid transition boundary in the $a - p_0$ plane, where $a$ measures the amount of uniaxial pre-deformation described by the deformation gradient $\hat{\boldsymbol{F}} = \left(\begin{smallmatrix} a & 0 \\ 0 & 1 \end{smallmatrix}\right)$. Blue line shows the analytical prediction from Eq. (2.11), which matches the stability analysis with the Hessian matrix (red dots). (b,c) The fitted values of the (b) spring and (c) dashpot constants for the SLS model in the solid phase [see Eq. (2.5)] and the Burgers model in the fluid phase [see Eq. (2.8)] when the system is under uniaxial compression ($a = 0.95$), no pre-deformation ($a = 1.00$), and under uniaxial tension ($a = 1.05$).

by Eq. (2.11). The dashpot constant $\eta_1$ remains constant in the solid phase. Once the system enters the fluid phase as $p_0$ increases, a new dashpot constant $\eta_2$ emerges and increases from 0, while the value of the dashpot constant $\eta_1$ decreases. As in the simple shear case, we note that the dashpot constant $\eta_1$ has a discontinuous jump at the solid-fluid transition (see Fig 2.2c) and that the values of the spring and dashpot constants are somewhat sensitive to the local energy minimum configuration used to probe the response in the fluid phase. The errorbars in Fig 2.2 show standard deviation for configurations that were obtained by using different random initial perturbation (see Model and Methods). Finally, we note that besides the uniaxial pre-deformation, the solid-fluid transition point can be tuned by other modes of pre-deformation (see Fig. A.7 and Appendix A, Sec. A.7).

## 2.3 Conclusion and discussion

In this chapter, we have performed a detailed analysis of the rheological properties of the vertex model subject to small-amplitude oscillatory deformations over seven

orders of magnitude in the driving frequency. Our analysis shows that the vertex model exhibits non-trivial viscoelastic behavior that can be tuned by a single dimensionless geometric parameter - the shape parameter, $p_0$. In order to characterize the response, we constructed constitutive rheological models that use combinations of linear springs and dashpots connected in series and in parallel. These models allowed us to match the shear response of the vertex model to that of the Standard Linear Solid model in the solid phase and the Burgers model in the fluid phase. In the low-frequency, i.e., quasistatic regime, our results are fully consistent with many previous studies [89, 109, 23, 24]. Our work, however, provides insights into the time-dependent response of the vertex model over a broad range of driving frequencies, which is important if one is to develop full understanding of the rheological properties of the vertex model and how they inform our understanding of epithelial tissue rheology.

While the SLS and the Burgers model accurately describe rheology of the vertex model of disordered tilings deep in the solid and liquid phases, respectively, these models deviate from the data for $p_0$ values in the vicinity of the solid-fluid transition. This is because close to the transition points additional relevant time scales start to emerge. As shown in Fig. A.11 in the Appendix A, Sec. A.11, adding additional Maxwell elements in parallel to the spring-dashpot models increases accuracy of the fits. This is to be expected since each Maxwell element introduces a new time scale. The physical interpretation of these additional time scales has clearly to do with the local arrangements of the cells for a particular disordered configuration but tying it to a specific cell pattern is, however, not easy. In addition, we also found that for disordered tilings the loss shear modulus crosses over from the linear scaling in frequency at low $\omega_0$ to the $\sim \omega^\alpha$ with $\alpha \approx 0.73$ at intermediate frequencies (Fig. A.12 in the Appendix A, Sec. A.12). The crossover moves to lower frequencies as the

system size increases. This behavior suggests a large (potentially infinite) number of relevant timescales.

It is important to note that we considered only friction between cells and the substrate and neglected any internal dissipation within the tissue. Therefore, the dissipation is solely due to relative motion of the cells with respect to the substrate as a result of non-affine relaxation of the tissue. The approach used in this study, therefore, would not be suitable for modeling the rheological response of epithelia not supported by a solid substrate, e.g., for early stage embryos or suspended epithelia in the experiments of Harris, et al. [40]. Furthermore, dissipative processes in epithelia are far more complex than simple viscous friction and are not fully understood. It has, for example, recently been argued that internal viscoelastic remodelling of the cortex can lead to interesting collective tissue behaviors [112]. We have addressed some of these questions in chapter 3 using a semi-analytic approach based on the normal-mode expansion.

In this work we kept the ratio $\Gamma/(KA_0)$ fixed, since this ratio does not qualitatively change the behavior of the vertex model [44, 23]. In chapter 3, however, we further explored the effect of parameter $\Gamma/(KA_0)$, where we showed that the perimeter stiffness $\Gamma$ and the area stiffness $K$ affect the low-frequency and high-frequency rheological behavior, respectively.

We also showed that the critical value for the solid-fluid transition can be tuned by applying pre-deformation. Interestingly, under uniaxial and biaxial (i.e., isotropic) pre-compression the solid to fluid transition shifts to lower values of $p_0$, leading to the non-intuitive prediction that one can fluidize the system by compressing it. This is, however, unsurprising, since the transition is driven by a geometric parameter that is inversely proportional to the square root of the cell's native area. Compressing the system reduces its area and, hence, effectively increases $p_0$. It is, however, important to note that this is just a property of the vertex model and it does not necessarily

imply that actual epithelial tissue would behave in the same way. Cells are able to adjust their mechanical properties in response to applied stresses, and it would be overly simplistic to assume that compression would directly lead to changes in the preferred area. In fact, experiments on human bronchial epithelial cells show that applying apical-to-basal compression, which effectively expands the tissue laterally (i.e., corresponds to stretching in our model), fluidizes the tissue [22].

Furthermore, the transition from solid phase to fluid phase is accompanied by the emergence of a large number of soft modes. As we have noted, it has recently been argued that these soft modes lead to a nonlinear response distinct from that obtained in classical models of elasticity [48]. Approximately half of the eigenmodes are zero modes (see Fig. A.8 in the Supporting Information, Sec. A.8). While the analysis of soft modes in the vertex model is an interesting problem [92], it is beyond the scope of this work. Other models in this class have intriguing non-trivial mechanical properties, such as the existence of topologically protected modes [113, 114, 115, 116, 117].

We briefly comment on the values of vertex model parameters and timescales that are relevant for experimental systems. While obtaining accurate in vivo measurements of elastic coefficients of epithelial tissues is notoriously difficult, it is possible to make order of magnitude estimates. For example, recent experiments on human corneal epithelial cells estimated $K/\gamma \approx 0.5\ \mu\mathrm{m}^{-2}\mathrm{h}^{-1}$ and $A_0 \approx 500\ \mu\mathrm{m}^2$ [28]. This would correspond to the timescale $\gamma/(KA_0) \approx 15$ s, or the relevant frequencies in the $\sim 10^0 - 10^2$ Hz range. Characteristic values of stress have been estimated to be $KA_0 \sim 10\,\mathrm{nN}/\mu\mathrm{m}$ for a number of different epithelia [118, 108].

Regardless of whether cells in an epithelial tissue are arrested or able to move, the rheological response of the tissue is viscoelastic with multiple timescales [41]. This response arises as a result of the complex material properties of individual cells combined with four basic cellular behaviors: movement, shape change, division, and

differentiation. The tissue not only has a non-trivial rheological response but is also able to tune it. There is growing evidence that this ability of biological systems to tune their rheology, and in particular, transition between solid-like and fluid-like behaviors, plays a key role during morphogenesis [8]. How such cellular processes are regulated and coordinated to form complex morphological structures is only partly understood. It is, however, clear that the process involves mechano-chemical feedback between mechanical stresses and the expression of genes that control the force-generating molecular machinery in the cell. Any models that aim to describe morphological processes, therefore, need to include coupling between biochemical processes and mechanical responses. The base mechanical model, however, must be able to capture the underlying viscoelastic nature of tissues. Our work provides evidence that the vertex model, a model commonly used to study the mechanics of epithelial tissues, has interesting non-trivial rheological behavior. This, combined with its ability to capture both fluid- and solid-like behavior by tuning a single geometric parameter shows it to be an excellent base model to build more complex descriptions of real tissues.

# Chapter 3

# Linear viscoelastic response of the vertex model with internal and external dissipation: normal modes analysis

In this chapter, We use the normal mode formalism to study the shear rheology of the vertex model for epithelial tissue mechanics in the overdamped linear response regime. We consider systems with external (e.g., cell-substrate) and internal (e.g., cell-cell) dissipation mechanisms, and derive expressions for stresses on cells due to mechanical and dissipative forces. The semi-analytical method developed here is, however, general and can be directly applied to study the linear response of a broad class of soft matter systems with internal and external dissipation. It involves normal mode decomposition to calculate linear loss and storage moduli of the system. Specifically, displacements along each normal mode produce stresses due to elastic deformation and internal dissipation, which are in force balance with loads due to external dissipation. Each normal mode responds with a characteristic relaxation timescale, and its rheo-

logical behavior can be described as a combination of a standard linear solid element due to elastic stresses and a Jeffreys model element due to the internal dissipative stresses. The total response of the system is then fully determined by connecting in parallel all the viscoelastic elements corresponding to individual normal modes. This allows full characterization of the potentially complex linear rheological response of the system at all driving frequencies and identification of collective excitations. We show that internal and external dissipation mechanisms lead to qualitatively different rheological behaviors due to the presence or absence of Jeffreys elements, which is particularly pronounced at high driving frequencies.

## 3.1 Normal Modes Analysis

We model a soft viscoelastic system as a collection of $N$ interacting agents (e.g., vertices of a network, colloids in colloidal dispersion, cells in a tissue, etc.) whose interaction is described by a potential energy $E(\{\mathbf{R}_j\})$, where $\{\mathbf{R}_j\}$ denotes the set of position vectors of all agents in a suitably chosen reference frame. The position vector of agent $j$ is $\mathbf{R}_j \in \mathbb{R}^d$ with $d$ being the number of spacial dimensions and $j \in \{1, \ldots, N\}$. In general, the potential energy can be multi-body, and each agent $i$ experiences the force $-\nabla_{\mathbf{R}_i} E(\{\mathbf{R}_j\})$. To simplify the notation, we introduce the column vector $\mathbf{r} \equiv (\mathbf{R}_1, \ldots, \mathbf{R}_N)$, which contains positions of all agents, i.e., $\mathbf{r} \in \mathbb{R}^{dN}$. Similarly, a $dN$-dimensional vector, $-\nabla_{\mathbf{r}} E(\mathbf{r})$, represents forces acting on all agents. Since typical systems of interests are in the overdamped regime, the relaxation dynamics of the system in the absence of an external driving force is described as

$$\hat{\boldsymbol{C}}\dot{\mathbf{r}}(t) = -\nabla_{\mathbf{r}} E\big(\mathbf{r}(t)\big), \tag{3.1}$$

where the symmetric matrix $\hat{\boldsymbol{C}}$ provides a generalization of the single friction coefficient to more complex mechanisms of energy dissipation, which captures both external

and internal dissipation. The overdot symbol is used to denote the time derivative of relevant quantities throughout this chapter.

We are interested in the linear response of the system around an equilibrium state $\mathbf{r}^{\mathrm{eq}}$, which corresponds to a solution of the set of algebraic equations,

$$\nabla_{\mathbf{r}} E\big|_{\mathbf{r}=\mathbf{r}^{\mathrm{eq}}} = 0. \tag{3.2}$$

In order to probe the linear response, we consider an external driving force $\mathbf{f}(t)$ that is sufficiently weak to produce deformations that are small compared to the typical distance between agents, i.e., it keeps the system in the basin of attraction of the local energy minimum. The corresponding displacements are $\delta\mathbf{r}(t) = \mathbf{r}(t) - \mathbf{r}^{\mathrm{eq}}$ and linearized equations of motion take the form

$$\hat{\boldsymbol{C}}\delta\dot{\mathbf{r}}(t) = -\hat{\boldsymbol{H}}\delta\mathbf{r}(t) + \mathbf{f}(t), \tag{3.3}$$

where $\hat{\boldsymbol{H}}$ is the Hessian matrix with elements

$$\hat{H}_{IJ} = \left.\frac{\partial^2 E}{\partial x_I \partial x_J}\right|_{\mathbf{r}=\mathbf{r}^{\mathrm{eq}}}. \tag{3.4}$$

Here, $x_I$ and $x_J$ are, respectively, the $I^{\mathrm{th}}$ and $J^{\mathrm{th}}$ entries in the vector $\mathbf{r}$. Recall that $\hat{\boldsymbol{H}}$ is a real $dN \times dN$ symmetric matrix. If $\mathbf{r}^{\mathrm{eq}}$ corresponds to a true local energy minimum, then $\hat{\boldsymbol{H}}$ is positive definite. Here, we relax this condition and assume that $\hat{\boldsymbol{H}}$ is positive semi-definite, i.e., we allow for the possibility that zero-energy modes are present in the system. Furthermore, in general, matrices $\hat{\boldsymbol{H}}$ and $\hat{\boldsymbol{C}}$ do not commute.

In order to solve Eq. (3.3), we consider the following generalized eigenvalue problem, [119]

$$\hat{\boldsymbol{H}}\boldsymbol{\xi}_k = \lambda_k \hat{\boldsymbol{C}}\boldsymbol{\xi}_k, \tag{3.5}$$

where $\lambda_k$ and $\boldsymbol{\xi}_k$ are the $k^{\text{th}}$ eigenvalue and eigenvector, respectively. Since $\hat{\boldsymbol{H}}$ and $\hat{\boldsymbol{C}}$ are real symmetric matrices, the eigenvectors form a complete orthonormal basis $\mathcal{B} = \{\boldsymbol{\xi}_i | i = 1, \ldots, dN\}$, i.e., $\langle \boldsymbol{\xi}_i, \boldsymbol{\xi}_j \rangle_{\hat{\boldsymbol{C}}} = \delta_{ij}$, where $\delta_{ij}$ is the Kronecker delta and the inner product is defined as $\langle \mathbf{u}, \mathbf{v} \rangle_{\hat{\boldsymbol{C}}} \equiv \mathbf{u}^\intercal \hat{\boldsymbol{C}} \mathbf{v}$. We can expand the displacement $\delta\mathbf{r}(t)$ in the basis $\mathcal{B}$ as

$$\delta\mathbf{r}(t) = \sum_{k=1}^{dN} a_k(t) \boldsymbol{\xi}_k, \tag{3.6}$$

where $a_k(t)$ is the time-dependent amplitude of the normal mode $\boldsymbol{\xi}_k$. Equations of motion of the system in Eq. (3.3) can then be projected along each normal mode. Since normal modes are orthogonal to each other and, hence, decoupled, each behaves as an independent overdamped harmonic oscillator. The projection, therefore, leads to a set of decoupled dynamical equations for the amplitudes $a_k(t)$ of normal modes,

$$\dot{a}_k(t) = -\lambda_k a_k(t) + f_k(t), \tag{3.7}$$

where $f_k(t) = \boldsymbol{\xi}_k^\intercal \mathbf{f}(t)$ is the projection of the driving force along the $k^{\text{th}}$ normal mode. We immediately see that $\lambda_k^{-1}$ is the characteristic relaxation time of the $k^{\text{th}}$ normal mode. For a given driving force $f_k$(t), Eq. (3.7) can be solved as

$$a_k(t) = a_k(0) e^{-\lambda_k t} + \int_0^t dt' f_k(t') e^{-\lambda_k (t - t')}. \tag{3.8}$$

Thus, once the external driving force $\mathbf{f}(t)$ is specified, the dynamics of the system is fully determined by Eqs. (3.6)-(3.8). Finally, Eq. (3.7) has a simple solution in the frequency domain

$$\tilde{a}_k(\omega) = \frac{\tilde{f}_k(\omega)}{\lambda_k + i\omega}, \tag{3.9}$$

where the Fourier transform is defined as $\tilde{g}(\omega) = \int_{-\infty}^{+\infty} dt\, g(t) e^{-i\omega t}$.

### 3.1.1 Application of normal modes to 2d systems with periodic boundaries under shear

As an example of the general formalism presented above, we now demonstrate how to extract linear shear rheological properties of a $d = 2$–dimensional system with periodic boundary conditions. Treating systems with open boundaries would be analogous, but one would have to solve the generalized eigenvalue problem in Eq. (3.5) subject to the appropriate boundary conditions. In numerical experiments, it is convenient to apply external driving via a macroscopic affine deformation of the entire system and measure the stress response in the system. [120, 121] One way of achieving this in a real system could be by placing the system on a sticky substrate and applying oscillatory shear deformation to the substrate. Due to interactions with the substrate, the deformation of the system follows the deformation of the substrate on short timescales, but the system can relax and produce non-affine motion on longer timescales. We remark that non-affine relaxation plays an important role in many soft systems, e.g., it is key for understanding the elastic properties of amorphous solids. [122]

The affine deformation can be described as $\mathbf{R}_i(t) = \hat{\boldsymbol{F}}(t)\mathbf{R}_i^0$ where the initial position $\mathbf{R}_i^0 \equiv \mathbf{R}_i(t = 0)$ of agent $i$ is mapped to the current position $\mathbf{R}_i(t)$ by an affine deformation gradient tensor $\hat{\boldsymbol{F}}(t)$. [123] For instance, the shear rheology of the system can be probed by applying an oscillatory affine simple shear described by the deformation gradient tensor

$$\hat{\boldsymbol{F}} = \begin{pmatrix} 1 & \epsilon(t) \\ 0 & 1 \end{pmatrix}, \tag{3.10}$$

where $\epsilon(t) = \epsilon_0 \sin(\omega_0 t)$ is the applied shear strain with amplitude $\epsilon_0 \ll 1$. The non-affine relaxation can be described by modifying the force balance in Eq. (3.1) as

$$\hat{\boldsymbol{C}}\big(\dot{\mathbf{r}}(t) - \mathbf{v}^{\text{aff}}(t)\big) = -\nabla_{\mathbf{r}} E\big(\mathbf{r}, \epsilon(\mathbf{t})\big). \tag{3.11}$$

Here, vector $\mathbf{v}^{\text{aff}}(t)$ contains the velocities of all agents due to the affine deformation imposed by the substrate, i.e., $\mathbf{v}^{\text{aff}} \equiv \left(\mathbf{V}_1^{\text{aff}}, \ldots, \mathbf{V}_N^{\text{aff}}\right)$, where $\mathbf{V}_i^{\text{aff}}(t) = \left(\frac{d}{dt}\hat{\boldsymbol{F}}(t)\right)\mathbf{R}_i^0$ is the affine part of the velocity of each individual agent. For the applied simple shear deformation in Eq. (3.10), the affine velocity of agent $i$ is $\mathbf{V}_i^{\text{aff}} = \left(\dot{\epsilon}(t)R_i^{0,y}, 0\right)$, where $R_i^{0,y}$ is the $y-$coordinate of the agent $i$ in the initial position, and the periodic box is centered at the origin.

It is important to note that for a system with periodic boundary conditions, the energy, $E\left(\mathbf{r}, \epsilon(\mathbf{t})\right)$, also depends on the applied shear strain $\epsilon(t)$. This dependence enters via the $x$-component of the separation distance $R_{ij}^x$ between agents $i$ and $j$ as $R_{ij}^x = R_j^x - R_i^x + q_{ij}^x \ell_x + \epsilon(t) q_{ij}^y \ell_y$. [32] Here, $R_i^x$ and $R_j^x$ are the $x$-coordinates of the agents $i$ and $j$, respectively, $\ell_x$ and $\ell_y$ are the sizes of the rectangular simulation box in the $x$ and $y$ directions, respectively. $q_{ij}^y = 0$ if agents $i$ and $j$ are connected without crossing the top or the bottom boundary and $q_{ij}^y = +1$ ($q_{ij}^y = -1$) if the bond connecting agent $i$ to agent $j$ crosses the top (bottom) boundary, with analogous expressions for $q_{ij}^x$ in terms of the left and right boundaries. [32]

Due to the dependence of the energy on the applied shear strain $\epsilon(t)$, the linearized equations of motion in Eq. (3.11) around the equilibrium state $\mathbf{r}^{\text{eq}}$ become

$$\hat{\boldsymbol{C}}\delta\dot{\mathbf{r}}(t) = -\hat{\boldsymbol{H}}\delta\mathbf{r}(t) + \overline{\mathbf{f}}^{\text{pb}}\epsilon(t) + \hat{\boldsymbol{C}}\mathbf{u}^{\text{aff}}\dot{\epsilon}(t). \tag{3.12}$$

Here, we introduced the driving force $\overline{\mathbf{f}}^{\text{pb}} = -\frac{\partial^2 E}{\partial \mathbf{r} \partial \epsilon}\Big|_{\mathbf{r}=\mathbf{r}^{\text{eq}}, \epsilon=0}$ due to periodic boundaries and rewrote the affine velocity as $\mathbf{v}^{\text{aff}} = \mathbf{u}^{\text{aff}}\dot{\epsilon}(t)$, where $\mathbf{u}^{\text{aff}} = \left(\mathbf{U}_1^{\text{aff}}, \ldots, \mathbf{U}_N^{\text{aff}}\right)$ with $\mathbf{U}_i^{\text{aff}} = (R_i^{0,y}, 0)$. As discussed above, the displacements can be expanded in the basis of normal modes as in Eq. (3.6). In this basis, the equations of motions in Eq. (3.12) become

$$\dot{a}_k(t) = -\lambda_k a_k(t) + \alpha_k \epsilon(t) + \beta_k \dot{\epsilon}(t), \tag{3.13}$$

where

$$\alpha_k = \boldsymbol{\xi}_k^{\intercal}\, \overline{\mathbf{f}}^{\mathrm{pb}}, \tag{3.14a}$$

$$\beta_k = \langle \boldsymbol{\xi}_k, \mathbf{u}^{\mathrm{aff}} \rangle_{\hat{\boldsymbol{C}}} = \boldsymbol{\xi}_k^{\intercal} \hat{\boldsymbol{C}} \mathbf{u}^{\mathrm{aff}}. \tag{3.14b}$$

The solution of Eq. (3.13) in the frequency domain is

$$\tilde{a}_k(\omega) = \left( \frac{\alpha_k + i\omega\beta_k}{\lambda_k + i\omega} \right) \tilde{\epsilon}(\omega). \tag{3.15}$$

### 3.1.2 Stresses in 2d systems with periodic boundaries

We measure the stress response of the system due to an external driving force as follows. The stress of the system has two contributions. One contribution is denoted as $\hat{\boldsymbol{\sigma}}^{\mathrm{e}}(t)$, and is generated by the interaction forces $-\nabla_{\mathbf{r}} E\left(\mathbf{r}\right)$ resulting from the elastic deformation. The other contribution is due to the internal dissipation resulting from the relative motion of agents with respect to each other, and it is denoted as $\hat{\boldsymbol{\sigma}}^{\mathrm{id}}(t)$. Note that the loads $\mathbf{f}^{\mathrm{ext}}(t)$ due to external dissipation induce stresses in the system via the force balance relation $\nabla \cdot (\hat{\boldsymbol{\sigma}}^{\mathrm{e}} + \hat{\boldsymbol{\sigma}}^{\mathrm{id}}) + \mathbf{f}^{\mathrm{ext}} = 0$. In Appendix B.4, we show a detailed derivation of these stress contributions for cells in the vertex model. Similar steps can be followed to derive the relevant expressions for stresses $\hat{\boldsymbol{\sigma}}^{\mathrm{e}}$ and $\hat{\boldsymbol{\sigma}}^{\mathrm{id}}$ for any other system.

In the linear response regime, the displacement perturbed from the equilibrium state $\delta\mathbf{r}(t)$ can be written as a linear superposition of displacements along normal modes. The response stress $\hat{\boldsymbol{\sigma}}^{\mathrm{e}}(t)$ due to the elastic deformation can thus be represented as a linear superposition of stress tensors $\hat{\boldsymbol{\sigma}}_k^{\mathrm{e}}(t) = a_k(t)\hat{\boldsymbol{\sigma}}_k^{\mathrm{e,lin}}$ due to the motion along each normal mode $k$ (see Fig. 3.1, top right). The linear response tensor $\hat{\boldsymbol{\sigma}}_k^{\mathrm{e,lin}}$ for $k^{\mathrm{th}}$ normal mode can be calculated by measuring the response stress tensor $\delta\hat{\boldsymbol{\sigma}}_k^{\mathrm{e}}$

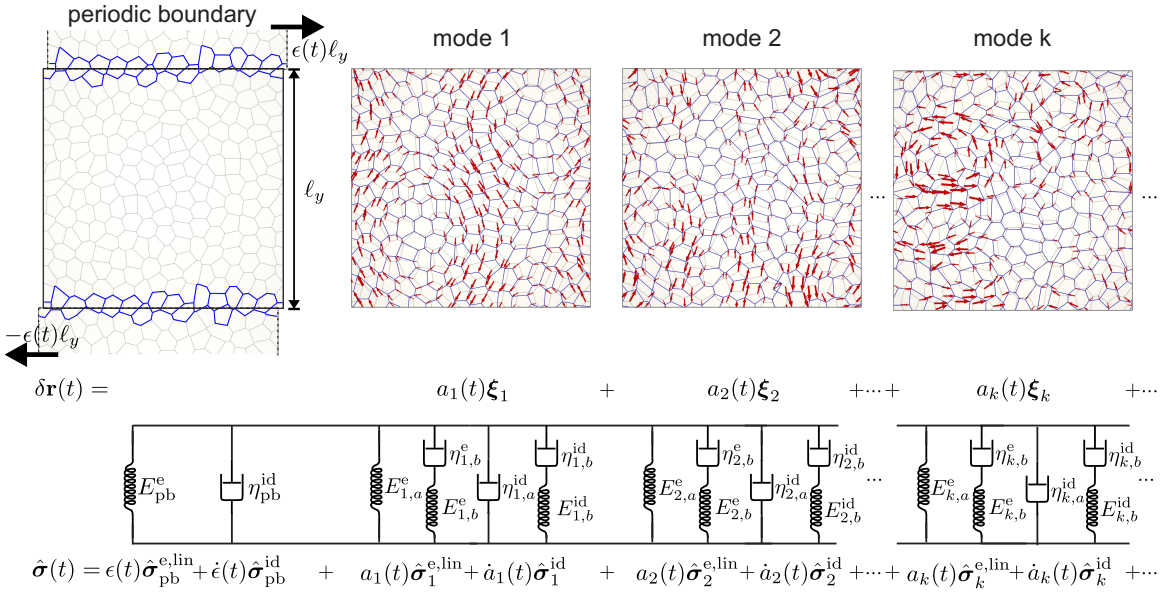


Figure 3.1: A schematic of the decomposition of the motion and the response stress along normal modes. The top left panel depicts the deformation of cells crossing the periodic boundary due to the relative motion of image boxes that are displaced according to the applied shear. The remaining panels show three representative normal modes for the vertex model. The grey mesh is the equilibrium configuration, the red arrows indicate displacements associated with the normal mode $\boldsymbol{\xi}_k$, and the blue mesh is the configuration after displacing vertices in the direction of the normal mode. Similarly, in the top left panel polygons outlined in blue indicate the distorted cells due to the relative movement of image boxes under applied shear. Perturbation from the equilibrium state $\delta\mathbf{r}(t)$ can be written as a linear superposition of displacements along the normal modes $\boldsymbol{\xi}_k$. The stress response of the system [see Eq. (3.18)] due to shear deformation can be represented as a linear superposition of stresses $\epsilon(t)\hat{\boldsymbol{\sigma}}^{\rm e,lin}_{\rm pb}$ and $\dot{\epsilon}(t)\hat{\boldsymbol{\sigma}}^{\rm id}_{\rm pb}$ due to the elastic deformation and internal dissipation of cells crossing the periodic boundary, respectively, and stresses $a_k(t)\hat{\boldsymbol{\sigma}}^{\rm e,lin}_k$ and $\dot{a}_k(t)\hat{\boldsymbol{\sigma}}^{\rm id}_k$ due to the elastic deformation and internal dissipation of the $k^{\rm th}$ normal mode, respectively. The rheological response of the system due to shear deformation [see Eq. (3.21)] can thus be represented as a parallel sequence of a spring and a dashpot due to shear of cells crossing the periodic boundary and standard linear solid (SLS) model elements and Jeffreys model elements, where each SLS model element and Jeffreys model element describe the shear response of a normal mode. Expressions for spring constants and dashpot viscosities are given in the text.

due to perturbation $\delta\mathbf{r} = \delta a\boldsymbol{\xi}_k$ along mode $k$ so that $\hat{\boldsymbol{\sigma}}^{\rm e,lin}_k = \delta\hat{\boldsymbol{\sigma}}^{\rm e}_k/\delta a$, where the amplitude $\delta a$ is sufficiently small to produce deformations that are small compared to the typical distance between agents. There is an additional stress contribution due to the deformation of elastic bonds that cross the periodic boundary. This is because

the displacements $\boldsymbol{\xi}_k$ of normal modes are periodic and they do not capture the relative displacement between the agent $i$ and its periodic image when the affine shear is applied. To account for that, we also consider stresses $\hat{\boldsymbol{\sigma}}^{\mathrm{e}}_{\mathrm{pb}}(t) = \epsilon(t)\hat{\boldsymbol{\sigma}}^{\mathrm{e,lin}}_{\mathrm{pb}}$ due to the deformation of the elastic bonds that cross periodic boundaries when the periodic images of the system are displaced according to the applied shear (see Fig. 3.1, top left). The linear response tensor $\hat{\boldsymbol{\sigma}}^{\mathrm{e,lin}}_{\mathrm{pb}}$ can be calculated by applying a small shear $\delta\epsilon_0 \ll 1$ to the periodic boundary, and measuring the resulting stress $\delta\hat{\boldsymbol{\sigma}}^{\mathrm{e}}_{\mathrm{pb}}$ so that $\hat{\boldsymbol{\sigma}}^{\mathrm{e,lin}}_{\mathrm{pb}} = \delta\hat{\boldsymbol{\sigma}}^{\mathrm{e}}_{\mathrm{pb}}/\delta\epsilon_0$. Therefore, the total elastic stress tensor is

$$\hat{\boldsymbol{\sigma}}^{\mathrm{e}}(t) = \epsilon(t)\hat{\boldsymbol{\sigma}}^{\mathrm{e,lin}}_{\mathrm{pb}} + \sum_k a_k(t)\hat{\boldsymbol{\sigma}}^{\mathrm{e,lin}}_{k}. \tag{3.16}$$

The stresses $\hat{\boldsymbol{\sigma}}^{\mathrm{id}}(t)$ generated by the internal dissipation, i.e., the motion of agents relative to each other, are proportional to the velocities of the agents. The velocity is expanded in the basis $\mathcal{B}$ as $\delta\dot{\mathbf{r}}(t) = \sum_k \dot{a}_k(t)\boldsymbol{\xi}_k$. The stress tensor $\hat{\boldsymbol{\sigma}}^{\mathrm{id}}(t)$ can thus be written as a linear superposition,

$$\hat{\boldsymbol{\sigma}}^{\mathrm{id}}(t) = \dot{\epsilon}(t)\hat{\boldsymbol{\sigma}}^{\mathrm{id}}_{\mathrm{pb}} + \sum_k \dot{a}_k(t)\hat{\boldsymbol{\sigma}}^{\mathrm{id}}_{k}, \tag{3.17}$$

where $\dot{\epsilon}(t)\hat{\boldsymbol{\sigma}}^{\mathrm{id}}_{\mathrm{pb}}$ is the dissipative stress due to the relative motion of agents when the periodic images of the system are displaced according to the applied shear, and $\hat{\boldsymbol{\sigma}}^{\mathrm{id}}_{k}$ is the dissipative stress generated by the $k^{\mathrm{th}}$ normal mode. Note that the stresses due to internal dissipation are linear by definition because the dissipative forces depend linearly on the agent velocities [see Eq. (3.1)]. Then the total stress is

$$\begin{aligned}
\hat{\boldsymbol{\sigma}}(t) &= \hat{\boldsymbol{\sigma}}^{\mathrm{e}}(t) + \hat{\boldsymbol{\sigma}}^{\mathrm{id}}(t), \\
\hat{\boldsymbol{\sigma}}(t) &= \epsilon(t)\hat{\boldsymbol{\sigma}}^{\mathrm{e,lin}}_{\mathrm{pb}} + \sum_k a_k(t)\hat{\boldsymbol{\sigma}}^{\mathrm{e,lin}}_{k} \\
&\quad + \dot{\epsilon}(t)\hat{\boldsymbol{\sigma}}^{\mathrm{id}}_{\mathrm{pb}} + \sum_k \dot{a}_k(t)\hat{\boldsymbol{\sigma}}^{\mathrm{id}}_{k}.
\end{aligned} \tag{3.18}$$

### 3.1.3 Storage and loss moduli in 2d systems with periodic boundaries

For the shear rheology, the dynamic shear modulus is defined as, [107]

$$\begin{aligned} G^*(\omega) = \frac{\tilde{\hat{\sigma}}_{xy}(\omega)}{\tilde{\epsilon}(\omega)} = \quad & G^{\mathrm{e}}_{\mathrm{pb}} + \sum_k \left( \frac{\alpha_k + i\omega\beta_k}{\lambda_k + i\omega} \right) G^{\mathrm{e}}_k \\ & + i\omega G^{\mathrm{id}}_{\mathrm{pb}} + \sum_k i\omega \left( \frac{\alpha_k + i\omega\beta_k}{\lambda_k + i\omega} \right) G^{\mathrm{id}}_k, \end{aligned} \tag{3.19}$$

where $G^{\mathrm{e}}_{\mathrm{pb}} \equiv \hat{\sigma}^{\mathrm{e,lin}}_{\mathrm{pb},xy}$ and $G^{\mathrm{id}}_{\mathrm{pb}} \equiv \hat{\sigma}^{\mathrm{id}}_{\mathrm{pb},xy}$ are the moduli due to the shear of the periodic boundary and

$$G^{\mathrm{e}}_k \equiv \hat{\sigma}^{\mathrm{lin}}_{k,xy}, \tag{3.20a}$$

$$G^{\mathrm{id}}_k \equiv \hat{\sigma}^{\mathrm{id}}_{k,xy}. \tag{3.20b}$$

Note that $G^{\mathrm{id}}_{\mathrm{pb}}$, $G^{\mathrm{e}}_k$, and $G^{\mathrm{id}}_k$ themselves do not have units of stress. We, however, use the letter "G" to emphasize their contributions to the dynamic moduli, which have units of stress. In general, the dynamic shear modulus $G^*(\omega) = G'(\omega) + iG''(\omega)$ has a real part $G'$, which is called the storage modulus, and an imaginary part $G''$, which is called the loss modulus. [107] Using Eq. (3.19), one can write the storage and loss moduli as

$$\begin{aligned} G'(\omega) = & G^{\mathrm{e}}_{\mathrm{pb}} + \sum_k \left( \frac{\alpha_k \lambda_k + \beta_k \omega^2}{\lambda_k^2 + \omega^2} \right) G^{\mathrm{e}}_k \\ & - \sum_k \left( \frac{(-\alpha_k + \beta_k \lambda_k)\omega^2}{\lambda_k^2 + \omega^2} \right) G^{\mathrm{id}}_k, \end{aligned} \tag{3.21a}$$

$$G''(\omega) = \omega G^{\mathrm{id}}_{\mathrm{pb}} + \sum_k \left( \frac{(-\alpha_k + \beta_k \lambda_k)\omega}{\lambda_k^2 + \omega^2} \right) G^{\mathrm{e}}_k + \sum_k \left( \frac{(\alpha_k \lambda_k + \beta_k \omega^2)\omega}{\lambda_k^2 + \omega^2} \right) G^{\mathrm{id}}_k . \tag{3.21b}$$

Upon a closer inspection of the expressions for the storage and loss moduli, we recognize that the contributions due to periodic boundaries can be represented as a Kelvin-Voigt element and that each normal mode $k$ behaves as a standard linear solid element connected in parallel with a Jeffreys element. [107] The Kelvin-Voigt element can be represented as a spring $E^{\mathrm{e}}_{\mathrm{pb}} = G^{\mathrm{e}}_{\mathrm{pb}}$ connected in parallel with a dashpot $\eta^{\mathrm{id}}_{\mathrm{pb}} = G^{\mathrm{id}}_{\mathrm{pb}}$. The standard linear solid element can be represented as a spring with elastic constant $E^{\mathrm{e}}_{k,a} = G^{\mathrm{e}}_k \alpha_k / \lambda_k$ connected in parallel with a Maxwell element that consists of a spring $E^{\mathrm{e}}_{k,b} = G^{\mathrm{e}}_k(-\alpha_k + \beta_k \lambda_k)/\lambda_k$ and a dashpot $\eta^{\mathrm{e}}_{k,b} = G^{\mathrm{e}}_k(-\alpha_k + \beta_k \lambda_k)/\lambda_k^2$ connected in series (see Fig. 3.1). The Jeffreys model element can be represented as a dashpot $\eta^{\mathrm{id}}_{k,a} = G^{\mathrm{id}}_k \beta_k$ connected in parallel with a Maxwell element that consists of a spring $E^{\mathrm{id}}_{k,b} = G^{\mathrm{id}}_k(\alpha_k - \beta_k \lambda_k)$ and a dashpot $\eta^{\mathrm{id}}_{k,b} = G^{\mathrm{id}}_k(\alpha_k - \beta_k \lambda_k)/\lambda_k$ (see Fig. 3.1). The characteristic time scale for mode $k$ is, therefore, $\eta^{\mathrm{e}}_{k,b}/E^{\mathrm{e}}_{k,b} = \eta^{\mathrm{id}}_{k,b}/E^{\mathrm{id}}_{k,b} = 1/\lambda_k$. The full rheological response of the system can thus be represented as a Kelvin-Voigt element due to periodic boundary and a sequence of standard linear solid elements and Jeffreys model elements connected in parallel, each standard linear solid element and Jeffreys model element corresponding to the contribution from one normal mode (see Fig. 3.1). The dynamic response of the system is, therefore, characterized by a spectrum of relaxation timescales $\lambda_k^{-1}$ corresponding to each normal mode.

Finally, we note that the contribution to the loss modulus due to internal dissipation scales as $G''(\omega) \sim \omega$ at high frequencies [see Eq. (3.21b)]. This is in contrast to the case with external dissipation only, where the loss modulus scales as $G''(\omega) \sim 1/\omega$ [see Eq. (3.21b)]. Thus, in general, at high frequencies, the loss modulus increases linearly with frequency and is dominated by internal dissipation. As we show below, the onset of the crossover to the linear scaling of the loss modulus with $\omega$ in systems

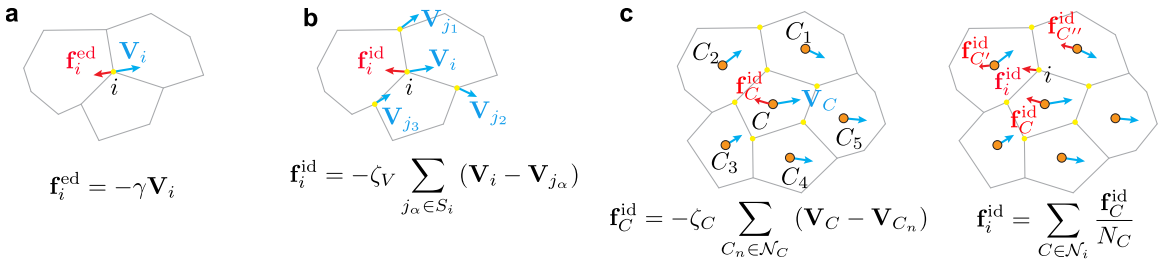


Figure 3.2: Schematics of the three types of dissipation mechanisms in the vertex model considered in this chapter. Velocity vectors are shown in blue and friction forces are red. (a) Dissipation due to the relative motion between vertices and a solid substrate. Vertex $i$ experiences a frictional force proportional to its velocity $\mathbf{V}_i$, with friction coefficient $\gamma$. (b) Friction force on the vertex $i$ is due to its motion relative to neighboring vertices. $\mathcal{S}_i$ is the set of all vertices connected to vertex $i$ by a cell-cell junction. (c) Dissipation is due to the relative motion of neighboring cell centers. $\mathcal{N}_C$ includes all neighboring cells of cell $C$. $\mathcal{N}_i$ includes all cells that share vertex $i$. $\mathbf{f}_C^{\mathrm{id}}$ is the friction force that cell $C$ experiences due to relative motion with respect to its neighboring cells. $\mathbf{f}_i^{\mathrm{ed}}$ and $\mathbf{f}_i^{\mathrm{id}}$ are the total friction forces applied at vertex $i$ due to external and internal dissipation, respectively. $N_C$ is the number of vertices that belong to cell $C$.

with internal dissipation, however, depends on the values of parameters and can start to occur at relatively high values of $\omega$, revealing rich low-frequency behavior.

## 3.2 Application to the Vertex model with different types of dissipation

In this section, we apply this formalism to analyze the linear viscoelastic properties of the vertex model of epithelial tissues with both external (i.e., cell-substrate) and internal (i.e., cell-cell) dissipation. The results are compared against direct numerical simulations of the vertex model. In the vertex model, a confluent epithelial tissue is represented as a polygonal tiling of the plane. We also assume that the tiling is subject to periodic boundary conditions. Two cells share a junction, which is modeled as a straight line, and three or more cells meet at a vertex, which is the degree of

freedom in the model. The mechanical energy of the system is,

$$E = \sum_C \left[ \frac{K}{2} \left( A_C - A_0 \right)^2 + \frac{\Gamma}{2} \left( P_C - P_0 \right)^2 \right], \tag{3.22}$$

where $K$ and $\Gamma$ are the area and perimeter moduli, and $A_C$ and $P_C$ are the area and perimeter of cell $C$, respectively. $A_0$ and $P_0$ are, respectively, the preferred area and perimeters, here assumed to be the same for all cells. The dimensionless cell-shape parameter $p_0 = P_0/\sqrt{A_0}$ controls whether the model tissue is in the solid or the fluid regime. [23] Model tissues with low (high) values of the cell-shape parameters $p_0 < p_c$ ($p_0 > p_c$) behave like solids (fluids). The critical value of the cell-shape parameter $p_c$ that characterizes the solid-fluid transition is $p_c = \sqrt{8\sqrt{3}} \approx 3.722$ for regular hexagonal tilings, [89] while for disordered tilings the critical value falls in the range $p_c \approx 3.8 - 3.9$ [23, 51, 93] and depends on the procedure with which they are generated. Here, we consider both regular hexagonal and disordered tilings. Expressions for mechanical forces on each vertex $-\nabla_{\mathbf{r}} E$, the Hessian matrix $\hat{\boldsymbol{H}}$, and the driving force $\bar{\mathbf{f}}^{\mathrm{pb}}$ due to periodic boundaries that are used for the normal modes analysis are given in Appendices B.1, B.2, and B.3, respectively.

The dynamics of the vertex model has been studied almost exclusively with the assumption that the only source of dissipation is the interaction between the vertex and the substrate. [45] In real epithelial tissues, however, there are different sources of dissipation, many of which have not been well understood. We, therefore, studied three simple dissipation mechanisms, as shown in Fig. 3.2. These are encoded in the matrix $\hat{\boldsymbol{C}}$ and describe the dynamics of vertices [see Eq. (3.1)]. Specifically, Fig. 3.2a shows the friction $\mathbf{f}_i^{\mathrm{ed}} = -\gamma \mathbf{V}_i$ due to the relative velocity $\mathbf{V}_i$ between the vertex $i$ and the substrate. The superscript 'ed' is used to emphasize that this is a source of external dissipation. In this case, the dissipation matrix takes a simple diagonal form, $\hat{\boldsymbol{C}} = \gamma \hat{\boldsymbol{I}}$, where $\gamma$ is the friction coefficient and $\hat{\boldsymbol{I}}$ is the identity matrix. In

Fig. 3.2b, we consider the internal dissipation due to relative motions of neighboring vertices with friction coefficient $\zeta_V$. In this case, the dissipation force for the vertex $i$ can be expressed as $\mathbf{f}_i^{\text{id}} = -\zeta_V \sum_{j_\alpha \in S_i} (\mathbf{V}_i - \mathbf{V}_{j_\alpha})$, where the summation is over all nearest neighbor vertices, referred to as the "star" of vertex $i$ and denoted as $\mathcal{S}_i$. Assuming that each vertex is shared by three cell-cell junctions, $3\zeta_V$ appears on the diagonal of the $\hat{\boldsymbol{C}}$ matrix, and each row has three nonzero off-diagonal elements with the value $-\zeta_V$. Clearly, if there are vertices with coordination higher than three, this will be reflected in the diagonal term and the row of the matrix $\hat{\boldsymbol{C}}$ that correspond to such vertices. Another formulation of the internal dissipation is to consider the relative motions of neighboring geometric centers of cells, as shown in Fig. 3.2c. The velocity $\mathbf{V}_C$ of the geometric center of cell $C$ is defined as the average velocity of the $N_C$ vertices that belong to it, i.e., $\mathbf{V}_C = \frac{1}{N_C} \sum_{i \in C} \mathbf{V}_i$. The friction force that cell $C$ experiences due to the relative motions with respect to its neighboring cells is then defined as $\mathbf{f}_C^{\text{id}} = -\zeta_C \sum_{C_n \in \mathcal{N}_C} (\mathbf{V}_C - \mathbf{V}_{C_n})$, where $\zeta_C$ is the friction coefficient and the set $\mathcal{N}_C$ includes all neighboring cells of cell $C$. This friction force is assumed to be equally distributed across all the $N_C$ vertices that belong to cell $C$. Thus, the total friction force on the vertex $i$ is denoted as $\mathbf{f}_i^{\text{id}} = \sum_{C \in \mathcal{N}_i} \mathbf{f}_C^{\text{id}} / N_C$, where the set $\mathcal{N}_i$ includes all cells that share vertex $i$. Once the friction force at each vertex is known, the dissipation matrix $\hat{\boldsymbol{C}}$ can be written accordingly. Note that in this dissipation model, more than three vertices contribute to the force on a given vertex each contributing to an off-diagonal element of the matrix $\hat{\boldsymbol{C}}$. We also note that the models characterizing internal dissipation, such as the ones in Fig. 3.2b, c, play an important role if cells are not supported by the substrate, e.g., as is the case in early-stage embryos. Finally, we remark that in the absence of external dissipation the $\hat{\boldsymbol{C}}$ matrix is singular reflecting the fact that translations and rigid body rotations do not cause internal dissipation. Therefore, one should either consider small, but finite external friction, which is done in this study, or include inertia.

In the remainder of this section, we show how those three different types of dissipation affect the rheological properties of the vertex model for regular hexagonal and disordered tilings. For all three models, we compared the results of the normal mode analysis with direct numerical simulations of the vertex model.

### 3.2.1 Simulation setup

We start by briefly summarizing the setup of our vertex model simulations, with additional details provided in Ref. [52]. In most simulations of the vertex model [Eq. (3.22)], we fixed the values of $K$ and $A_0$, and measured the energy in units $KA_0^2$, stresses in units $KA_0$, and lengths in unit $A_0^{1/2}$. The preferred cell perimeter $P_0$, was varied to tune the system between solid or fluid phases. We fixed the perimeter modulus $\Gamma$ by fixing the ratio $KA_0/\Gamma \approx 3.464$ in most simulations since it does not affect the location of the solid to fluid transition. In Fig. 3.4 we, however, show an example of how the ratio $KA_0/\Gamma$ affects the dynamic shear modulus by changing the area modulus $K$.

We created regular hexagonal as well as disordered tilings subject to periodic boundary conditions as described in Ref. [52]. For regular hexagonal tilings, we used a nearly square domain with a total of 240 cells (15 cells in the horizontal direction). For disordered tiling, we used a square domain with 200 cells. Such systems are sufficiently large that the finite size effects are negligible as shown in Ref. [52]. All configurations used to probe the rheology corresponded to local energy minima obtained by the FIRE minimization algorithm. [94]

For the normal modes analysis, we first calculated the Hessian matrix $\hat{\boldsymbol{H}}$ using the expressions derived in Appendix B.2. Next, we used the NumPy library [124] in Python to numerical obtain the complete spectrum of eigenvalues, $\lambda_k$, and eigenvectors, $\boldsymbol{\xi}_k$, for the generalized eigenvalue problem in Eq. (3.5). This system of normal modes was then used to calculate the storage and loss shear moduli as explained in

Sections 3.1.2 and 3.1.3. These values of shear moduli were compared to the results of the simulations described below.

The shear rheology was probed by applying an oscillatory affine simple shear described by the deformation gradient $\hat{\boldsymbol{F}} = \left(\begin{smallmatrix} 1 & \epsilon(t) \\ 0 & 1 \end{smallmatrix}\right)$, where $\epsilon(t) = \epsilon_0 \sin(\omega_0 t)$ and we used a small magnitude of deformation, i.e., $\epsilon = 10^{-7}$. At each time step, we first applied the affine shear deformation to the simulation box and all vertices, which was followed by internal relaxation of vertices according to the overdamped dynamics [see Eq. (3.1)].

The response stress tensor, $\hat{\boldsymbol{\sigma}}_C(t) = \hat{\boldsymbol{\sigma}}_C^{\mathrm{e}}(t) + \hat{\boldsymbol{\sigma}}_C^{\mathrm{id}}(t)$, for each cell $C$ was computed following the formalism introduced in Refs. [104, 105, 106, 125] but took into account the contribution from internal dissipative forces (see Appendix B.4 for details). The stress due to elastic deformation is

$$\hat{\boldsymbol{\sigma}}_C^{\mathrm{e}} = -\Pi_C \hat{\boldsymbol{I}} + \frac{1}{2A_C} \sum_{e \in C} \mathbf{T}_e \otimes \mathbf{l}_e, \tag{3.23}$$

where the summation is over all junctions $e$ belonging to cell $C$. In the above Eq. (3.23), $\Pi_C = -\frac{\partial E}{\partial A_C} = -K(A_C - A_0)$ is the hydrostatic pressure inside cell $C$, $\hat{\boldsymbol{I}}$ is the unit tensor, and $\mathbf{T}_e = \frac{\partial E}{\partial \mathbf{l}_e} = 2\Gamma(P_C - P_0)\,\mathbf{l}_e/|\mathbf{l}_e|$ is the tension along the junction $e$ with $\mathbf{l}_e$ being a vector joining the two vertices on it. [104, 105, 106] The stress due to internal dissipation is

$$\hat{\boldsymbol{\sigma}}_C^{\mathrm{id}} = -\frac{1}{2z_i A_C} \sum_{i \in C} \left( \tilde{\mathbf{R}}_i \otimes \mathbf{f}_i^{\mathrm{id}} + \mathbf{f}_i^{\mathrm{id}} \otimes \tilde{\mathbf{R}}_i \right), \tag{3.24}$$

where the summation is over all vertices $i$ belonging to cell $C$. In Eq. (3.24), $\mathbf{f}_i^{\mathrm{id}}$ is the internal friction force applied at vertex $i$, and $\tilde{\mathbf{R}}_i = \mathbf{R}_i - \mathbf{R}_C$ is the position of vertex $i$ relative to the cell's geometric center $\mathbf{R}_C = \sum_{i \in C} \mathbf{R}_i / N_C$. The average stress tensor $\hat{\boldsymbol{\sigma}}(t) = \sum_C w_C \hat{\boldsymbol{\sigma}}_C(t)$, with $w_C = A_C / \sum_C A_C$, was used as a measure for the response of the system. We recorded the average shear stress signal $\hat{\sigma}_{xy}(t)$ once the

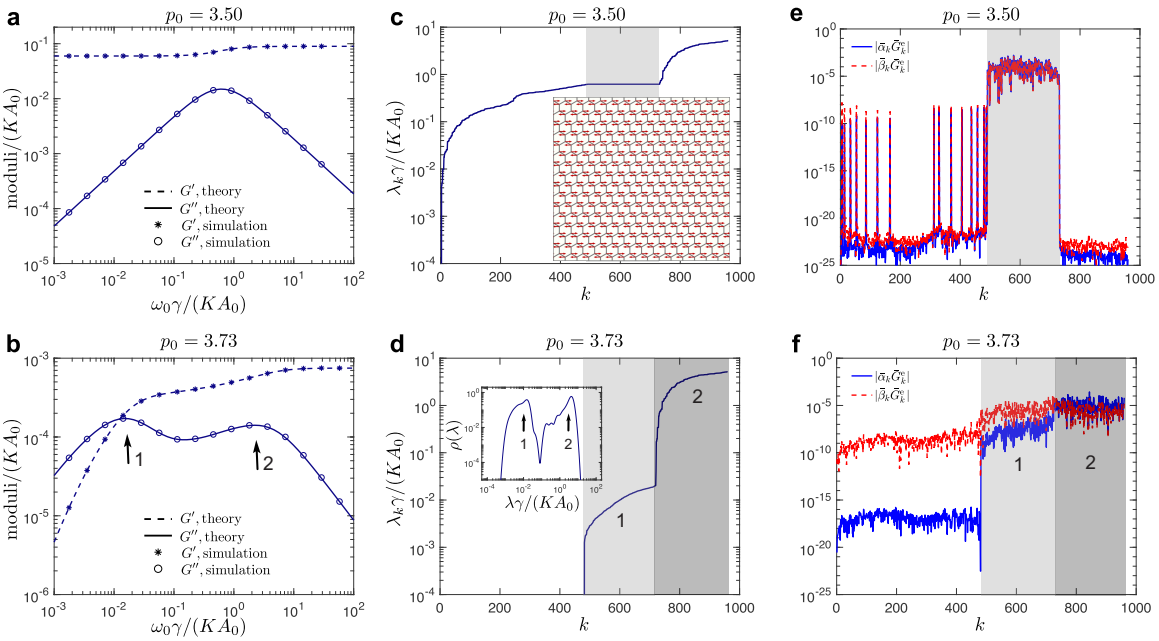


Figure 3.3: Shear rheology of hexagonal tilings with dissipation due to friction with the solid substrate. Results for two representative values of the cell shape parameter, $p_0 = 3.5$ in the solid phase (top row) and $p_0 = 3.73$ in the fluid phase (bottom row) are shown. (a,b) Storage and loss moduli from the simulations (symbols) compared with the predictions based on the normal mode analysis (lines). (c,d) Nonzero eigenvalues $\lambda_k$ vs. the mode number $k$; eigenvalues are sorted in the ascending order. (e,f) Absolute values of normalized coefficients $|\bar{\alpha}_k\bar{G}^e_k| = |\alpha_k G^e_k \gamma/(KA_0)^2|$ and $|\bar{\beta}_k\bar{G}^e_k| = |\beta_k G^e_k/(KA_0)|$ [see Eqs. (3.14) and (3.20)]. Also note that the ordinate covers $\sim 25$ decades. The inset in (c) shows a schematic of the normal mode $\boldsymbol{\xi}_D$ that dominates the shear rheology of hexagonal tilings in the solid phase. This dominant normal mode is a linear combination of degenerate normal modes within the shaded region in panel (c,e). Labeled arrows in panel (b) denote peaks that correspond to the characteristic timescales from the normal modes in the shaded regions in panels (d) and (f). The inset in (d) shows the density of states $\rho(\lambda)$.

system reached a steady state. The dynamics modulus $G^*(\omega_0) = \tilde{\hat{\sigma}}_{xy}(\omega_0)/\tilde{\epsilon}(\omega_0)$ was computed at a given driving frequency $\omega_0$ of the applied strain, where $\tilde{\hat{\sigma}}_{xy}(\omega)$ and $\tilde{\epsilon}(\omega)$ are the Fourier transforms of $\hat{\sigma}_{xy}(t)$ and $\epsilon(t)$, respectively.

### 3.2.2 Friction between vertices and a substrate

We first performed simulations of the vertex model with external dissipation only, i.e., the friction force $-\gamma\mathbf{V}_i$ applied to each vertex, as shown in Fig. 3.2a. Since the

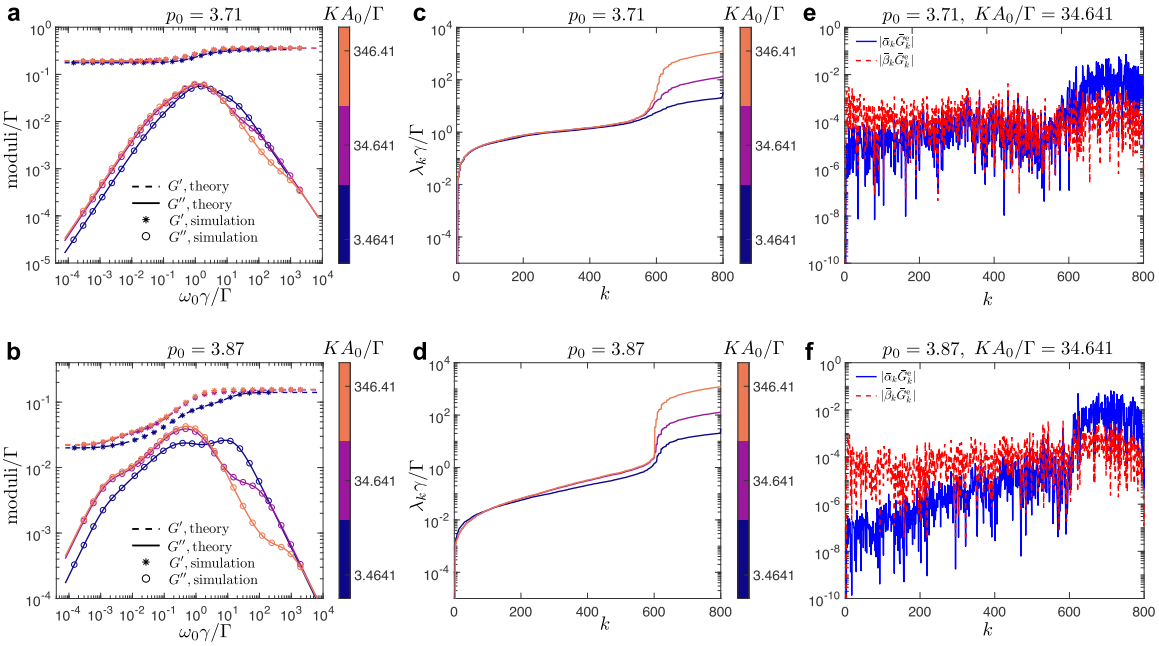


Figure 3.4: Shear rheology of disordered tilings with dissipation due to friction with the substrate for different values of the area elastic moduli $K$. Results for two representative values of the cell shape parameter, $p_0 = 3.71$ (top row) and $p_0 = 3.87$ (bottom row), are shown. (a,b) Storage and loss moduli from the simulations (symbols) compared with the predictions of the normal mode analysis (lines). Different colors represent the results from different values of the ratio $KA_0/\Gamma$. (c,d) Nonzero eigenvalues $\lambda_k$ in ascending order for different values of $KA_0/\Gamma$. (e,f) Absolute values of normalized coefficients $|\bar{\alpha}_k\bar{G}^e_k| = |\alpha_k G^e_k\gamma/(KA_0)^2|$ and $|\bar{\beta}_k\bar{G}^e_k| = |\beta_k G^e_k/(KA_0)|$ at one representative value of $KA_0/\Gamma = 34.641$.

external friction force produce stresses only indirectly (see Appendix B.4 for details), the values of $G^{\rm id}_{\rm pb}$ and $G^{\rm id}_k$ are 0 in Eq. (3.21). We validated the normal mode approach by comparing the shear moduli with the results of simple shear simulations of regular hexagonal tilings, which have been analyzed extensively in our previous work [52]. Fig. 3.3a,b show the storage and loss moduli obtained from simulations (dots) for representative values of $p_0$ in (a) the solid and (b) the fluid phase, which show excellent agreement with the predictions (lines) of the normal mode analysis. The corresponding eigenvalues $\lambda_k$ and the normalized coefficients $\bar{\alpha}_k\bar{G}^e_k = \alpha_k G^e_k\gamma/(KA_0)^2$ and $\bar{\beta}_k\bar{G}^e_k = \beta_k G_k/(KA_0)$ [see Eq. (3.14), Eq. (3.20) and Eq. (3.21)] for the normal mode analysis are shown in Figs. 3.3c,d and 3.3e,f, respectively.

We note that the distribution of eigenvalues $\lambda_k$ is often presented in the form of the density of states [120, 58, 59]. For the present analysis, however, in addition to the eigenvalues one also needs to know the values of coefficients $\bar{\alpha}_k \bar{G}^{\mathrm{e}}_k$ and $\bar{\beta}_k \bar{G}^{\mathrm{e}}_k$ that describe projections of external driving force to the normal modes. For this reason, it is more instructive to present $\lambda_k$, $\bar{\alpha}_k \bar{G}^{\mathrm{e}}_k$, and $\bar{\beta}_k \bar{G}^{\mathrm{e}}_k$ as functions of $k$. For reference, however, we show the density of states in the inset in Fig. 3.3d.

In our previous work [52], we noted that the rheological response of regular hexagonal tilings in the solid and fluid phases can be well described with the standard linear solid and Burgers model, respectively. This can be explained with the help of normal modes. The shear response in the solid phase is dominated by the set of normal modes in the shaded region in Fig. 3.3e, where coefficients $\bar{\alpha}_k \bar{G}^{\mathrm{e}}_k$ and $\bar{\beta}_k \bar{G}^{\mathrm{e}}_k$ have the highest values. All modes in this region correspond to the identical eigenvalue that we denote as $\lambda_D$ (see the shaded region in Fig. 3.3c). Hence, the shear response of hexagonal tilings in the solid phase is characterized by a single time scale $\lambda_D^{-1}$, and, therefore, can be accurately captured by the standard linear solid model. Note that the response of the system is dominated by the linear combination of normal modes that corresponds to the projection of the affine shear deformation to the set of these degenerate normal modes as $\boldsymbol{\xi}_D = \sum_{k \text{ s.t. } \lambda_k = \lambda_D} \left( \boldsymbol{\xi}_k^{\intercal} \, \mathbf{u}^{\mathrm{aff}} \right) \, \boldsymbol{\xi}_k$ of the same eigenvalue $\lambda_D$. The normal mode $\boldsymbol{\xi}_D$ is shown in the inset of Fig. 3.3b, where it is represented by the corresponding displacement field, which shows that the connected vertices move horizontally by the same amount but in opposite directions.

In the fluid phase (bottom row of Fig. 3.3), the spectrum of normal modes can be grouped in a region of zero-modes ($\lambda_k = 0$) and two distinct regions with approximately constant values of eigenvalues $\lambda_k$ (two shaded regions in Fig. 3.3d). These two regions of non-zero modes set the two characteristic timescales (marked by arrows in Fig. 3.3b) of the shear response of hexagonal tilings in the fluid phase, which can be

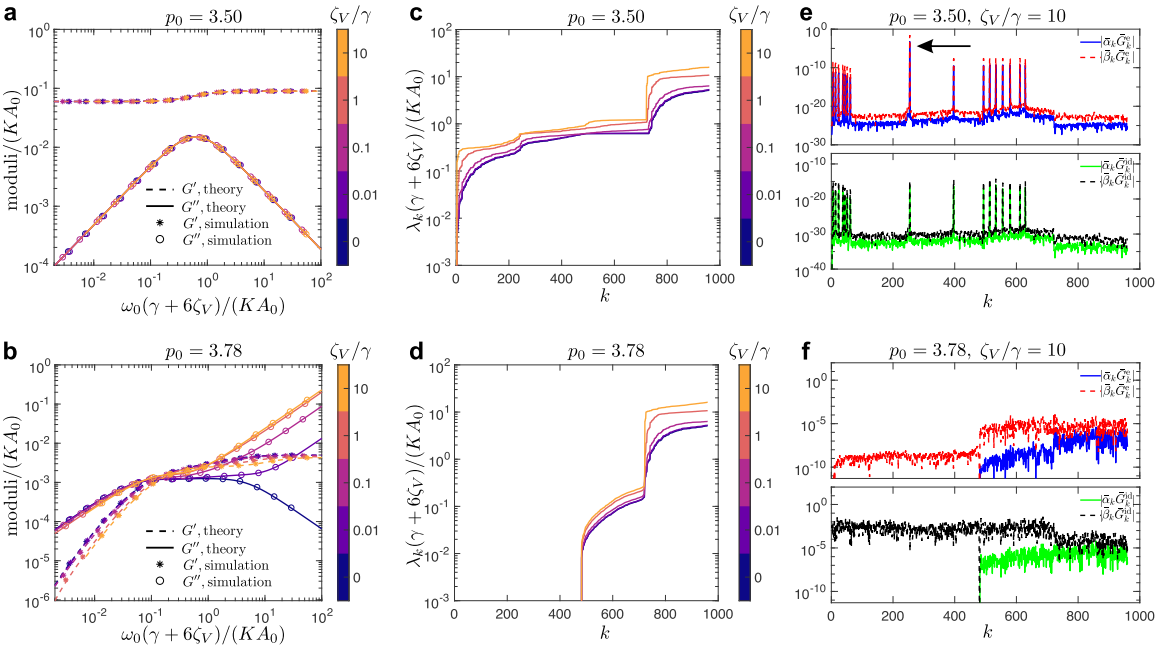


Figure 3.5: Shear rheology of hexagonal tilings with internal dissipation due to the relative motion of neighboring vertices in addition to the vertex-substrate friction. Results for two representative values of the cell shape parameter, $p_0 = 3.5$ in the solid phase (top row) and $p_0 = 3.78$ in the fluid phase (bottom row) are shown. (a,b) Storage and loss moduli from the simulations (symbols) compared with the predictions from normal modes (lines) for different values of the internal friction coefficient $\zeta_V$ (see colorbar). (c,d) Nonzero eigenvalues $\lambda_k$ in ascending order for different values of $\zeta_V$. (e,f) Normalized coefficients $\bar{\alpha}_k \bar{G}^{\rm e}_k = \alpha_k G^{\rm e}_k \gamma/(KA_0)^2$, $\bar{\beta}_k \bar{G}^{\rm e}_k = \beta_k G^{\rm e}_k/(KA_0)$, $\bar{\alpha}_k \bar{G}^{\rm id}_k = \alpha_k G^{\rm id}_k/(KA_0)$, and $\bar{\beta}_k \bar{G}^{\rm id}_k = \beta_k G^{\rm id}_k/\gamma$ [see Eqs. (3.14) and (3.20)] for a representative value of $\zeta_V/\gamma = 10$. In the solid phase, the rheological response is dominated by the single normal mode $\boldsymbol{\xi}_D$ marked by the arrow in panel (e), which corresponds to the highest value of coefficients $\bar{\alpha}_k \bar{G}^{\rm e}_k$ and $\bar{\beta}_k \bar{G}^{\rm e}_k$. Note very different values used for the ordinate axes in the top and bottom panels in (e).

described with the Burgers model. Note that the zero modes do not contribute to the shear response because the value of normalized coefficient $\bar{\alpha}_k \bar{G}^{\rm e}_k \approx 0$ (see Fig. 3.3f).

We used the normal mode approach to further demonstrate how the ratio between the area and perimeter moduli, $KA_0/\Gamma$, affects the shear rheology of the vertex model. We measured the storage and loss moduli of disordered tilings with different area modulus $K$ as shown in Fig. 3.4a,b for two representative values of $p_0$. The simulation results (symbols) show excellent agreement with the predictions of the normal mode analysis (lines). Note that in Fig. 3.4 we fixed $\Gamma$ and measured the stresses in units $\Gamma$

and time in units $\gamma/\Gamma$. We varied the values of $K$ by two orders of magnitude, as indicated by the colorbars for the ratio $KA_0/\Gamma$. Fig. 3.4c,d show the corresponding eigenvalues $\lambda_k$ in the ascending order. The eigenvalues $\lambda_k$ for $k > 600$ are strongly affected by the magnitude of the area modulus $K$. This indicates that the area term in the vertex model in Eq. (3.22) has a stronger contribution to the normal modes of large eigenvalues, which strongly affects the loss moduli at high frequency as a function of $K$ (see Fig. 3.4a,b). Fig. 3.4e,f shows the corresponding coefficients $\bar{\alpha}_k \bar{G}^{\mathrm{e}}_k$ and $\bar{\beta}_k \bar{G}^{\mathrm{e}}_k$ at a representative value of $KA_0/\Gamma = 34.641$. In our previous work [52], we noted that the standard linear solid and Burgers model cannot accurately capture the shear rheological properties for disordered tilings in the vicinity of the solid-fluid transition with $p_0 \approx 3.9$. This can be seen in Fig. 3.4b for $p_0 = 3.87$, where the complex rheological behavior is a consequence of the broad spectrum of normal mode eigenvalues $\lambda_k$ (see Fig. 3.4d). This reflects one of the key results of the normal mode approach that the full response of the vertex model is the sum of the contributions from all the normal modes, each of which behaves as a standard linear solid.

### 3.2.3 Friction due to the relative motion of neighboring vertices

In this section, we analyze the shear rheology of the vertex model with the internal friction due to the relative motion of connected vertices characterized by the friction coefficient $\zeta_V$ (see Fig. 3.2b). In addition, the system is subject to vertex-substrate friction with the friction coefficient $\gamma$, discussed in the previous section. In Fig. 3.5, we first report the results for hexagonal tilings at representative values of the cell shape parameter in the solid phase (top) and the fluid phase (bottom). Fig. 3.5a,b show an excellent agreement between the storage and loss moduli obtained from simulations (symbols) and the normal mode analysis (lines) for various values of the internal friction coefficient $\zeta_V$. Fig. 3.5e,f show the normalized coefficients $\bar{\alpha}_k \bar{G}^{\mathrm{e}}_k$ and

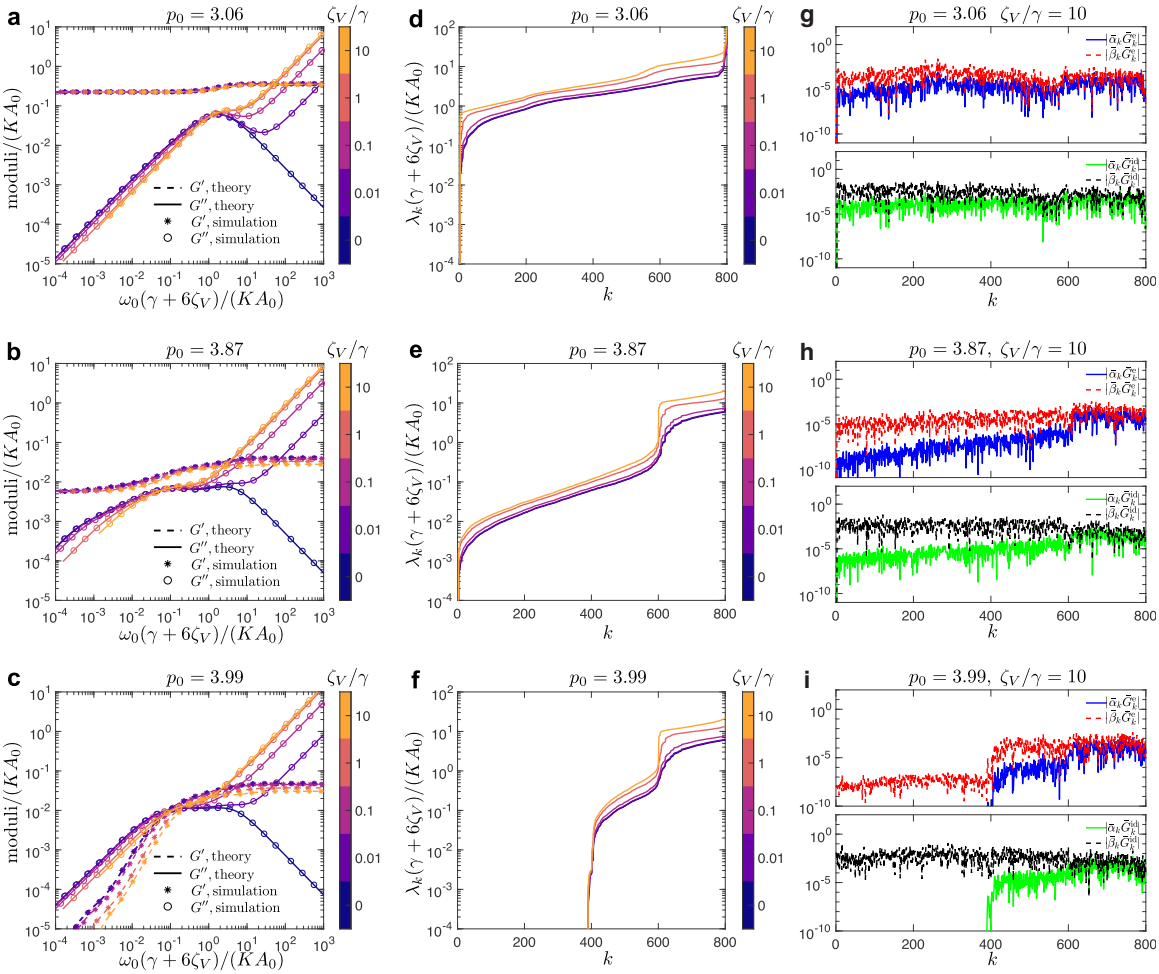


Figure 3.6: Shear rheology for disordered tilings with internal dissipation due to the relative motion of neighboring vertices in addition to cell-substrate friction. Results for three representative values of the cell shape parameter, $p_0 = 3.06$ deep in the solid phase (first row), $p_0 = 3.87$ close to the solid-fluid transition point on the solid side (second row), $p_0 = 3.99$ in the fluid phase (bottom row) are shown. (a,b,c) Storage and loss moduli from the simulations (symbols) compared with the predictions from normal modes (lines) for different values of the internal friction coefficient $\zeta_V$ (see colorbar). (d,e,f) Nonzero eigenvalues $\lambda_k$ in ascending order for different values of $\zeta_V$. (g,h,i) Normalized coefficients $\bar{\alpha}_k \bar{G}^{\rm e}_k = \alpha_k G^{\rm e}_k \gamma/(KA_0)^2$, $\bar{\beta}_k \bar{G}^{\rm e}_k = \beta_k G_k/(KA_0)$, $\bar{\alpha}_k \bar{G}^{\rm id}_k = \alpha_k G^{\rm id}_k/(KA_0)$, and $\bar{\beta}_k \bar{G}^{\rm id}_k = \beta_k G^{\rm id}_k/\gamma$ for a representative value of $\zeta_V/\gamma = 10$.

$\bar{\beta}_k \bar{G}^{\rm e}_k$ [see Eq. (3.14a), Eq. (3.20a) and Eq. (3.21a)] due to the contribution of elastic forces, $\bar{\alpha}_k \bar{G}^{\rm id}_k = \alpha_k G^{\rm id}_k/(KA_0)$ and $\bar{\beta}_k \bar{G}^{\rm id}_k = \beta_k G^{\rm id}_k/\gamma$ [see Eq. (3.14b), Eq. (3.20b) and Eq. (3.21b)] due to the contribution of internal dissipation.

The storage and loss moduli in the solid phase are characterized by a single timescale, and all curves for different values of $\zeta_V$ can be collapsed by rescaling the frequency as $\omega_0(\gamma+6\zeta_V)/(KA_0)$. This is because the shear response is dominated by the normal mode $\boldsymbol{\xi}_D$ introduced in the previous section, which is shown by the single peak of the normalized coefficients $\bar{\alpha}_k\bar{G}^{\mathrm{e}}_k$ and $\bar{\beta}_k\bar{G}^{\mathrm{e}}_k$ marked by the arrow in Fig. 3.5e. The normal mode $\boldsymbol{\xi}_D$ is simultaneously the eigenvector of the Hessian matrix $\hat{\boldsymbol{H}}$ and the dissipation matrix $\hat{\boldsymbol{C}}$. In particular, $\hat{\boldsymbol{C}}\boldsymbol{\xi}_D = (\gamma+6\zeta_V)\boldsymbol{\xi}_D$, since each vertex in the normal mode $\boldsymbol{\xi}_D$ moves in the opposite direction but with the same magnitude as the three vertices connected to it (see the schematic of $\boldsymbol{\xi}_D$ in the inset of Fig. 3.3c). The eigenvalue $\gamma+6\zeta_V$ with respect to $\hat{\boldsymbol{C}}$ thus accounts for the scaling factor of the frequency in Fig. 3.5a. Note that the values of normalized coefficients $\bar{\alpha}_k\bar{G}^{\mathrm{id}}_k$ and $\bar{\beta}_k\bar{G}^{\mathrm{id}}_k$ are negligible since the stresses from internal dissipation $\hat{\boldsymbol{\sigma}}^{\mathrm{id}}_C$ [see Eq. 3.24)] cancel out due to hexagonal symmetry. Hence, the rheological behavior in this case is analogous to the one for the hexagonal tiling in the solid phase with only external dissipation (compare Fig. 3.3a and Fig. 3.5a).

In the fluid phase, we rescaled the frequency with the same factor to help visually compare the change in the moduli with respect to the friction coefficient $\zeta_V$, as shown in Fig. 3.5b. Unlike in the solid phase, where the stress contributions $\hat{\boldsymbol{\sigma}}^{\mathrm{id}}_C$ from internal dissipative forces cancel out due to hexagonal symmetry, there is no such cancellation in the fluid phase and the loss modulus in the fluid phase increases as $G''(\omega)\sim\zeta_V\omega$ at high frequencies $\omega$ [see Eq. (3.21b)]. This is because the hexagonal state is unstable in the fluid regime and cells become slightly distorted in a local energy minimum [52]. Note that the crossover to the asymptotic regime $G''(\omega)\sim\zeta_V\omega$ shifts to lower frequencies as the ratio $\zeta_V/\gamma$ increases.

We proceed to perform simulations of the vertex model with disordered tilings, which mimic the geometry of real epithelial tissues. The first column in Fig. 3.6 shows the storage and loss moduli from simulations (symbols) for representative values of

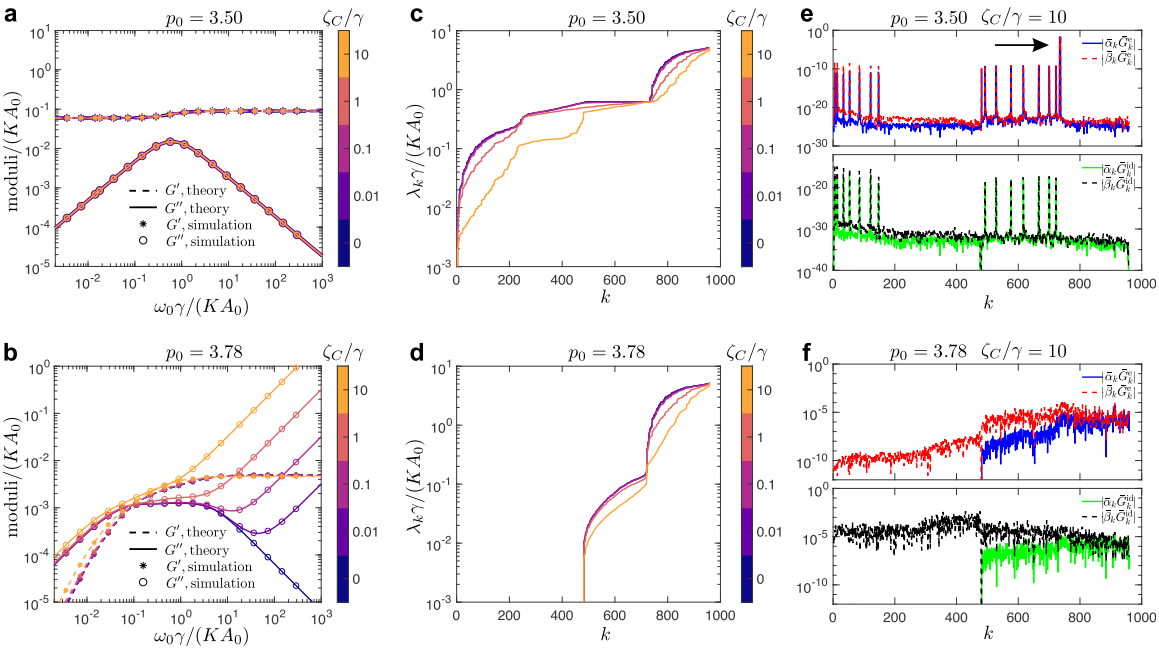


Figure 3.7: Shear rheology of hexagonal tilings with internal dissipation due to relative motion of neighboring cell centers and external cell-substrate friction. Results for two representative values of the cell shape parameter, $p_0 = 3.5$ in the solid phase (top row) and $p_0 = 3.78$ in the fluid phase (bottom row) are shown. (a,b) Storage and loss moduli from the simulations (symbols) compared with the predictions of the normal mode analysis (lines) for different values of $\zeta_C/\gamma$ (see colorbar). (c,d) Nonzero eigenvalues $\lambda_k$ in ascending order for different values of $\zeta_C/\gamma$. (e,f) Normalized coefficients $\bar{\alpha}_k\bar{G}^{\rm e}_k = \alpha_k G^{\rm e}_k\gamma/(KA_0)^2$, $\bar{\beta}_k\bar{G}^{\rm e}_k = \beta_k G_k/(KA_0)$, $\bar{\alpha}_k\bar{G}^{\rm id}_k = \alpha_k G^{\rm id}_k/(KA_0)$, and $\bar{\beta}_k\bar{G}^{\rm id}_k = \beta_k G^{\rm id}_k/\gamma$ for a representative value of $\zeta_C/\gamma = 10$. In the solid phase, the rheological response is dominated by the single normal mode $\boldsymbol{\xi}_D$ marked by the arrow in panel (e). This mode corresponds to the highest value of coefficients $\bar{\alpha}_k\bar{G}^{\rm e}_k$ and $\bar{\beta}_k\bar{G}^{\rm e}_k$. Note very different numerical values on ordinate axes in top and bottom panels in (e).

the cell shape parameter deep in the solid phase (top row, $p_0 = 3.06$), close to the solid-fluid transition point on the solid side (middle row, $p_0 = 3.87$), and in the fluid phase (bottom row, $p_0 = 3.99$), which show excellent agreement with predictions of the normal mode analysis (lines). As usual, the frequency is again measured in units of $KA_0/(\gamma + 6\zeta_V)$. When the system is deep in the solid phase, as shown in Fig. 3.6a, the response is similar to that of a standard linear solid, with loss modulus having one peak for small values of $\zeta_V/\gamma$ in the low-frequency regime, and crossing over to the asymptotic behavior $G''(\omega) \sim \zeta_V\omega$ in the high-frequency regime, where

the internal dissipation dominates. Increasing the ratio $\zeta_V/\gamma$ moves this crossover to lower frequencies, which is analogous to the behavior of hexagonal tilings in the fluid phase (see Fig. 3.5b).

When the system is close to the solid-fluid transition, but on the solid side (see Fig. 3.6b), the loss modulus develops two peaks, whose separation becomes more pronounced as $\zeta_V/\gamma$ increases. This is similar to the behavior for hexagonal tilings shown in Fig. 3.5b, which can be accounted for by the jump between the two regions of eigenvalues $\lambda_k$ becoming sharper with increasing $\zeta_V/\gamma$, as shown in Figs. 3.5d and 3.6e. The internal dissipation, however, dominates in the high-frequency regime, and the loss modulus crosses over to increasing with frequency, which is again shifted to the left as $\zeta_V/\gamma$ increases. Furthermore, the loss modulus crosses over from the linear scaling ($\sim \omega$) at low frequencies to anomalous scaling ($\sim \omega^\alpha$) with the fractional exponent $\alpha < 1$ at intermediate frequencies (see Fig. 3.6b), which was already noted in our prior work in Ref. [52]. This is because the eigenvalues $\lambda_k$ gradually increase by two orders of magnitude up to the sharp jump point in Fig. 3.6e.

In the fluid phase, the internal dissipation $\zeta_V$ has a similar effect on the loss modulus as shown in Fig. 3.6c and one observes that the loss modulus crosses over to growing linearly with frequency in the high-frequency regime.

### 3.2.4 Friction due to relative motions of neighboring cells

Finally, we investigated the shear rheology of the vertex model with the internal friction due to the relative motion of neighboring cell centers characterized by the friction coefficient $\zeta_C$ (see Fig. 3.2c). As in the previous section, vertices also experience friction with the substrate with the friction coefficient $\gamma$. In Fig. 3.7, we show the dynamic moduli for hexagonal tilings at representative values of the cell shape parameter in the solid (top) and the fluid phase (bottom). In the solid phase, the dominant normal mode $\boldsymbol{\xi}_D$ does not generate friction due to relative motion of neigh-

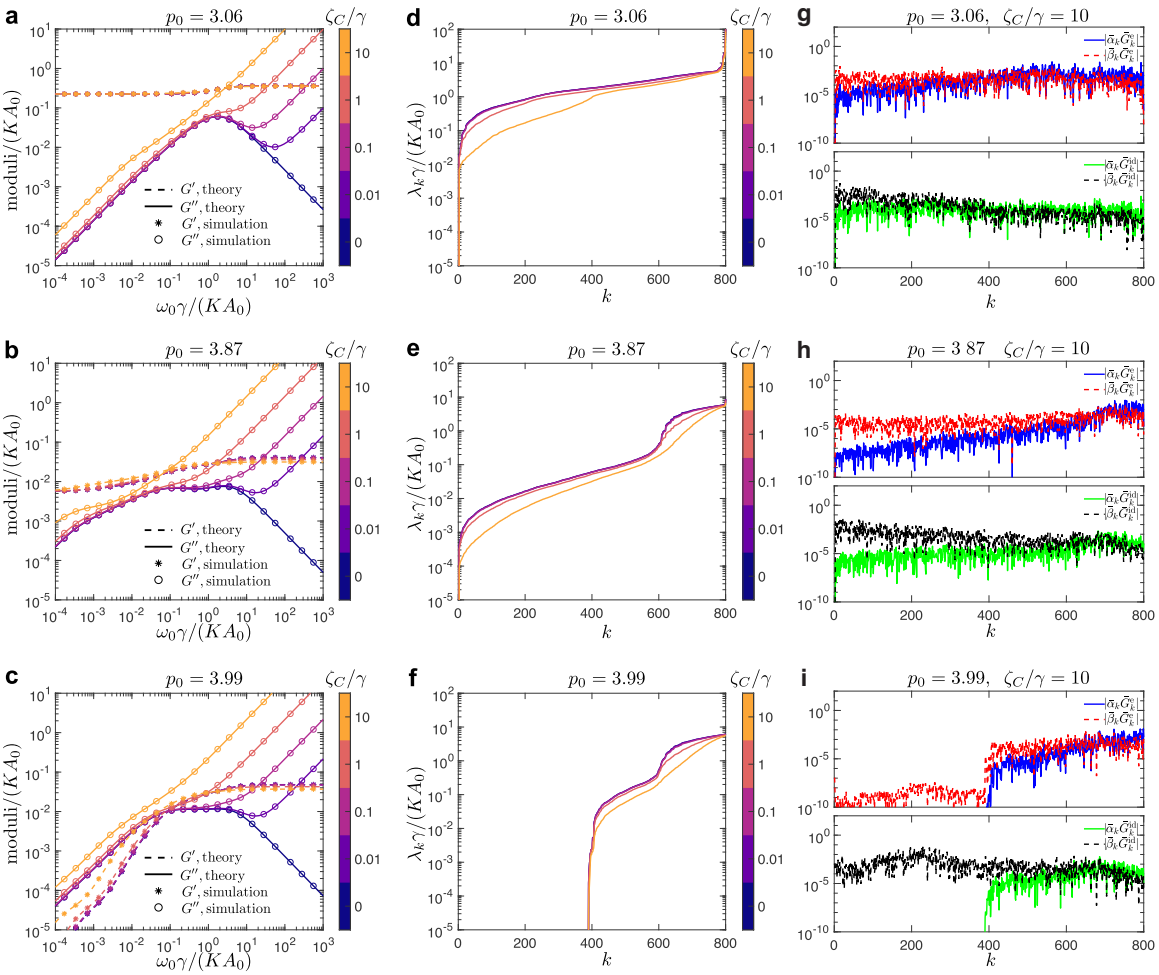


Figure 3.8: Shear rheology for disordered tilings with internal dissipation due to the relative motion of neighboring cell centers and external cell-substrate friction. Results are shown for three representative values of the cell shape parameter, $p_0 = 3.06$ deep in the solid phase (top row), $p_0 = 3.87$ close to the solid-fluid transition point on the solid side (middle row), and $p_0 = 3.99$ in the fluid phase (bottom row). (a,b,c) Storage and loss moduli from the simulations (symbols) compared with the predictions of the normal mode analysis (lines) for different values of $\zeta_C/\gamma$ (see colorbar). (d,e,f) Nonzero eigenvalues $\lambda_k$ in ascending order for different values of $\zeta_C/\gamma$. (g,h,i) Normalized coefficients $\bar{\alpha}_k\bar{G}^{\rm e}_k = \alpha_k G^{\rm e}_k\gamma/(KA_0)^2$, $\bar{\beta}_k\bar{G}^{\rm e}_k = \beta_k G_K/(KA_0)$, $\bar{\alpha}_k\bar{G}^{\rm id}_k = \alpha_k G^{\rm id}_k/(KA_0)$, and $\bar{\beta}_k\bar{G}^{\rm id}_k = \beta_k G^{\rm id}_k/\gamma$ at one representative value of $\zeta_C/\gamma = 10$.

boring cells, i.e., $\hat{\boldsymbol{C}}\boldsymbol{\xi}_D = \gamma\boldsymbol{\xi}_D$. Thus, the shear rheology for the hexagonal tiling in the solid phase is identical to that of the model with the cell-substrate friction only, cf. Fig. 3.3.

In the fluid phase, the two small humps in the loss modulus that are present in the case with only the vertex-substrate dissipation (i.e., for $\zeta_C = 0$) are smoothed out as $\zeta_C/\gamma$ increases (see Fig. 3.7b). This is because the jump between two regions of eigenvalues $\lambda_k$ are smoothed out with increasing $\zeta_C/\gamma$, as shown in Fig. 3.7d. Note that this is different from the the case with dissipation due to the relative motion of neighboring vertices, where the jump in the spectrum of eigenvalues $\lambda_k$ becomes more pronounced as the value of $\zeta_V/\gamma$ increases (see Fig. 3.5d)

In Fig. 3.8, we report the results for disordered tilings. The first column in Fig. 3.8 shows the storage and loss moduli from simulations (symbols) for representative values of the cell shape parameter deep in the solid phase (top row, $p_0 = 3.06$), close to the solid-fluid transition point on the solid side (middle row, $p_0 = 3.87$), and in the fluid phase (bottom row, $p_0 = 3.99$), which all show excellent match with predictions from the normal modes (lines). For a system deep in the solid phase, the loss modulus develops a secondary shoulder at low frequencies as $\zeta_C$ increases (see Fig. 3.8a), which corresponds to the jump of the eigenvalues $\lambda_k$ developing at $k \approx 400$ in Fig. 3.8d.

When the system is close to the solid-fluid transition on the solid side, the range of intermediate frequencies over which the loss modulus has a significant value becomes wider with a small bump developing at low frequency as $\zeta_C/\gamma$ increases (see Fig. 3.8b). This is reflected by a wider range of eigenvalues $\lambda_k$ with increasing $\zeta_C/\gamma$ in Fig. 3.8e. This behavior is different from the response of the system with friction due to the relative motion of neighboring vertices, for which the dynamic range of characteristic time scales does not significantly change with $\zeta_V$ (see Fig. 3.6e).

In the fluid phase, similarly to the hexagonal tilings, the two small bumps in the loss modulus at intermediate frequencies, when there is only external dissipation (i.e.,

for $\zeta_C = 0$), are smoothed out as $\zeta_C/\gamma$ increases (see Fig. 3.8c), which is reflected by the jump of eigenvalues $\lambda_k$ at $k \approx 600$ being smoothed out with increasing $\zeta_C$ as shown in Fig. 3.8f.

## 3.3 Conclusion and discussion

In this chapter, we used the normal modes formalism to develop a general method for calculating dynamic rheological moduli of soft materials in the linear response regime in the presence of internal and external dissipation. A key finding is that the dynamic rheological moduli can be represented as a linear superposition of standard linear solid and Jeffreys elements connected in parallel, with each mode contributing a characteristic relaxation timescale related to its eigenvalue. The external and internal dissipation, i.e., friction with the substrate and friction between constitutive elements of the system, respectively, have markedly different effects on the rheology. The external dissipation together with elastic relaxation combine to result in the standard linear solid model, i.e., a viscoelastic solid. On the other hand, the internal dissipation is described by the Jeffreys element, and it represents a viscoelastic liquid. As the result, the behavior of the loss modulus is qualitatively different at high frequencies depending on whether the internal dissipation is present or not. While the calculated dynamical moduli depend on the precise details of microscopic dynamics and dissipation mechanism, the method presented here based on normal modes is agnostic to such details. It can be applied to systems with any number of spatial dimensions as long as it is possible to define an energy function with well-defined local minima that is differentiable twice. Although here we considered the overdamped case, extension to systems with inertia is straightforward.

Finally, for systems with less than $\sim 10^4$ degrees of freedom, this method is superior in terms of computational cost compared to direct simulations since one

needs to solve the generalized eigenvalue problem only once, which can then be used to determine the linear response properties over the full range of frequencies. For larger systems sizes, however, solving the full eigensystem becomes computationally costly since the computational complexity scales as $O\big((dN)^3\big)$, where $dN$ is the total number of degrees of freedom. If one is interested only in the low-(high-)frequency response, this can be somewhat alleviated by computing only a small subset of normal modes with the lowest (highest) eigenvalues, which can be done at a lower computational cost $O(N^2)$. In the case where the full-frequency scan is required, however, for large systems, the direct simulations become computationally advantageous. The associated complexity of a single direct simulation with short-range interaction scales as $O(dN \times n_t)$, but typically with a substantial prefactor. Here $n_t = t_{\mathrm{tot}}/\Delta t = 2\pi n_{\mathrm{periods}}/(\omega \Delta t)$ corresponds to the total number of timesteps, which is especially high for low driving frequencies $\omega$. This, combined with the need to repeat the full simulation for each driving frequency, makes direct simulations far less appealing.

We applied this formalism to study the linear response to shear deformations of the two-dimensional vertex model for epithelial tissue mechanics with three different microscopic mechanisms of dissipation. We derived expressions for mechanical stresses on cells due to elastic and dissipative forces and showed that for all three dissipation models, the method gives an excellent agreement with direct numerical simulations. Although our analysis of the vertex model is limited to the linear response regime and is unable to capture the response to large deformations, especially if those involve local plastic rearrangements, it nonetheless provides valuable insights into its complex rheology. In particular, it allows one to fully understand the behavior of the storage and loss moduli of the vertex model in the linear response regime in terms of the behaviors of each normal mode. Applying this approach to compute and understand other response functions, e.g., the bulk modulus is also straightforward, as is the

treatment of different forms of external driving. For example, modeling a typical experimental setup where the system is clamped at two of its ends that are then moved relative to each other would just involve introducing the appropriate functional form for the driving force in Eq. (3.3). Additionally, the generalized eigenvalue problem in Eq. (3.5) would have to be solved subject to appropriate boundary conditions.

The ability to study the effects of both internal and external dissipation at the same footing makes this approach appealing to studying the effects of complex dissipative processes. In addition, the method can be directly extended to models that include the effects of activity. [126, 127, 128, 129, 130] Understanding the roles of activity and internal dissipation is crucial for a proper understanding of the rheology of living tissues.

# Chapter 4

# Mechanical response of wrinkled structures

In this chapter, we present a theoretical study of how wrinkled structures respond to infinitesimal surface forces in either vertical or horizontal directions. We find that the linear response diverges near the onset of the wrinkling instability and then decays away from this critical compression threshold. The mechanical response near the critical compression threshold can be understood exclusively in terms of the dominant characteristic Fourier mode of wrinkles, which is decoupled from other modes. However, away from the critical compression threshold, the coupling between different Fourier modes becomes significant and it affects the mechanical response.

The structure of this chapter is summarized as follows. In section 4.1, we first focus on a special case where a vertical point force is applied at the peak of the wrinkles. We make an analogy to the critical phenomena in the Landau phase transition model to understand the linear response behavior of wrinkled structures. We show that the linear response diverges near the onset of wrinkling instability due to the divergence of the Fourier mode that corresponds to the characteristic Fourier mode of wrinkles. In section 4.2, we give the general formalism of the wrinkling problem in the presence

of external forces. We derive the nonlinear governing equations in Fourier space. The governing equations are solved perturbatively in section 4.3 and 4.4. In section 4.3, we assume the amplitude of wrinkles is small enough when the compression is near the instability threshold. Based on this assumption, we recover the simple Landau-like response theory discussed in section 4.1. We illustrate the response due to vertical or horizontal forces in section 4.3.1 and 4.3.2. The vertical point force is placed at the peak of the wrinkles, whereas a pair of horizontal forces are applied symmetrically to the peak or the valley of the wrinkles. In section 4.3.4, we discuss the rearrangement of wrinkle profiles due to asymmetric external forces. In section 4.4, we show that coupling between different Fourier modes becomes significant when the compression is moderately above the critical threshold, which can be captured by linearized matrix equations.

## 4.1 Landau theory

We consider the bilayer structure with a thin stiff film bound to a soft substrate. The schematic of the geometry and notations for the problem are shown in Fig. 1.2(b,c). For simplicity, we assume the film is pre-compressed by a uni-axial strain $\eta_x > 0$, the direction of which is along the x-axis. Then we can treat our problem as a 2D problem. The out-of-plane direction is along the y-axis. The deformed configuration of the film is described by the displacements of the central surface of the film. The displacement field is denoted as $(u(x), w(x))$, where $u(x)$ is the in-plane displacement and $w(x)$ is the out-of-plane displacement. We also denote $h$, $E_f$, and $\nu_f$ as the thickness, Young's modulus, and Poisson's ratio of the film, respectively. The in-plane strain in the film is defined as

$$\epsilon_{xx} = -\eta_x + \frac{du}{dx} + \frac{1}{2}\left(\frac{dw}{dx}\right)^2. \tag{4.1}$$

The film is described by the Föppl-von Kármán plate theory [131], in which the elastic energy of the film has two parts. One is the bending energy $\mathcal{U}_{\text{fb}}$, the other is the stretching energy $\mathcal{U}_{\text{fs}}$. They take the following form:

$$\mathcal{U}_{\text{fb}} = \frac{1}{L}\frac{B}{2}\int \left(\frac{d^2w}{dx^2}\right)^2 dx, \tag{4.2}$$

$$\mathcal{U}_{\text{fs}} = \frac{1}{L}\frac{E_0}{2}\int \epsilon_{xx}^2 \, dx, \tag{4.3}$$

where $B = \frac{E_f h^3}{12(1-\nu_f^2)}$ is the bending rigidity, $E_0 = \frac{E_f h}{1-\nu_f^2}$ is the reduced 2D Young's Modulus, $L$ is the length of the structure along x direction.

We treat the substrate as a 2D semi-infinite linear elastic medium. $E_s$, $\nu_s$ are used to denote Young's modulus and Poisson's ratio of the substrate. Based on linear elasticity, the energy of the substrate is written as the sum of the contributions from each Fourier mode [72],

$$\mathcal{U}_{\text{substrate}} = \frac{1}{2}K_1 \sum_k |k|\tilde{w}(k)\tilde{w}(-k), \tag{4.4}$$

where $K_1 = \frac{2E_s(1-\nu_s)}{(1+\nu_s)(3-4\nu_s)}$. In this work, we use the definition of the Fourier Transform of a function $w(x)$ as follows,

$$\tilde{w}(k) = \frac{1}{L}\int w(x)e^{-ikx}dx. \tag{4.5}$$

The corresponding Fourier series of $w(x)$ is then written as

$$w(x) = \sum_k \tilde{w}(k)e^{ikx}. \tag{4.6}$$

In the presence of external forces, the total energy density of the system is written as

$$\mathcal{U}_{\text{total}} = \mathcal{U}_{\text{fb}} + \mathcal{U}_{\text{fs}} + \mathcal{U}_{\text{s}} - \frac{1}{L}\int dx f_y(x)w(x), \tag{4.7}$$

where $f_y(x)$ is the external force density along $y$ direction. This section focuses on the response to a vertical point force. Specifically, the point force is located at the peak of wrinkles. In the later sections, we will return to the general formalism of response theory. Under the assumption that the external forces are tiny, we study the linear response behavior of wrinkled structures. We will transform this energy functional Eq. (4.7) into a Landau-like model and make an analogy to the second-order phase transition.

Without loss of generality, we align the y-axis with the peak where the force is located so that $f_y(x) = F_0\delta(x)$ where $\delta(x)$ is the Dirac function and the corresponding Fourier component of $f_y(x)$ is $\tilde{f}_y(k) = F_0/L$. Due to the mirror symmetry of the problem, the response should be an even function. Thus, We consider the following perturbation expansion of the out-of-plane displacement

$$w(x) = A_0\cos(k_0x) + \sum_{k>0}\delta\tilde{w}(k)\cos(kx), \tag{4.8}$$

where $A_0\cos(k_0x)$ is the ground state of wrinkled structures in the absence of external forces, $k_0$ denotes the characteristic Fourier mode of wrinkled structures, $\sum_{k>0}\delta\tilde{w}(k)\cos(kx)$ is the additional displacement due to the presence of the external force. The equilibrium state of the system is the one that minimizes the total energy. The minimization of the total energy with respect to the in-plane displacement, i.e., $\frac{\delta\mathcal{U}_{\text{total}}}{\delta u(x)}$, leads to $\frac{d}{dx}\epsilon_{xx}(x) = 0$, which concludes that $\epsilon_{xx}(x)$ is a constant function. One then can perform the integration of each Fourier mode separately to obtain in-plane displacement as a function of out-of-plane displacement. The in-plane strain turns out to be $\epsilon_{xx} = -\eta_x + \frac{1}{4}A^2k_0^2 + \sum_{k\neq k_0}\frac{1}{4}\delta\tilde{w}^2(k)k^2$, where we combine the amplitude of wrinkles $A_0$ and response amplitude $\delta\tilde{w}(k_0)$ for the characteristic Fourier mode $k_0$ as $A = A_0 + \delta\tilde{w}(k_0)$. The total energy in terms of the sum of the contributions from

each Fourier mode of out-of-plane displacement is as follows,

$$\mathcal{U}_{\text{total}} = \sum_{k\neq k_0, k>0} \frac{1}{4}Bk^4\delta\tilde{w}^2(k) + \frac{1}{4}\left(-\eta_x + \frac{1}{4}A_0^2k_0^2\right)E_0k^2\delta\tilde{w}^2(k) + \frac{1}{4}K_1k\delta\tilde{w}^2(k) - \frac{F_0}{L}\delta\tilde{w}(k) + \frac{1}{4}Bk_0^4A^2 - \frac{1}{4}E_0k_0^2\eta_xA^2 + \frac{1}{4}K_1k_0A^2 + \frac{1}{32}E_0k_0^4A^4 - \frac{F_0}{L}A, \tag{4.9}$$

where we keep the response of each Fourier mode up to quadratic order.

In the absence of external force, i.e., $F_0 = 0$, we only need to keep the characteristic mode $k_0$ in the energy functional of Eq. (4.9), which is

$$\mathcal{U}_{k_0} = \frac{1}{4}Bk_0^4A^2 - \frac{1}{4}E_0k_0^2\eta_xA^2 + \frac{1}{4}K_1k_0A^2 + \frac{1}{32}E_0k_0^4A^4. \tag{4.10}$$

Eq. (4.10) with $A$ regarded as the order parameter, is similar to the Landau phase transition model [132], which describes the critical phenomena in ferromagnets. Analogously, the Landau model can describe the transition between the smooth and wrinkled states of bilayer structures. The critical point is obtained by setting the coefficient of $A^2$ to be 0, which corresponds to the transition of a single well potential to a double-well potential, as shown schematically in Fig. 4.1(a). As a result, we obtained the critical compression of wrinkling instability,

$$\eta_{x,cr} = \frac{1}{E_0}(Bk_0^2 + K_1/k_0). \tag{4.11}$$

The characteristic Fourier mode $k_0$ is obtained by minimizing Eq. (4.11) of $\eta_{x,cr}$ with respect to $k_0$, since $k_0$ is the first unstable mode when the instability occurs. We then have the characteristic Fourier mode $k_0$ of wrinkles

$$k_0 = \left(\frac{K_1}{2B}\right)^{1/3} \tag{4.12}$$

We can rewrite Eq. (4.10) in the absence of external forces as

$$\mathcal{U}_{k_0} = \frac{1}{4} E_0 k_0^2 (\eta_{x,cr} - \eta_x) A^2 + \frac{1}{32} E_0 k_0^4 A^4. \tag{4.13}$$

The schematic of the energy functional of Eq. (4.13) is shown in Fig. 4.1(a). It is clear that the phase transition occurs at $\eta_x = \eta_{x,cr}$. When $\eta_x > \eta_{x,cr}$, we can obtain the minimum of the double well potential in the absence of external force as

$$A_0 = \pm \sqrt{\frac{4(\eta_x - \eta_{x,cr})}{k_0^2}} \quad (\eta_x > \eta_{x,cr}), \tag{4.14}$$

which corresponds to the amplitude of wrinkles. The theoretical prediction of the amplitude of wrinkles as a function of compression [see Eq. (4.14)] is shown in Fig. 4.1(b), which agrees with the Finite Element simulation results.

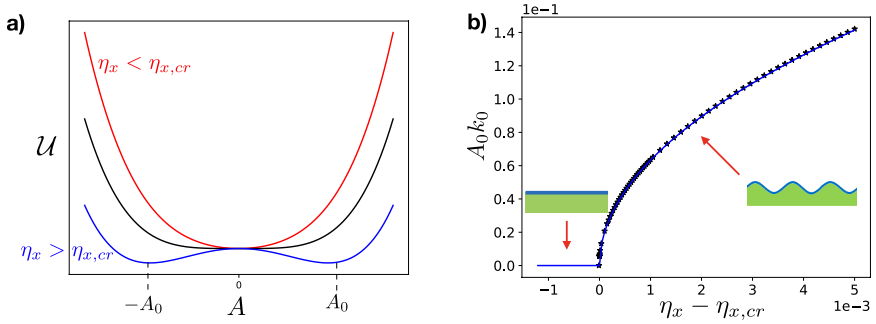


Figure 4.1: (a) A schematic of the energy in the absence of external forces as a function of the amplitude $A$. When $\eta_x < \eta_{x,cr}$, the minimum of the energy is at $A = 0$, which corresponds to the smooth state. When $\eta_x > \eta_{x,cr}$, two minima $\pm A_0$ correspond to the wrinkled state. (b) The evolution of the amplitude of wrinkles $A_0$ as a function of compression $\eta_x$. Black dots are the FEM simulation results, for which $E_f/E_s = 10^4$ and $\eta_{x,cr} = 0.0012$.

In the presence of the vertical point force, we consider the linear response from Eq. (4.9). To simplify notation, we use $q = k/k_0$ as the normalized wavenumber for different Fourier modes. So $q = 1$ represents the characteristic mode $k_0$. Before

wrinkling, the linear response expressions for different Fourier modes are

$$\delta\tilde{w}(k_0) = 2(\frac{4B^2}{E_0^3K_1^2})^{\frac{1}{3}}\frac{F_0/L}{\eta_{x,cr}-\eta_x}, \tag{4.15a}$$

$$\delta\tilde{w}(qk_0) = (\frac{2B}{K_1^4})^{\frac{1}{3}}\frac{4F_0/L}{q(2-3\frac{\eta_x}{\eta_{x,cr}}q+q^3)}, \tag{4.15b}$$

while after wrinkling

$$\delta\tilde{w}(k_0) = (\frac{4B^2}{E_0^3K_1^2})^{\frac{1}{3}}\frac{F_0/L}{\eta_x-\eta_{x,cr}}, \tag{4.16a}$$

$$\delta\tilde{w}(qk_0) = (\frac{2B}{K_1^4})^{\frac{1}{3}}\frac{4F_0/L}{q(2-3q+q^3)} \quad q\neq 1. \tag{4.16b}$$

To verify our theory, we compare the theoretical predictions of Eq. (4.15,4.16) with results from Finite Element Method (FEM) simulations. The details about how we carry out the FEM simulations are explained in Appendix C.2. Fig. 4.2 present the theoretical predictions compared to the simulation results. Fig. 4.2(a) shows how the additional displacement due to a tiny vertical point force evolves as a function of the compression $\eta_x$. The displacement is measured at the location where the point force is applied. As seen from Fig. 4.2(a), wrinkled structures have a divergent linear response near the critical threshold. This is because the linear response of the characteristic mode $k_0$ diverges at $\eta_{x,cr}$ [see Eq. (4.15a,4.16a)]. Combining contributions of all the Fourier modes from theory [see Eq. (4.15,4.16)], we can give the theoretical prediction of the displacement in real space. The black dashed curve in Fig. 4.2(a) gives the theoretical prediction of the displacement at the location where the force is applied. The deviation from simulation results at compression $\eta_x$ much larger than $\eta_{x,cr}$ is due to the coupling of different modes, which we will discuss in details in section 4.4. Fig. 4.2(b,c) are the comparison of the response theory of different Fourier modes from Eq. (4.15,4.16) and FEM results with different values for the ratio of elastic constants $E_f/E_s$. Based on Eq. (4.16), we choose the appropriate normalized factor

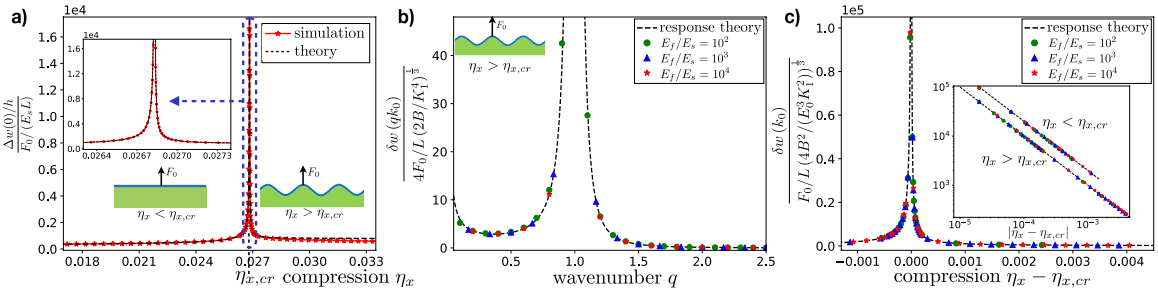


Figure 4.2: (a) Additional displacement due to a vertical point force as a function of the compression $\eta_x$. (b,c) Comparison of the response theory [Eq. (4.15,4.16)] with FEM simulation results. Discrete points are from the simulations, while the dashed curves are predictions from the theory. (b) Normalized response as a function of normalized wavenumber $q = k/k_0$ for different values of elastic ratio $E_f/E_s$ at a given loading parameter $\eta_x$. we choose $\eta_x$ such that $\eta_x - \eta_{x,cr} \approx 2\times10^{-5}$. $\eta_{x,cr}$ is different for different $E_f/E_s$. (c) The response of normalized characteristic mode $k_0$ as a function of $\eta_x - \eta_{x,cr}$ for different values of elastic ratio $E_f/E_s$. The same figure is plotted in the log-log scale in the inset figure, which confirms the divergent behavior of the characteristic mode predicted from the theory.

for the response modes $\delta\tilde{w}(qk_0)$ in Fig. 4.2(b,c), which shows that simulation results for different values of elastic ratios $E_f/E_s$ collapse onto one single curve predicted from the theory. According to Eq. (4.15a,4.16a), linear response of the characteristic mode diverges at critical threshold $\eta_{x,cr}$ with the same scaling exponent before and after wrinkling. The scaling behavior is shown in the inset of Fig. 4.2(c). According to Eq. (4.16b), linear response of other Fourier modes diverges as $q$ approaches 1, which is shown in Fig. 4.2(b). This observation is consistent with the divergence of the characteristic Fourier mode $k_0$.

The analogy between the phase transition of ferromagnets and wrinkling instability is summarized in table 4.1. In the absence of an external field, the phase transition of ferromagnetism or wrinkling instability occurs as a supercritical pitchfork bifurcation. The stable solution of the order parameter, either the magnetization $M$ or the amplitude of wrinkles $A$, can be described by Fig. 4.1(b) (the other branch of stable solution with an opposite sign is not plotted). When an external field is

| Ferromagnets | Wrinkled structures |
|---|---|
| temperature $T$ | compressive strain $\eta_x$ |
| critical temperature $T_c$ | critical compression $\eta_{x,cr}$ |
| magnetisation $M \propto \sqrt{T - T_c}$ | amplitude $A \propto \sqrt{\eta_x - \eta_{x,cr}}$ |
| external magnetic field $H$ | external vertical point force $F_0$ |
| susceptibility $\chi = \frac{M}{H} \propto \frac{1}{T-T_c}$ | linear response of characteristic mode $\frac{\delta\tilde{w}(k_0)}{F_0} \propto \frac{1}{\eta_x - \eta_{x,cr}}$ |
| $M \propto H^{1/3}$ along critical isotherm | amplitude of characteristic mode at critical compression $A \propto F_0^{1/3}$ |

Table 4.1: Analogy between phase transition of ferromagnets and wrinkling instability.

present, the linear response of ferromagnets and wrinkled structures have the same divergent scaling exponent near the critical point.

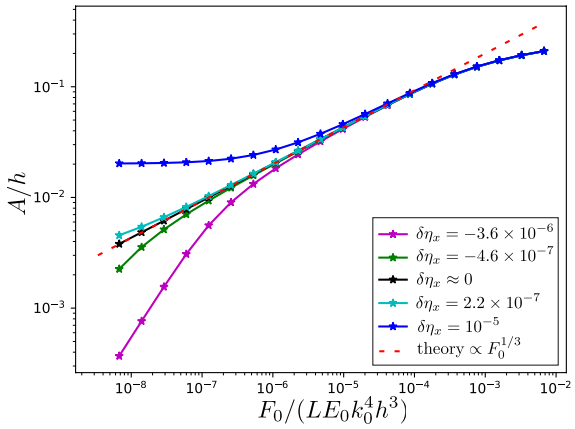


Figure 4.3: Amplitude of characteristic mode $k_0$ as a function of external force obtained from Finite Element simulation. $\delta\eta_x = \eta_x - \eta_{x,cr}$ is how much the applied compression $\eta_x$ differs from the critical compression $\eta_{x,cr}$. When $\delta\eta_x < 0$ ,the surface is flat. When $\delta\eta_x > 0$, the surface is wrinkled.

Moreover, we can make another analogy of the response of wrinkled structures to the critical scaling $M \propto H^{1/3}$ along the critical isotherm for ferromagnetism, where $H$ is the external magnetic field. For wrinkled structures at critical compression, the amplitude of characteristic mode has similar scaling behavior as $A \propto F_0^{1/3}$. The theoretical prediction, which is $A = \left(\frac{8F_0}{LE_0k_0^4}\right)^{1/3}$, can be obtained by minimizing the quartic energy functional in the presence of external forces. We verify this scaling

behavior from the Finite element simulation, as shown in Fig. 4.3. When the external force $F_0$ is small and compression $\eta_x$ is very close to the critical compression $\eta_{x,cr}$, this scaling behavior is valid.

## 4.2 General Formulation

In the previous section, we studied the response behavior of wrinkled structures due to a vertical point force located at the peak of wrinkles by analogy to the Landau phase transition model. Now we show the general formulation of the response theory in the presence of any vertical or horizontal forces.

The energy contributions from the film in Eq. (4.2,4.3) can be expressed in terms of the sum of Fourier components as follows,

$$\mathcal{U}_{\text{fb}} = \frac{1}{L}\frac{B}{2}\int \left(\frac{d^2w}{dx^2}\right)^2 dx = \frac{B}{2}\sum_k k^4 \tilde{w}(k)\tilde{w}(-k), \tag{4.17}$$

$$\mathcal{U}_{\text{fs}} = \frac{1}{L}\frac{E_0}{2}\int \epsilon_{xx}^2\, dx = \frac{E_0}{2}\sum_k \tilde{\epsilon}_{xx}(k)\tilde{\epsilon}_{xx}(-k), \tag{4.18}$$

where $\tilde{w}(k)$ and $\tilde{\epsilon}_{xx}(k)$ are the Fourier components of $w(x)$ and $\epsilon_{xx}(x)$ respectively. Also the kinematic relation in Eq. (4.1) for in-plane strain $\epsilon_{xx}$ has the following expression in Fourier space,

$$\tilde{\epsilon}_{xx}(k) = -\eta_x \delta_{k,0} + ik\tilde{u}(k) - \frac{1}{2}\sum_{k_1} k_1(k-k_1)\tilde{w}(k_1)\tilde{w}(k-k_1), \tag{4.19}$$

where $\delta_{k,0}$ is the discrete delta function. The discrete delta function is denoted as $\delta_{k,k'}$, which takes value 1 if $k = k'$ and 0 otherwise.

We treat the substrate as a 2D semi-infinite linear elastic medium. The boundary conditions between the film and the substrate are displacement continuity, i.e., the film's lower surface and the substrate's top surface share the same displacements. In

principle, the displacements at the lower surface of the film are $\left(u(x)+\frac{h}{2}w'(x), w(x)\right)$ from the kinematics of Föppl-von Kármán plate theory. However, with the assumption that $E_f/E_s \gg 1$, it is reasonable to let the displacements at the top surface of the substrate be $(u(x), w(x))$ (shown in Appendix C.1). This assumption leads to the traction at the interface of the film and substrate given by the Fourier components as [70]

$$\tilde{T}_y(k) = K_1|k|\tilde{w}(k) - K_2 ik\tilde{u}(k), \tag{4.20a}$$

$$\tilde{T}_x(k) = K_3 ik\tilde{w}(k) + K_4|k|\tilde{u}(k), \tag{4.20b}$$

where $K_1 = K_4 = \frac{2E_s(1-\nu_s)}{(1+\nu_s)(3-4\nu_s)}, K_2 = K_3 = \frac{E_s(1-2\nu_s)}{(1+\nu_s)(3-4\nu_s)}$,$\tilde{w}(k), \tilde{u}(k)$ are the Fourier components of out-of-plane and in-plane displacements of the film respectively. As a result, one can write the energy of the substrate as the sum of each Fourier mode contribution,

$$\mathcal{U}_\mathrm{s} = \frac{1}{2}\sum_k \tilde{T}_y(k)\tilde{w}(-k) + \tilde{T}_x(k)\tilde{u}(-k). \tag{4.21}$$

External forces include vertical and horizontal forces at the upper surface of the film. They are denoted as $f_y(x)$ and $f_x(x)$ respectively. The work done by these forces per length is

$$\mathcal{W} = \frac{1}{L}\int f_y(x)w(x) + f_x(x)\left(u(x) - \frac{h}{2}w'(x)\right)\, dx, \tag{4.22}$$

where we take into account the fact that the horizontal displacement at the upper surface of the film is $u(x) - \frac{h}{2}w'(x)$ due to the rotation of the film. We will show in section 4.3.2 that the contribution of plane rotation is significant for the linear response due to horizontal forces. The expression for the work done by external

forces can also be written as the sum of Fourier components as

$$\mathcal{W} = \sum_k \tilde{f}_y(k)\tilde{w}(-k) + \tilde{f}_x(k)\left(\tilde{u}(-k) - \frac{h}{2}(-ik)\tilde{w}(-k)\right), \tag{4.23}$$

where $\tilde{f}_x(k)$, $\tilde{f}_y(k)$ are the Fourier components of horizontal and vertical force densities applied at the upper surface of the film, respectively. In the end, the total energy density is

$$\mathcal{U}_{\text{total}} = \mathcal{U}_{\text{fb}} + \mathcal{U}_{\text{fs}} + \mathcal{U}_{\text{s}} - \mathcal{W}. \tag{4.24}$$

The governing equations of the displacement field of the film are derived by setting the variation of total energy density $\frac{\delta \mathcal{U}_{\text{total}}}{\delta \tilde{w}(-k)}$ and $\frac{\delta \mathcal{U}_{\text{total}}}{\delta \tilde{u}(-k)}$ to be 0, which gives

$$Bk^4\tilde{w}(k) + E_0 \sum_{k_1} k(k-k_1)\tilde{w}(k-k_1)\tilde{\epsilon}_{xx}(k_1) + \tilde{T}_y(k) = \tilde{f}_y(k) + \frac{h}{2}ik\tilde{f}_x(k) \tag{4.25a}$$

$$E_0(-ik)\tilde{\epsilon}_{xx}(k) + K_3 ik\tilde{w}(k) + \tilde{T}_x(k) = \tilde{f}_x(k). \tag{4.25b}$$

With Eq. (4.19,4.25b), we rewrite $\tilde{\epsilon}_{xx}(k)$ and $\tilde{u}(k)$ in terms of the out-of-plane displacement $\tilde{w}(k)$ as

$$\tilde{\epsilon}_{xx}(k) = \frac{1}{E_0k^2 + K_4|k|}\left[K_3k^2\tilde{w}(k) - \frac{1}{2}K_4|k|\sum_{k_1} k_1(k-k_1)\tilde{w}(k_1)\tilde{w}(k-k_1) + ik\tilde{f}_x(k)\right] \quad k \neq 0 \tag{4.26a}$$

$$ik\tilde{u}(k) = \tilde{\epsilon}_{xx}(k) + \frac{1}{2}\sum_{k_1} k_1(k-k_1)\tilde{w}(k_1)\tilde{w}(k-k_1), \tag{4.26b}$$

where $\tilde{\epsilon}_{xx}(k)$ in Eq. (4.26b) should be replaced with the expression from Eq. (4.26a). Note that $\tilde{\epsilon}_{xx}(k=0)$ is treated differently by setting $k=0$ in Eq. (4.19) as

$$\bar{\epsilon}_{xx} := \tilde{\epsilon}_{xx}(k=0) = -\eta_x + \frac{1}{2}\sum_{k_1} k_1^2\tilde{w}(k_1)\tilde{w}(-k_1), \tag{4.27}$$

where we use $\bar{\epsilon}_{xx}$ to represent $\tilde{\epsilon}_{xx}(k=0)$ from now on. The out-of-plane force balance Eq. (4.25a) can be rewritten as

$$\begin{aligned} &Bk^4\tilde{w}(k) + E_0k^2\tilde{w}(k)\bar{\epsilon}_{xx} + E_0\sum_{k_1\neq 0} k(k-k_1)\tilde{w}(k-k_1)\tilde{\epsilon}_{xx}(k_1) \\ &+ K_1|k|\tilde{w}(k) - K_2ik\tilde{u}(k) = \tilde{f}_y(k) + \frac{h}{2}ik\tilde{f}_x(k) \end{aligned} \tag{4.28}$$

where $\tilde{\epsilon}_{xx}(k)$, $\tilde{u}(k)$ and $\bar{\epsilon}_{xx}$ are related to $\tilde{w}(k)$ through Eq. (4.26a,4.26b,4.27).

With Eq. (4.28), we can solve for the out-of-plane displacement field $\tilde{w}(k)$ in the Fourier space. However, the nonlinear relations between $\tilde{\epsilon}_{xx}(k)$, $\tilde{u}(k)$ and $\tilde{w}(k)$ in Eq. (4.26a,4.26b,4.27) lead to complications. We seek to solve Eq. (4.28) perturbatively. Note that the wrinkled structures have a characteristic Fourier mode $k_0$ with the out-of-plane displacement described by $A_0\cos k_0x$, where $A_0$ is the amplitude of wrinkles. The response to infinitesimal forces can be written as a Fourier series in addition to the wrinkled state,

$$w(x) = A_0\cos(k_0x) + \sum_k \delta\tilde{w}(k)e^{ikx}, \tag{4.29}$$

which is similar to what we have done in section 4.1. Using the perturbation expansion from Eq. (4.29), we can linearize Eq. (4.28) around the wrinkled state and build matrix equations, which are presented in section 4.4. Due to the presence of nonlinear terms in Eq. (4.28), different Fourier modes are coupled, and the matrix equations have non-zero off-diagonal terms. The matrix equations can be solved numerically. However, it turns out that near the onset of wrinkling instability, different Fourier modes can be decoupled based on a few assumptions. Once Fourier modes are decoupled, the coefficient matrix of matrix equations can be easily inverted since it is diagonalized. With decoupled formalism, we can recover the Landau theory from section 4.1, and in the end, we obtain simple expressions for the response of different Fourier modes.

In section 4.3, we first discuss a decoupled response theory, where analytical expressions are obtained. Based on a few assumptions, we arrive at an energy functional where different Fourier modes are decoupled. This energy functional is essentially the Landau theory that we discussed in section 4.1. In section 4.4, we demonstrate that deviation of Fourier modes from Landau theory near the characteristic mode of wrinkles and zero modes occurs as compression is increased from the critical compression threshold. This behavior is captured by the linearized matrix equations since the coupling of different Fourier modes becomes significant with increasing compression. The formalism and results of the matrix equations are discussed in section 4.4.

## 4.3 A decoupled response theory

In this section, we will simplify Eq. (4.28) by restricting to the regime near the onset of wrinkling instability, where the amplitude of wrinkles $A_0$ is also small in addition to the small response assumption $\delta\tilde{w}(k)/A_0 \ll 1$ in the linear response regime. In this regime, we show in section 4.3.1 that the response to vertical forces is reduced to the Landau theory in section 4.1. We present a similar decoupled response theory for horizontal forces in section 4.3.2 and compare with simulation results in section 4.3.3.

### 4.3.1 Linear response due to vertical forces

We first present the response behavior of wrinkled structures due to vertical forces $f_y$ and set $f_x = 0$. We show that near the onset of wrinkling instability, i.e., $A_0 k_0 \ll 1$, different Fourier modes are decoupled.

The condition $A_0 k_0 \ll 1$ leads to a few simplifications of Eq. (4.28). First, shear traction $\tilde{T}_x(k)$ becomes negligible. This is because the shear traction acts on the displacement $\tilde{w}(k)$ through the coupling between the in-plane strain and out-of-plane

displacement, i.e., $E_0 \sum_{k_1 \neq 0} k(k-k_1)\tilde{w}(k-k_1)\tilde{\epsilon}_{xx}(k_1)$ in Eq. (4.28), where the in-plane strain depends on shear traction through Eq. (4.26a). From this coupling term, the dominant contribution of shear traction to the linear order of $\delta\tilde{w}(k)$ is $\sim A_0 k_0 \delta\tilde{w}(k)$, which is much smaller than $Bk^4\delta\tilde{w}(k)$ and $E_0 k^2 \delta\tilde{w}(k)\bar{\epsilon}_{xx}$ in Eq. (4.28). Second, with $\tilde{T}_x(k) = 0$, the in-plane force balance of Eq. (4.25b) is further simplified to be,

$$\tilde{\epsilon}_{xx}(k) = 0 \quad k \neq 0. \tag{4.30}$$

So only zero mode of in-plane strain $\bar{\epsilon}_{xx} = \tilde{\epsilon}_{xx}(k = 0)$ does not vanish, which indicates that the in-plane strain is constant. Third, when Eq. (4.30) holds, the in-plane displacement $\tilde{u}(k)$ to the first order of $\delta\tilde{w}(k)$ is $\sim A_0 k_0 \delta\tilde{w}(k \pm k_0)$ from Eq. (4.26b). This indicates that $\tilde{u}(k)$ component in $\tilde{T}_y(k)$ is negligible. Thus, with the assumption that $A_0 k_0 \ll 1$, the Eq. (4.28) can be simplified to be the following force balance equation of each mode,

$$Bk^4\tilde{w}(k) + E_0 k^2 \bar{\epsilon}_{xx}\tilde{w}(k) + K_1|k|\tilde{w}(k) = \tilde{f}_y(k), \tag{4.31}$$

where different Fourier modes are decoupled. Each Fourier mode $k$ behaves as a linear spring in response to external forces with the stiffness

$$m(k) = Bk^4 + E_0 k^2 \bar{\epsilon}_{xx} + K_1|k|, \tag{4.32}$$

which is independent of the external forces. The corresponding energy functional of Eq. (4.31) is

$$\mathcal{U}_{\text{total}} = \sum_k \frac{1}{2} Bk^4\tilde{w}(k)\tilde{w}(-k) + \frac{1}{2} E_0 k^2 \bar{\epsilon}_{xx}\tilde{w}(k)\tilde{w}(-k) + \frac{1}{2} K_1|k|\tilde{w}(k)\tilde{w}(-k) - \tilde{f}_y(k)\tilde{w}(-k), \tag{4.33}$$

which is equivalent to the energy functional of Landau theory in section 4.1 [see Eq. (4.9)] considering that the expansion of displacement in section 4.1 [see Eq. (4.8)] restricts $k > 0$ compared to the expansion in Eq. (4.29). Thus, we conclude that the Landau theory fully describes the linear response of wrinkled structures to vertical forces near the onset of instability, i.e., with condition $A_0 k_0 \ll 1$.

In section 4.4, we will study the response behavior when the loading parameter $\eta_x$ is moderately above the instability threshold $\eta_{x,cr}$. The Landau theory, where different Fourier modes are decoupled, works well near the instability threshold. As $\eta_x$ increases, the response of Fourier modes that are close to zero mode and characteristic Fourier mode deviates from the theoretical prediction of Landau theory. We can improve the prediction by solving the matrix equations considering the interaction of different Fourier modes.

### 4.3.2 Linear response due to horizontal forces

In this section, we present the response behavior of wrinkled structures due to horizontal forces $f_x$ and set $f_y = 0$. With the same assumption in section 4.3.1 that $A_0 k_0 \ll 1$, Eq. (4.28) can again be simplified such that Fourier modes of vertical displacement are decoupled and have the stiffness given in Eq. (4.32).

We still need to know how the horizontal forces act on the vertical displacement in Eq. (4.28). Here we show that there are three contributions. First, with $A_0 k_0 \ll 1$, we have concluded in section 4.3.1 that the shear traction $\tilde{T}_x(k)$ can be neglected. Then the in-plane force balance [see Eq. (4.25b)] gives

$$\tilde{\epsilon}_{xx}(k) = -\frac{1}{iE_0 k}\tilde{f}_x(k) \quad k \neq 0, \tag{4.34}$$

which, unlike the Eq. (4.30) for response to vertical forces, are non-zero. Thus, the contribution of horizontal forces through the coupling between in-plane strain and

out-of-plane displacement in Eq. (4.28) is

$$E_0 \sum_{k_1 \neq 0} k(k-k_1)\tilde{w}(k-k_1)\tilde{\epsilon}_{xx}(k_1) = \begin{cases} \frac{iA_0kk_0}{2}\left(\frac{\tilde{f}_x(k-k_0)}{k-k_0} - \frac{\tilde{f}_x(k+k_0)}{k+k_0}\right) & k \neq \pm k_0 \\ \mp\frac{iA_0k_0}{4}\tilde{f}_x(\pm 2k_0) & k = \pm k_0 \end{cases} \tag{4.35}$$

Second, due to the rotation of the film, the right-hand side of Eq. (4.28) has a term $\frac{h}{2}ik\tilde{f}_x(k)$. This second contribution is on the same order as Eq. (4.35) since $A_0 \sim h$, which also shows that the effect of considering external forces applied at the top surface of the film instead of the central surface is not negligible when we proposed Eq. (4.22). Third, from Eq. (4.26b,4.34), the in-plane displacement $\tilde{u}(k)$ is

$$\begin{aligned} ik\tilde{u}(k) &= \tilde{\epsilon}_{xx}(k) \\ &= -\frac{1}{iE_0k}\tilde{f}_x(k), \end{aligned} \tag{4.36}$$

where the term involving out-of-plane displacement in Eq. (4.26b) is neglected since the leading order is $\sim A_0k_0\delta\tilde{w}(k \pm k_0)$ and $A_0k_0 \ll 1$. Thus, the term $-K_2ik\tilde{u}(k)$ in Eq. (4.28) that comes from the normal traction $\tilde{T}_y(k)$ becomes

$$-K_2ik\tilde{u}(k) = K_2\frac{1}{iE_0k}\tilde{f}_x(k). \tag{4.37}$$

With all three contributions from horizontal forces and the stiffness [see Eq. (4.32)] for each Fourier mode, the response of non-characteristic modes can be written as a function of normalized wavenumber $q = k/k_0$,

$$\delta\tilde{w}(qk_0) = \frac{i(2B)^{2/3}\left(A_0E_0k_0^2q^2\left(\frac{\tilde{f}_x(qk_0+k_0)}{q+1} - \frac{\tilde{f}_x(qk_0-k_0)}{q-1}\right) + (2K_2 + hE_0k_0^2q^2)\tilde{f}_x(qk_0)\right)}{E_0K_1^{5/3}q(-3q^2+q^4+2|q|)} \quad q \neq \pm 1. \tag{4.38}$$

For the characteristic Fourier mode,

$$\delta\tilde{w}_e(k_0) = \frac{iB\left((2hE_0k_0^2+4K_2)\left(\tilde{f}_x(k_0)-\tilde{f}_x(-k_0)\right)+A_0E_0k_0^2\left(\tilde{f}_x(2k_0)-\tilde{f}_x(-2k_0)\right)\right)}{4E_0^2K_1(\eta_x-\eta_{x,cr})} \tag{4.39a}$$

$$0\,\delta\tilde{w}_o(k_0) = -(2hE_0k_0^2+4K_2)\left(\tilde{f}_x(k_0)+\tilde{f}_x(-k_0)\right)-A_0E_0k_0^2\left(\tilde{f}_x(2k_0)+\tilde{f}_x(-2k_0)\right) \tag{4.39b}$$

where $\delta\tilde{w}_e(k_0) = (\delta\tilde{w}(k_0)+\delta\tilde{w}(-k_0))$ and $\delta\tilde{w}_o(k_0) = i(\delta\tilde{w}(k_0)-\delta\tilde{w}(-k_0))$ are the even and odd part of characteristic Fourier mode $k_0$ respectively. Note that the stiffness of $\delta\tilde{w}_o(k_0)$ is 0 in the linear response regime. To avoid large deformation and work in the linear response regime, the external force terms on the right-hand side of Eq. (4.39b) should vanish. Thus, we apply a pair of horizontal forces equal in magnitude, opposite directed, and symmetric to the peak or the valley of wrinkles. Fig. 1.2(c) shows one example of such symmetric horizontal forces. This work will mainly focus on the response to such forces. We will briefly discuss in section 4.3.4 the mechanical response of wrinkled structures to horizontal forces that can excite odd characteristic mode and induce large deformation.

We first consider a pair of horizontal forces symmetric to the peak of wrinkles and place the y-axis through the peak without loss of generality. Due to symmetry, only the even part of $\delta\tilde{w}(k)$ is nonzero. The response of even modes $\delta\tilde{w}_e(k) = (\delta\tilde{w}(k)+\delta\tilde{w}(-k))$ is,

$$\delta\tilde{w}_e(qk_0) = \frac{(2B)^{2/3}\left(A_0E_0k_0^2q^2\left(\frac{\tilde{f}_{x,o}(qk_0+k_0)}{q+1}-\frac{\tilde{f}_{x,o}(qk_0-k_0)}{q-1}\right)+(hE_0k_0^2q^2+2K_2)\tilde{f}_{x,o}(qk_0)\right)}{E_0K_1^{5/3}q(-3q^2+q^4+2|q|)} \quad q\neq 1 \tag{4.40a}$$

$$\delta\tilde{w}_e(k_0) = \frac{B\left((2hE_0k_0^2 + 4K_2)\tilde{f}_{x,o}(k_0) + A_0E_0k_0^2\tilde{f}_{x,o}(2k_0)\right)}{4E_0^2K_1(\eta_x - \eta_{x,cr})}, \tag{4.40b}$$

where $\tilde{f}_{x,o}(k) = i\left(\tilde{f}_x(k) - \tilde{f}_x(-k)\right)$, $q = k/k_0 > 0$. Eq. (4.40) shows that the even modes $\delta\tilde{w}_e(k)$ are only coupled to the odd part of horizontal forces. Similarly, when a pair of horizontal forces is symmetric to the valley of wrinkles which is aligned with y-axis, only the even Fourier modes $\delta\tilde{w}_e(k)$ survive, the expressions of which are Eq. (4.40) with $A_0$ changed to $-A_0$. We present a few implications from Eq. (4.40) in the following discussions.

**Response diverges near the onset of instability if forces are coupled to the characteristic mode**

In section 4.1, we showed that a vertical point force applied at the peak of wrinkles induces a large deformation near the onset of wrinkling instability, which is due to the divergence of the characteristic Fourier mode in the linear response regime [see Eq. (4.15a,4.16a)]. Similarly, Eq. (4.40b) indicates that the linear response due to a pair of horizontal forces also diverges at the onset of wrinkling instability if the external forces are coupled to the characteristic mode, i.e., if the numerator in Eq. (4.40b) is nonzero. One can show that $\tilde{f}_{x,o}(k_0)$ and $\tilde{f}_{x,o}(2k_0)$ in the numerator of Eq. (4.40b) both vanish when the pair of horizontal forces are applied symmetrically at the peaks. When the pair of horizontal forces are applied at midpoints but still symmetric to the peak or the valley of wrinkles, $\tilde{f}_{x,o}(k_0) \neq 0$ and $\tilde{f}_{x,o}(2k_0) = 0$. Both $\tilde{f}_{x,o}(k_0)$ and $\tilde{f}_{x,o}(2k_0)$ are nonzero in other scenarios. Thus, we conclude that wrinkled structures should have a divergent response due to a pair of horizontal forces near the instability threshold except for forces applied at the peaks.

We further carry out the FEM simulations and measure the linear response due to a pair of horizontal forces. Fig. 4.4 shows the simulation results of the response as a function of the loading parameter $\eta_x$ for two different locations of applied forces (see

the schematic insets for the application of forces). The additional vertical displacements $\Delta w(0)$ due to external forces are measured at the valley point between two forces. In Fig. 4.4(a), forces are applied at midpoints. These forces are coupled to the characteristic Fourier mode with $\tilde{f}_{x,o}(k_0) \neq 0$. In Fig. 4.4(b), forces are applied at neighboring peaks. They are not coupled to the characteristic mode since $\tilde{f}_{x,o}(k_0) = 0$ and $\tilde{f}_{x,o}(2k_0) = 0$. Note that we use a tiny incremental step for loading parameter $\eta_x$ near the instability threshold since the large response only occurs close to the threshold. The results in Fig. 4.4 confirm our argument about whether the response

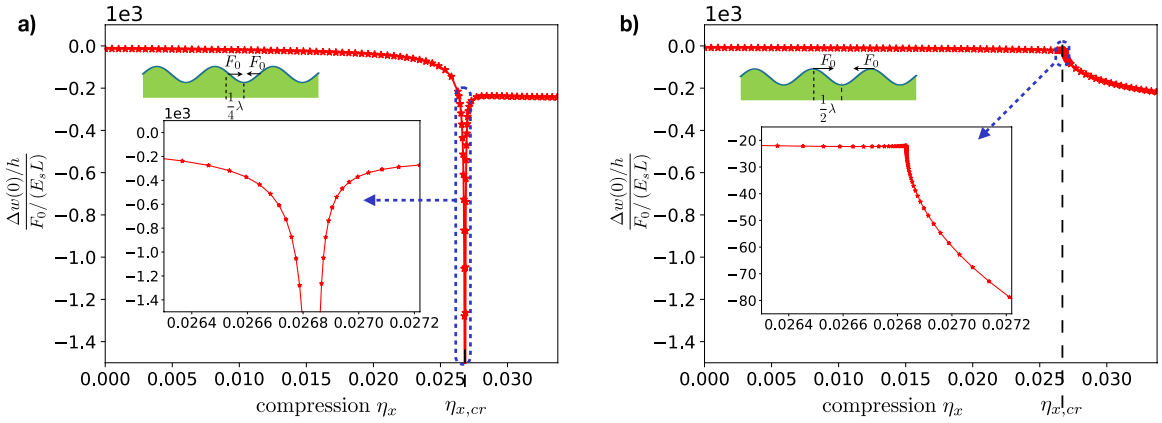


Figure 4.4: Response of wrinkled structures to a pair of horizontal forces as a function of loading parameter $\eta_x$. This figure presents the simulation results with $E_f/E_s = 100$, for which the corresponding instability threshold is $\eta_{x,cr} = 0.02684$. We measure the additional displacement $\Delta w(0)$ at the valley between two point forces to quantify the response. (a) A pair of horizontal forces are applied at neighboring midpoints of wrinkles. The curve in the inset is the zoom-in view of the response curve near the threshold. (b) A pair of horizontal forces are applied at neighboring peaks of wrinkles. We did not observe a significant response near the threshold since the forces are not coupled to the characteristic mode.

due to horizontal forces diverges. For the same reason, we can argue that the response to vertical forces should not diverge at the instability if forces are not coupled to the characteristic Fourier mode. One can show that a pair of vertical forces at neighboring midpoints is not coupled to the characteristic Fourier mode and, thus, can not induce a significant response. However, this is not easy to be verified in simulations since forces in FEM simulations have to be applied at specific mesh nodes, which might

not be precisely located in the middle between neighboring peak and valley points. We observed in simulations that near the instability threshold, the response to a pair of vertical forces almost located at midpoints is much smaller than the response to forces at other locations.

**Response to horizontal forces gradually increases beyond the instability**

In Fig. 4.4, the response to horizontal forces gradually increases beyond the instability after the divergent response dies out. As shown in the Eq. (4.40), the horizontal forces in the numerator are amplified by the amplitude $A_0$, which grows with increasing compression as $A_0 \sim \sqrt{\eta_x - \eta_{x,cr}}$. Thus, our theory in Eq. (4.40) indeed predicts an increase in the response.

In comparison, the response to vertical forces shown in Fig. 4.2(a) stays almost constant beyond the instability. Eq. (4.16) provides a consistent prediction, where the characteristic mode decays away from the instability threshold while other Fourier modes do not change with increasing compression. A slight decrease of response in Fig. 4.2(a) can be accounted for by the interaction of different Fourier modes, which we will discuss in section 4.4.

### 4.3.3 Comparison between simulation and theory for the response due to horizontal forces

The decoupled response theory in Eq. (4.40) describes the linear response of wrinkled structures due to horizontal forces for each Fourier mode. We performed FEM simulations and compared the results with the theoretical predictions. Specifically, we put the horizontal forces symmetric to the valley, as shown in Fig. 4.5(a). As discussed in section 4.3.2, the vertical displacement has to be an even function to the origin due to symmetry. Similarly, the horizontal displacement has to be an odd function. Fig. 4.5(b,e,h) present the vertical and horizontal displacements in

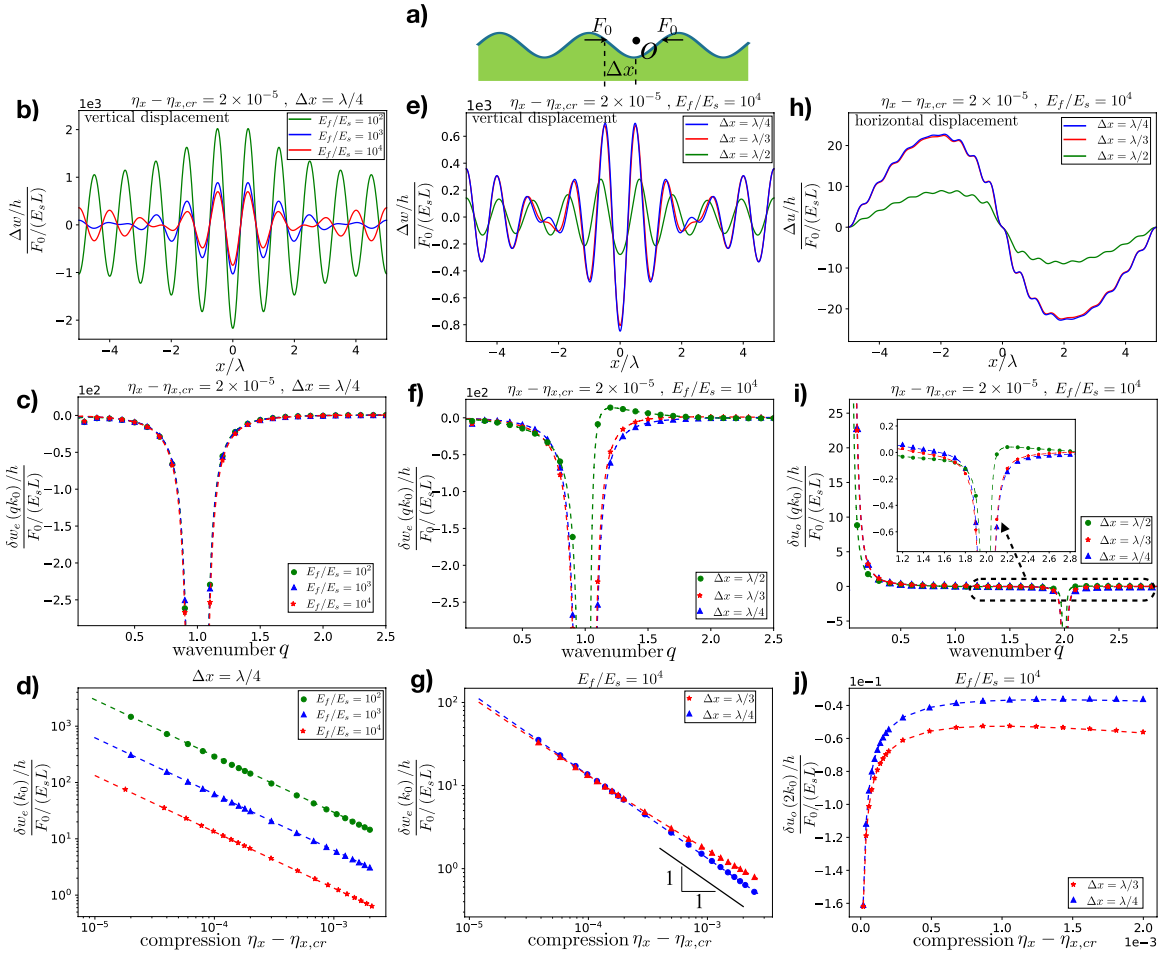


Figure 4.5: Vertical and horizontal displacements due to horizontal forces for different ratios of elastic constants and locations of forces. Results are shown in the real space (top row), the Fourier space for non-characteristic mode (middle row), and characteristic mode (bottom row) with the comparison between simulations (symbols) and theory (lines). (a) A schematic of the horizontal forces, symmetric to the origin $O$ at the valley with a distance $\Delta x$. (b-d) Vertical displacements for different elastic ratios when $\Delta x = \lambda/4$ where $\lambda$ is the wavelength of the wrinkles. (e-g) Vertical displacements for the same elastic ratios $E_f/E_s = 10^4$ but different $\Delta x$. Note that (g) does not show the response of characteristic mode when $\Delta x = \lambda/2$ since it vanishes. (h-j) Horizontal displacements for different $\Delta x$ but the same elastic ratios $E_f/E_s = 10^4$. (j) $\delta u_o(2k_0)$ vanishes when $\Delta x = \lambda/2$.

real space for different ratios of elastic constants and locations of forces. We further compared the FEM simulation results with the theory in Fourier space. Note that the Fourier mode response is negative if that mode goes down at the origin. As shown in Fig. 4.5(c,f), for different ratios of elastic constants and locations of forces, the theoretical predictions of vertical displacements all agree well with the simulation results. Besides, Fig. 4.5(c,f) show that most of the response Fourier modes are negative. Also, the characteristic mode is negative for all the scenarios presented in Fig. 4.5(c,f). The accumulation of all negative modes leads to the wrinkled structure being pushed down by the horizontal forces at the origin, as shown in Fig. 4.5(b,e) for the vertical displacement in real space.

The linear response of the characteristic Fourier mode due to horizontal forces is described by Eq. (4.40b), which has contributions from horizontal forces as $\tilde{f}_{x,o}(k_0)$ and $\tilde{f}_{x,o}(2k_0)$. Note that $\tilde{f}_{x,o}(2k_0)$ in Eq. (4.40b) has a prefactor $A_0$, which has the scaling $A_0 \sim \sqrt{\eta_x - \eta_{x,cr}}$ and is tiny when $\eta_x \approx \eta_{x,cr}$. Thus, near the onset of instability, $\tilde{f}_{x,o}(k_0)$ dominates and the response of characteristic mode $\delta\tilde{w}(k_0) \sim \frac{1}{\eta_x - \eta_{x,cr}}$. For compression $\eta_x$ moderately above the critical threshold, $\tilde{f}_{x,o}(2k_0)$ will take over if $\tilde{f}_{x,o}(2k_0) \neq 0$ and the scaling exponent will gradually changes from $-1$.

Fig. 4.5(g) presents the scaling behavior of characteristic mode from simulations, which agree with the theory. When $\Delta x = \frac{1}{3}\lambda$, where $\lambda$ is the wavelength of wrinkles, both $\tilde{f}_{x,o}(k_0)$ and $\tilde{f}_{x,o}(2k_0)$ are nonzero. So as shown by the red symbols and curve in Fig. 4.5(g), with increasing compression from critical threshold, $\delta\tilde{w}(k_0)$ initially scales as $\delta\tilde{w}(k_0) \sim \frac{1}{\eta_x - \eta_{x,cr}}$. Later, when compression is large enough, the scaling exponent gradually changes. When two point forces are at two neighboring midpoints, i.e., $\Delta x = \frac{1}{4}\lambda$, $\tilde{f}_{x,o}(2k_0) = 0$ so the response theory predicts that the scaling exponent keeps being $-1$, which is shown by the blue curve in Fig. 4.5(g) and also results in Fig. 4.5(d).

Once we know the vertical displacement, we can calculate the horizontal displacement in Fourier space from Eq. (4.26b,4.34). The Fourier components of horizontal displacement are

$$\delta u(qk_0) = \frac{\tilde{f}_x(qk_0)}{E_0 k_0^2 q^2} - \frac{iAk_0((q-1)\delta\tilde{w}(qk_0 - k_0) - (q+1)\delta\tilde{w}(qk_0 + k_0))}{2q}. \tag{4.41}$$

Due to symmetry, the odd part of horizontal displacement $\delta u_o(qk_0) = i(\delta u(qk_0) - \delta u(-qk_0))$ is nonzero

$$\delta u_o(qk_0) = \frac{\tilde{f}_{x,o}(qk_0)}{E_0 k_0^2 q^2} + \frac{Ak_0((q-1)\delta\tilde{w}_e(qk_0 - k_0) - (q+1)\delta\tilde{w}_e(qk_0 + k_0))}{2q}, \tag{4.42}$$

while the even part vanishes. The horizontal displacements in real and Fourier space for different locations of forces are present in Fig. 4.5(h-j), which shows excellent agreement between simulations and theory.

### 4.3.4 Large response of wrinkled structures due to odd characteristic mode

In section 4.3.2, we showed that the odd characteristic Fourier mode has zero stiffness. So when this mode is excited by external forces, wrinkled structures have a large response that the linear response model does not capture. In Fig. 4.6, we present the FEM simulation results of the large response behavior. To be consistent with our Fourier mode formalism, we use periodic boundary conditions in the simulations, details of which are illustrated in the appendix C.2.

Fig. 4.6(a) presents the large response due to a vertical point force at the midpoint. The wrinkle profile rearranges itself such that the location of the vertical point force becomes the peak of wrinkles after deformation. On top of the new wrinkle

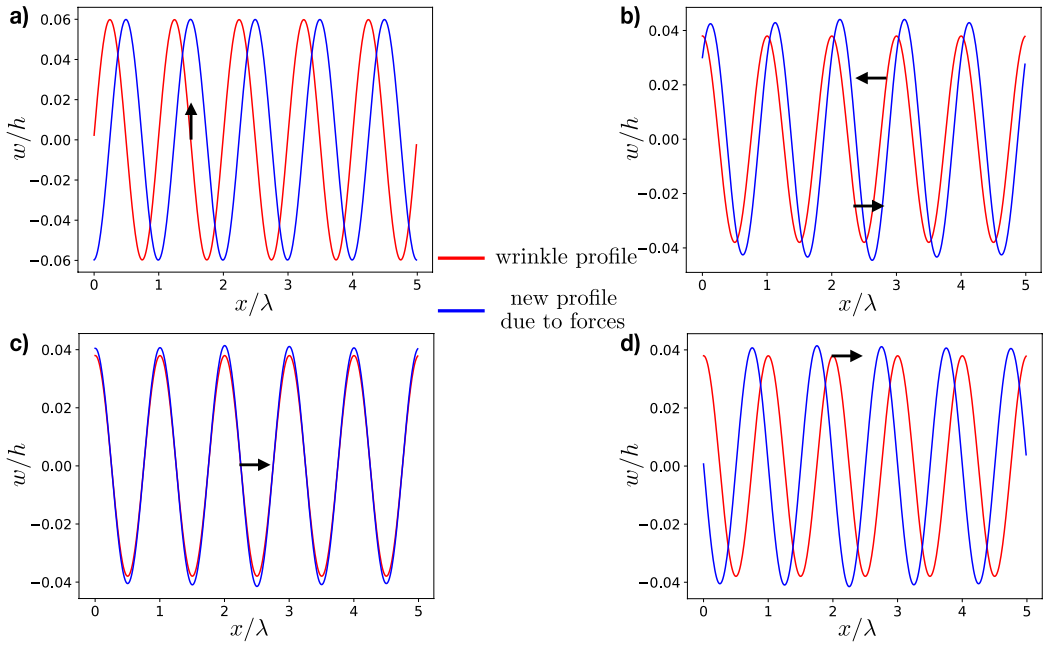


Figure 4.6: Response of wrinkled structures due to the application of asymmetric forces. Arrows indicate the position and direction of the external forces.

profile, additional linear response due to the infinitesimal vertical point force obeys the response theory in section 4.3.1.

We can understand the rearrangement of wrinkles as follows. We consider the following Lagrangian

$$\mathcal{L} = \mathcal{E} - F_0 w(x_0), \tag{4.43}$$

where $\mathcal{E}$ is the elastic energy of wrinkled structures and $F_0 w(x_0)$ is the work done by the point force $F_0$ at location $x_0$. With periodic boundary conditions, the elastic energy $\mathcal{E}$ of wrinkles does not change by rearranging the waves; that is, all rearrangements of wrinkle waves are degeneracies of the minimum of $\mathcal{E}$. When a point force is applied, the work done by the force is maximized to minimize the Lagrangian. So the wrinkles shift such that the location, $x_0$, where the point force is applied, becomes the peak. This point force breaks the translational symmetry and lifts the degeneracy of wrinkled structures. Note that suppose we use boundary conditions other than being

periodic. In that case, there is no such degeneracy of rearranging wrinkles, and the response can be more complicated. However, the response should still be large.

Fig. 4.6(b) presents the large response due to a horizontal force couple not symmetric to the peak or the valley. After deformation, the wrinkle profile rearranges itself such that the force couple becomes symmetric to the peak or the valley. On top of the new wrinkle profile, wrinkle structures respond linearly to the horizontal forces described by the theory in section 4.3.2. If a single point force in the horizontal direction is applied, as shown in Fig. 4.6(d), the wrinkle profile will rearrange itself such that the location of the point force becomes the midpoint of wrinkles. Note that the horizontal displacement at the upper surface of the film is $u(x) - \frac{h}{2}w'(x)$, and the midpoint of the wrinkle profile has the maximum $|w'(x)|$. Thus, the work done by the force is maximized, so the corresponding Lagrangian is minimized. Fig. 4.6(c) shows that the wrinkle profile does not shift if the horizontal point force is applied at the midpoint of wrinkles.

## 4.4 Linear response with compression moderately above the instability threshold

The decoupled response theory in section 4.3 agrees with FEM simulation near the onset of wrinkling instability. However, we will show in this section that, as the loading parameter $\eta_x$ increases from $\eta_{x,cr}$, simulation results deviate from the prediction of decoupled response theory. The deviation occurs because the assumption $A_0 k_0 \ll 1$ used in section 4.3 only holds near the instability threshold. As $\eta_x$ increases, $A_0$ increases and scales as $A_0 \sim \sqrt{\eta_x - \eta_{x,cr}}$. In this section, we drop the assumption that $A_0 k_0 \ll 1$. We seek to linearize Eq. (4.28) around the wrinkled state using the perturbation expansion of Eq. (4.29) and build matrix equations, which have off-diagonal terms due to the coupling of different Fourier modes.

Here we present the linearized expressions of different components in Eq. (4.28). The in-plane strain $\tilde{\epsilon}_{xx}(k)$ from Eq. (4.26a) is

$$\begin{aligned}\tilde{\epsilon}_{xx}(k\neq 0) = &\frac{1}{8(E_0k^2+K_4|k|)}\left(4K_3k^2(A_0\delta_{k,k_0}+A_0\delta_{k,-k_0}+2\delta\tilde{w}(k))\right.\\ &\left.-A_0k_0^2K_4|k|(A_0\delta_{k,2k_0}+A_0\delta_{k,-2k_0}+4(k-k_0)\delta\tilde{w}(k-k_0)-4(k+k_0)\delta\tilde{w}(k+k_0))\right),\end{aligned} \tag{4.44}$$

where $\delta_{k,k'}$ is the discrete delta function that takes value 1 if $k=k'$ and 0 otherwise. At linear order of $\delta\tilde{w}(k)$, term $E_0\sum_{k_1\neq 0}k(k-k_1)\tilde{w}(k-k_1)\tilde{\epsilon}_{xx}(k_1)$ in Eq. (4.28) becomes

$$\begin{aligned}&\frac{1}{8}A_0E_0kk_0\times\\ &\left(-\frac{A_0k_0K_4\left((k-2k_0)\,\delta\tilde{w}\,(k-2k_0)+(k+2k_0)\,\delta\tilde{w}\,(k+2k_0)\right)}{2E_0k_0+K_4}\right.\\ &+\frac{4K_3\left((k-k_0)\,\delta\tilde{w}\,(k-k_0)+(k+k_0)\,\delta\tilde{w}\,(k+k_0)\right)}{E_0k_0+K_4}\\ &+\frac{1-\delta_{k,k_0}}{E_0\,(k-k_0)^2+K_4\,|k-k_0|}\times\\ &\quad 2\left(2K_3\,(k-k_0)^2\,\delta\tilde{w}\,(k-k_0)+A_0k_0K_4\,|k-k_0|\,(-(k-2k_0)\,\delta\tilde{w}\,(k-2k_0)+k\delta\tilde{w}(k))\right)\\ &-\frac{1-\delta_{k,-k_0}}{E_0\,(k+k_0)^2+K_4\,|k+k_0|}\times\\ &\quad\left.2\left(2K_3\,(k+k_0)^2\,\delta\tilde{w}\,(k+k_0)+A_0k_0K_4\,|k+k_0|\,(-k\delta\tilde{w}(k)+(k+2k_0)\,\delta\tilde{w}\,(k+2k_0))\right)\right)\end{aligned} \tag{4.45}$$

Term $K_2ik\tilde{u}(k)$ in Eq. (4.28) becomes

$$\frac{K_2k^2\left[2K_3\delta\tilde{w}(k)+A_0k_0E_0((k-k_0)\delta\tilde{w}(k-k_0)-(k+k_0)\delta\tilde{w}(k+k_0))\right]}{2(E_0k^2+K_4|k|)} \tag{4.46}$$

Other terms on the left-hand side of Eq. (4.28) to the linear order are summarized below

$$\begin{aligned}&Bk^4\delta\tilde{w}(k)+E_0k^2\delta\tilde{w}(k)(-\eta_x+\frac{1}{4}A_0^2k_0^2)+K_1|k|\delta\tilde{w}(k)\\ &+(\delta_{k,k_0}+\delta_{k,-k_0})\frac{1}{4}E_0A_0^2k_0^4(\delta\tilde{w}(-k_0)+\delta\tilde{w}(k_0)),\end{aligned} \tag{4.47}$$

which also appears in the Landau theory in section 4.1. With Eq. (4.45,4.46,4.47), we obtain the expansion of Eq. (4.28) to the linear order of $\delta\tilde{w}(k)$, which contains the Fourier modes ranging from $k-2k_0$ to $k+2k_0$ and separated by one characteristic mode, $k_0$, in k-space. The linearized form of Eq. (4.28) can be written as,

$$\sum_{n=-2}^{2} c_{k+nk_0}\delta\tilde{w}\left(k+nk_0\right) = \tilde{f}_y(k) + \mathcal{F}[\tilde{f}_x(k)] \tag{4.48}$$

where $\mathcal{F}[\tilde{f}_x(k)]$ is how the horizontal forces are coupled to the vertical displacement and has been derived in section 4.3.2. Due to the coupling of different Fourier modes, Eq. (4.48) cannot be inverted symbolically. We need to construct the corresponding matrix equations and solve them numerically. We choose a system of size $L$ such that the characteristic Fourier mode is $k_0 = \frac{2\pi}{L}n_0$ where $n_0$ is an integer. For a given wavenumber $k = \frac{2\pi}{L}n$, the corresponding normalized wavenumber $q$ is $q = k/k_0 = n/n_0$. The spacing in k-space is $\frac{2\pi}{L}$. We also truncate the k-space to be within $(-\frac{\pi}{a}, \frac{\pi}{a}]$ where $a$ is the mesh size in simulations and assume a periodic boundary condition in k-space.

### 4.4.1 Response to a vertical point force at compression moderately above the instability threshold

We place the vertical point force at the peak of the wrinkles for simplicity. Fig. 4.7 shows the comparison of FEM results, decoupled response theory, and coupled matrix equations. Note that we choose the length $L$ of the system much bigger than what was used for simulations in Fig. 4.2(b), so the data points in k-space in Fig. 4.7 are much denser, and there are points much closer to the characteristic Fourier mode ($q = 1$) of wrinkles and zero modes. Specifically, we choose the system's length $L$ to have 30 waves of wrinkles. Fig. 4.7 shows that, with the increase of loading parameter $\eta_x$, the simulation results of Fourier modes near the characteristic mode of wrinkles

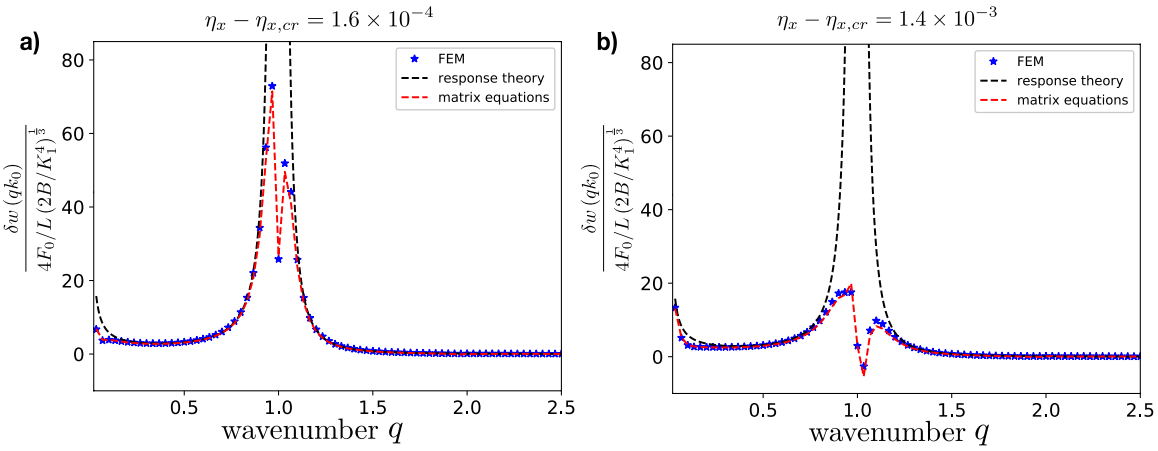


Figure 4.7: Comparison of results from FEM simulations, decoupled response theory Eq. (4.16b), and matrix equations for the response to a vertical point force at the peak of wrinkles. For the results presented here, we choose $E_f/E_s = 100$, system's length $L = 30\lambda$, where $\lambda = 2\pi/k_0$ is the wavelength of wrinkles. The loading parameter is $\eta_x - \eta_{x,cr} = 1.6 \times 10^{-4}$ and $1.4 \times 10^{-3}$ for (a) and (b) respectively. With increasing $\eta_x$, the results from matrix equations trace the evolution of Fourier modes obtained from FEM simulations.

and zero modes deviate from the prediction of the decoupled Landau response theory. The results of the matrix equations give better prediction and capture the trend of the evolution of all the Fourier modes with increasing compression. Note that the response will only be even modes due to symmetry as we put the vertical point force at the peak. Negative $\delta\tilde{w}(k)$ in Fig. 4.7 are the modes that go down at the peak where force is applied. Fig. 4.7 shows that some modes change sign as compression $\eta_x$ increases, which is captured by the matrix equations.

### 4.4.2 Response to a pair of horizontal forces at compression moderately above the instability threshold

In this section, we present the results of matrix equations in the presence of horizontal forces. We first place a pair of horizontal forces symmetric to the valley, as shown by the schematic of Fig. 4.8(a). In Fig. 4.8, we present the comparison of FEM simulation, decoupled response theory, and matrix equations for different locations of forces

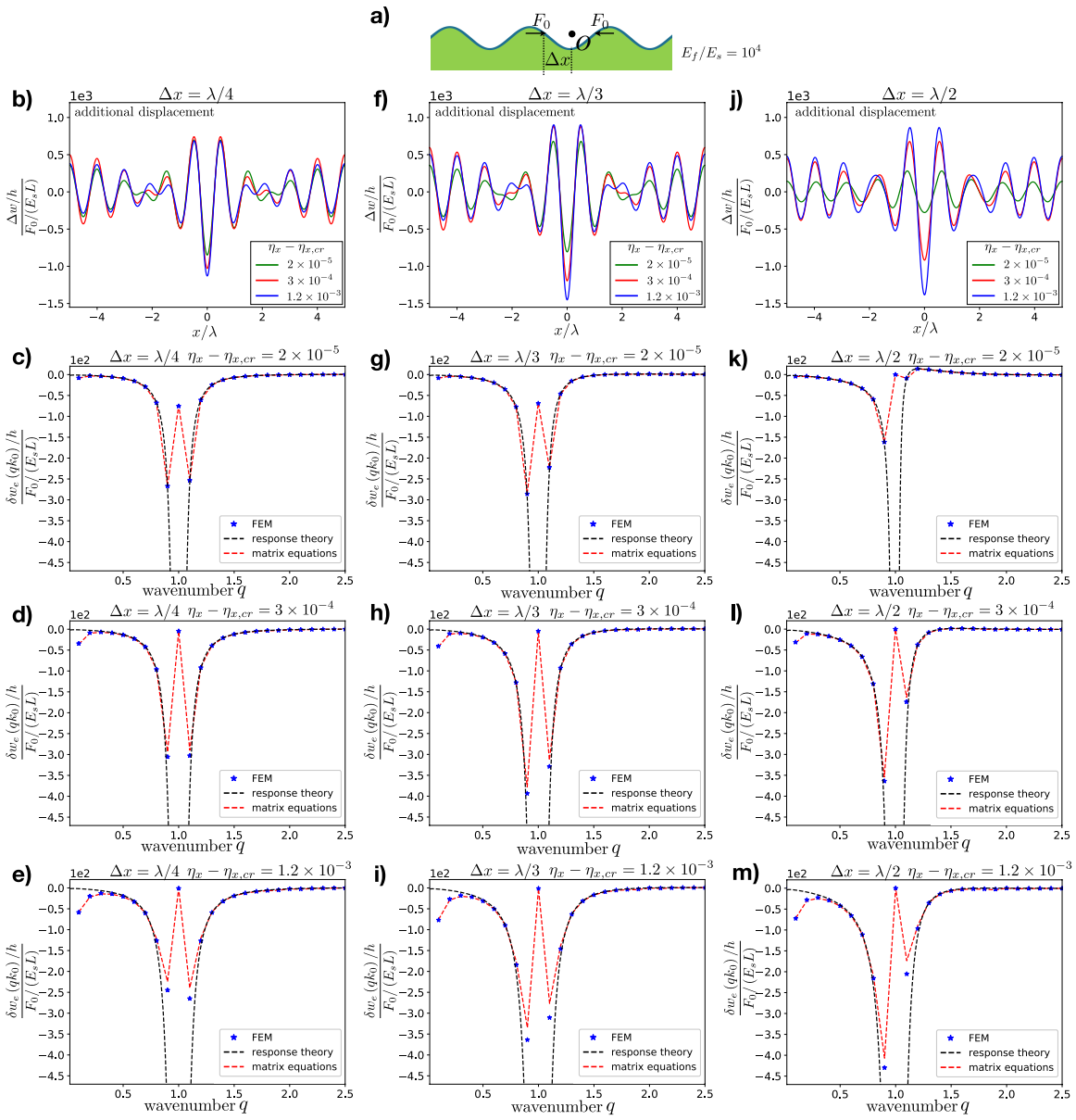


Figure 4.8: Vertical displacements due to a pair of horizontal forces symmetric to the valley when compression $\eta_x$ is moderately above the instability. Results are shown in the real space (top row) and Fourier space (bottom three rows) with the comparison between simulations (symbols), decoupled response theory (black lines), and matrix equations (red lines). (a) A schematic of the horizontal forces, symmetric to the origin $O$ at the valley with a distance $\Delta x$. The ratio of elastic constants is $E_f/E_s = 10^4$ for all results. The corresponding critical threshold is $\eta_{x,cr} = 0.0012$. Each column presents the results for different $\Delta x$. (b-e) $\Delta x = \lambda/4$. (f-i) $\Delta x = \lambda/3$. (j-m) $\Delta x = \lambda/2$. The results in Fourier space (bottom three rows) have compression $\eta_x - \eta_{x,cr}$ as $2 \times 10^{-5}$, $3 \times 10^{-4}$,$1.2 \times 10^{-3}$ from top to bottom.

$\Delta x$ and loading parameter $\eta_x$. We choose the system size $L$ to have 10 waves of wrinkles, which is the same as what was used for simulations in Fig. 4.5. As $\eta_x$ increases (from the second row to the last row in Fig. 4.5), simulation results of Fourier modes near the characteristic mode and zero modes deviate from the decoupled response theory. However, the matrix equations capture the evolution of simulation results with increasing $\eta_x$.

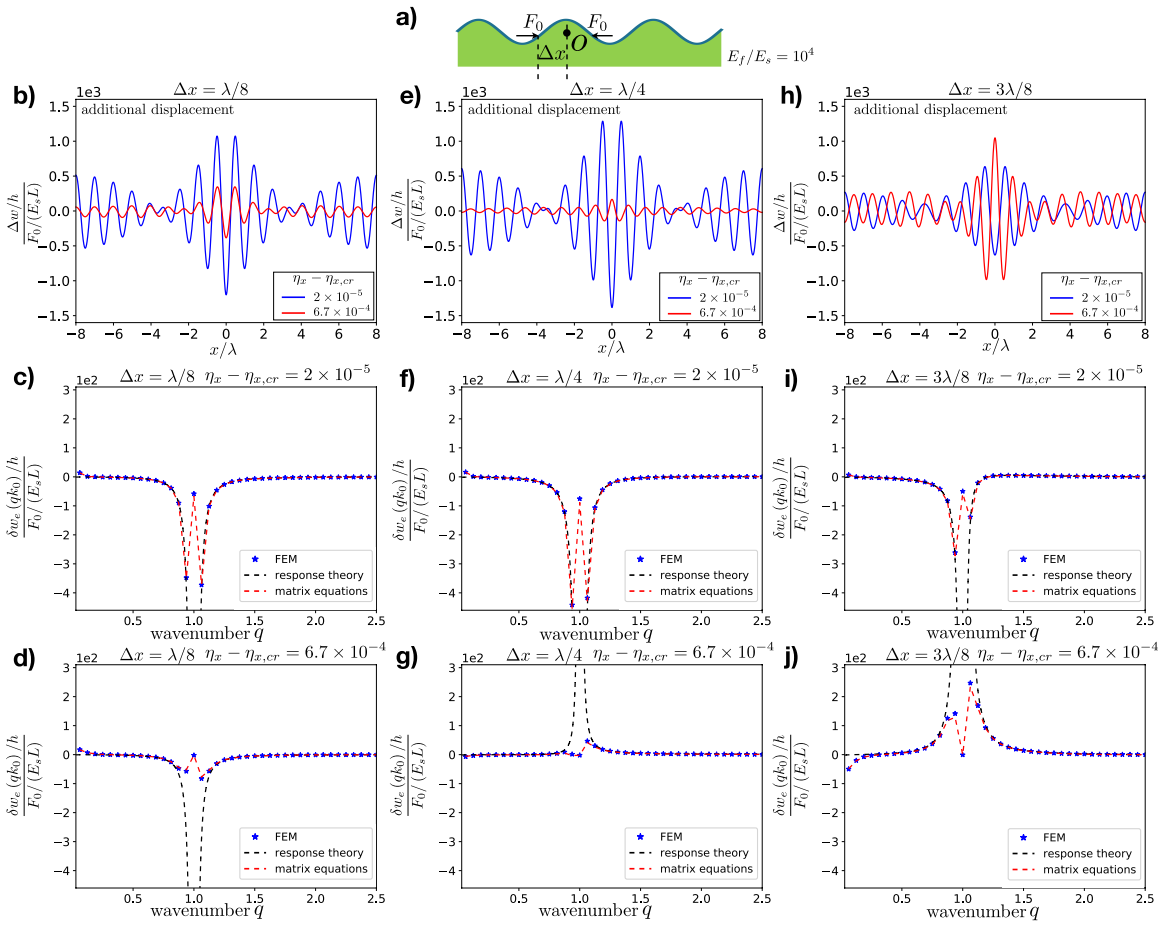


Figure 4.9: Vertical displacements due to a pair of horizontal forces symmetric to the peak. Results are shown in the real space (top row) and Fourier space (bottom two rows) with the comparison between simulations (symbols), decoupled response theory (black lines), and matrix equations (red lines). (a) A schematic of the horizontal forces, symmetric to the origin $O$ at the peak with a distance $\Delta x$. The ratio of elastic constants is $E_f/E_s = 10^4$ for all results. The corresponding critical threshold is $\eta_{x,cr} = 0.0012$. Each column presents the results for different $\Delta x$. (b-d) $\Delta x = \lambda/8$. (e-g) $\Delta x = \lambda/4$. (h-j) $\Delta x = 3\lambda/8$. The results in Fourier space (bottom two rows) have compression $\eta_x - \eta_{x,cr}$ as $2 \times 10^{-5}$, $6.7 \times 10^{-4}$ from top to bottom.

In Fig. 4.9, we present similar results for the response to a pair of horizontal forces symmetric to the peak of wrinkles, the schematic of which is shown in Fig. 4.9(a). Fig. 4.9(b,e,h) show the response in the real space for different locations of forces and compression $\eta_x$. Near the onset of instability, i.e., $\eta_x - \eta_{x,cr} = 2 \times 10^{-5}$, the peak between two forces at the origin is pushed down for all three different $\Delta x$. However, as $\eta_x$ increases, the displacements in the real space evolve differently depending on $\Delta x$. Specifically, for bigger separation $\Delta x$ of the force couple, the additional displacement at the peak between two forces changes sign and points upwards.

Decoupled response theory and matrix equations provide a qualitative explanation for this behavior. Near the onset of instability, the amplitude of wrinkles $A_0 \sim \sqrt{\eta_x - \eta_{x,cr}}$ is negligible. Thus, the decoupled response theory of Eq. (4.40b) for the characteristic Fourier mode, which dominates the response, can be rewritten as

$$\delta\tilde{w}_e(k_0) = \frac{B\left((4K_2 + 2hE_0k_0^2)\tilde{f}_{x,o}(k_0)\right)}{4E_0^2K_1(\eta_x - \eta_{x,cr})}. \tag{4.49}$$

When the pair of forces point to each other as shown in the schematic of Fig. 4.9(a), we have $\tilde{f}_{x,o}(k_0) < 0$, therefore, the additional displacement at the peak between two forces points downwards at the onset of instability. However, as $\eta_x$ increases, the negative characteristic mode decays away. Some other non-characteristic modes are positive depending on the compression $\eta_x$ and locations of forces $\Delta x$, as shown in the last two rows of Fig. 4.9 with an excellent agreement between simulation results and predictions of matrix equations. When positive modes dominate, the displacements at the origin become positive.

We systematically studied how the response behavior depends on the locations of horizontal forces and ratios of elastic constants by solving the matrix equations and measuring the additional displacement at the point in the middle of two horizontal forces, as shown in Fig. 4.10. Fig. 4.10(a,e) show the schematic of the force couple

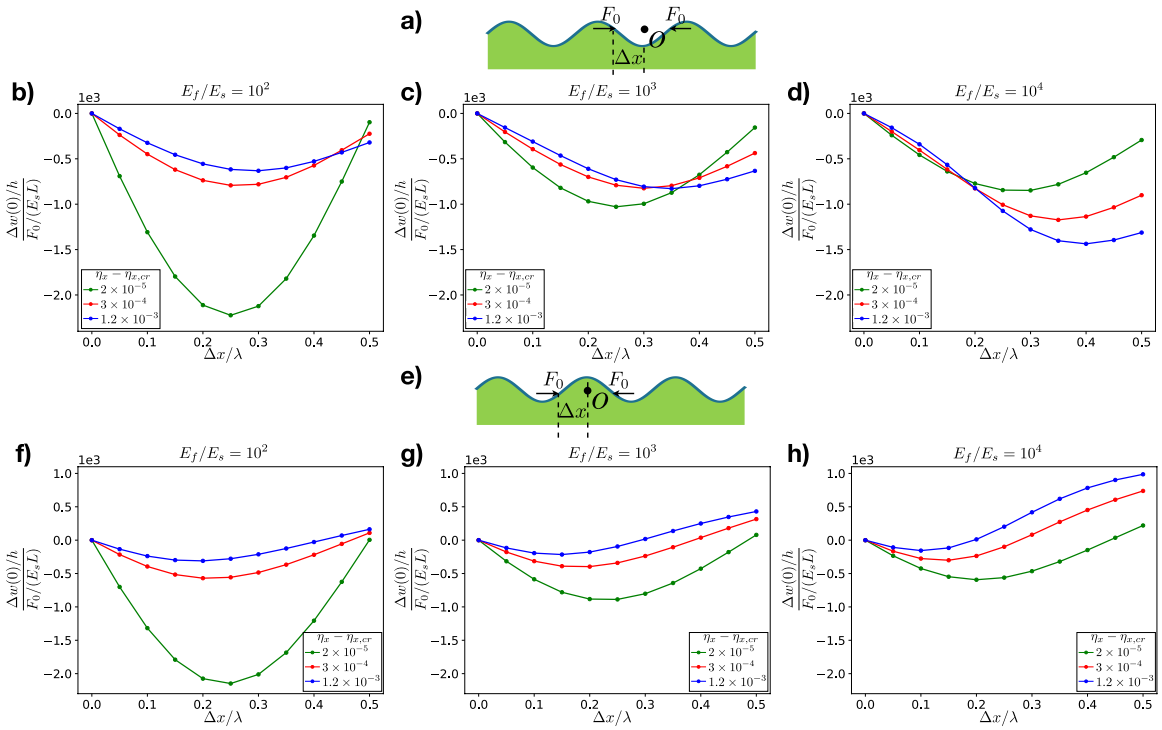


Figure 4.10: Additional displacement at the origin $O$ as a function of locations of forces $\Delta x$, for different ratios of elastic constants and compression $\eta_x$. (a-d) present the additional displacement when two forces are symmetric to the valley. (e-h) present the additional displacement when two forces are symmetric to the peak.

applied to wrinkled structures, where the additional displacement is measured at the origin $O$. Fig. 4.10(a-d) present the response when two forces are symmetric to the valley. When $\eta_x$ is close to $\eta_{x,cr}$, the structures have a maximum response when two forces are separated by $0.5\lambda$, as shown by the green lines in Fig. 4.10(b-d). Besides, the structures with smaller elastic ratios have a larger response since the dominant Fourier mode scales as $\frac{\delta\tilde{w}(k_0)/h}{F_0/(E_s L)} \sim \left(\frac{E_s}{E_f}\right)^{2/3}$, which increases as $E_f/E_s$ decreases. As $\eta_x$ increases above $\eta_{x,cr}$, the characteristic Fourier mode decays. At the same time, the horizontal force has a contribution from the nonlinear coupling term [see Eq. (4.35)] that scales as $\frac{\delta\tilde{w}(qk_0)/h}{F_0/(E_s L)} \sim \left(\frac{E_f}{E_s}\right)^{1/3} \sqrt{\eta_x - \eta_{x,cr}}$ and increases with increasing $\eta_x$ and $E_f/E_s$. The scaling expression can be shown from Eq. (4.40a). Thus, Fig. 4.10(b-d) shows that the response as a function of the locations $\Delta x$ of forces evolves differently with increasing compression $\eta_x$ for different $E_f/E_s$.

Similarly, Fig. 4.10(e-h) shows the response when two forces are symmetric to the peak. When $\eta_x$ is very close to $\eta_{x,cr}$, the structures also have more significant responses when $E_f/E_s$ is smaller. As $\eta_x$ increases, the absolute value of the response decreases. Besides, the response changes from positive to negative for bigger separation $\Delta x$, as shown in Fig. 4.10(g,h).

## 4.5 Conclusion

In this chapter, we have investigated the linear response behavior of wrinkled structures due to infinitesimal point forces in the vertical and horizontal directions. A decoupled Landau-like response theory can adequately describe the response behavior near the instability threshold. The linear response of wrinkled structures diverges at the onset of wrinkling instability due to the divergent Fourier mode that corresponds to the characteristic Fourier mode of wrinkles, which can be understood in analogy with the critical phenomena in ferromagnets. Away from the instability threshold, coupling between different Fourier modes becomes significant. We presented the general formalism of the wrinkling problem in the presence of external forces. We showed that the Landau theory predicts the response well in the regime that $A_0 k_0 \ll 1$ and linearized matrix equations capture the evolution of linear response behavior with increasing compression moderately above the instability threshold.

# Chapter 5

# Conclusion and outlook

## 5.1 Modeling of tissue mechanics with vertex model

In chapter 2, we presented a detailed study of the linear rheological properties of the vertex model for both regular hexagonal and disordered cell configurations over a wide range of driving frequencies. We showed that the linear viscoelastic responses of the vertex model could be mapped to standard spring-dashpot models. When the system is deep in the solid or fluid phases, the spring-dashpot models with a couple of elements are accurate enough to describe the linear viscoelastic properties of the vertex model. However, in the vicinity of solid-fluid transition, the vertex model exhibits a much wider distribution of characteristic time spectrum, which is further discussed in chapter 3 and adequately described by the normal mode theory.

It is important to note that our work focuses on the rheological behavior in the tangent moduli approximation to a general stress-strain curves, where applied shear and bulk deformations are infinitesimal with respect to a potentially significantly predeformed state (e.g., see Fig 2.9). This is clearly an idealized case and, in reality, one would be interested in the response to higher values of the applied deformation ($\gtrsim$

$1-10\%$). It would be possible to study such finite deformations using our simulation protocol. Interpreting the results would, however, be more challenging, e.g., due to shear-driven rigidity transition in model tissues and the presence of plastic events [49, 47].

The vertex model provides a rather coarse description of real epithelial tissues and omits many important aspects such as cell polarization, chemical signalling, cells' ability to actively adjust their properties in response to their environment, etc. The framework presented in this study would, however, be able to address the linear response in the presence of such effects, provided that the vertex model is suitably augmented [133, 134, 128].

A future direction would be to research the role played by the active forces on the rheology of tissues. For example, the remodeling of the actomyosin network along the cell-cell junctions leads to active intercellular stresses. Also, cells are self-propelled due to active cell-substrate traction. Previous studies [24, 135] have shown that activity plays an essential role in the rigidity transition of cell-based models. It would be interesting to study how the viscoelastic properties of these models depend on the activity.

Most existing physical modeling studies for tissue dynamics assumed model parameters are homogeneous across the system or with a simple distribution [136]. With a massive amount of experimental data collected over the years, it would be interesting to study which physical model fits the best and the spatial-temporal distribution of the model parameters for a given experimental system. Recent studies [137] have revealed attractors and repellers of morphogenetic flows using cell-velocity data during the developmental processes, which helps understand the kinematic information. In order to have predictive power, one needs to relate kinematics to thermodynamic forces, i.e., to develop constitutive relations. It would be interesting to develop a physics-based constitutive model bridging from cell scale to

tissue level and unifying experimental measures with the aid of data-driven methods. This physics-based model is expected to be generalizable and provide insights into the properties, including long-time relaxation, that are not experimentally accessible.

## 5.2 Normal mode description of soft matter dynamics

In chapter 3, we demonstrated that the normal mode formalism is a powerful tool to understand the rheology of the vertex model in the overdamped linear response regime. The method developed is general, and can be used to understand many rheological properties of epithelia and other soft matter systems. For example, the relaxation time scales of the system can be understood in terms of the corresponding eigenvalues of the normal modes. Thus the eigenvalue spectrum gives the complete picture of the relaxation properties of the system, even for slow dynamics that are not experimentally accessible.

We studied a few microscopic dissipation mechanisms for the vertex model, which all show good agreement between simulation results and normal mode predictions. Our findings also underscore the importance of microscopic dissipation mechanisms in understanding the rheological behavior of soft materials and tissues. Note that the dissipation matrix $\hat{\boldsymbol{C}}$ contains all the information on how the systems dissipate energy. It would be straightforward to include more realistic dissipation mechanisms in the normal mode approach for the vertex model and other soft matter systems in the future.

We solely focused on the eigenvalue spectrum when we studied the generalized eigenvalue problem in Eq. (3.5). In the future, we could look at how the eigenvalues are correlated with the spatial distribution of their corresponding eigenvectors. For a regular hexagonal configuration, i.e., when the system has discrete transla-

tional symmetry, one could simplify the problem by studying in the reciprocal space. However, disordered systems do not have this advantage. Another point to note is that, in this work, we set the model parameters spatially homogeneous across the systems. In actual epithelial tissues and soft matter systems, heterogeneity is present, which might affect the spatial properties of the eigenvectors of normal modes and, accordingly, the eigenvalue spectrum.

Another interesting direction is to understand how the property of the dissipation matrix $\hat{\boldsymbol{C}}$ perturbs the eigenvalue spectrum of the Hessian matrix $\hat{\boldsymbol{H}}$, thus leading to the solution of the generalized eigenvalue problem in Eq. (3.5). We know that $\hat{\boldsymbol{C}}$ and $\hat{\boldsymbol{H}}$ can be simultaneously diagonalized in the subspace spanned by their shared eigenmodes. However, it is not clear how $\hat{\boldsymbol{C}}$ perturbs $\hat{\boldsymbol{H}}$ outside their shared eigenspace. In the last few decades, the Eigen-spectrum of Hessian has been used to understand the topological states of materials in the absence of dissipation [117]. We do not know much about the role of dissipation in describing the topological properties of materials. Besides, a better understanding of the interaction between $\hat{\boldsymbol{C}}$ and $\hat{\boldsymbol{H}}$ might provide insight into designing a dissipation mechanism to achieve desired rheological properties of materials.

## 5.3 Mechanical response of wrinkled structures

In chapter 4, we studied the linear response property of wrinkled structures. We developed a general formalism of wrinkled structures in the presence of external forces from linear elasticity and Föppl-von Kármán plate theory. In the vicinity of instability, we showed that the general formalism could be simplified to a decoupled response theory, where the divergent response can be understood in terms of the characteristic Fourier modes of wrinkles. Away from the instability threshold, the coupling between Fourier modes becomes significant, which affects the mechanical response.

One future direction is to study the morphogenetic processes of biological systems with multi-layers, where instability occurs during development. Near the instability threshold, these structures become soft because they are more sensitive to external forces. So tiny stimuli are enough to generate wrinkled patterns.

The linear response theory of wrinkled structures can be further used to study the response of wrinkled structures to a more complicated distribution of external forces coming from the environment, such as the interaction of wrinkled structures with liquid droplets. It has been shown by Nagashima et al. [85] that the liquid from the droplet on top of wrinkles can squeeze the wrinkle channels into sharp folds due to the capillary forces if the wetting angle of the liquid droplet is small. This mechanism has been used to produce DNA nanowires by placing a droplet of a liquid solution containing DNA molecules on the wrinkled surface. Since wrinkle-to-fold transition involves large deformation, a precise understanding requires nonlinear continuum mechanics. However, our linear response theory provides a first-step understanding of how horizontal forces coming from the surface tension affect the deformation of wrinkled structures.

# Appendix A

# Additional details of simulations and analysis for Chapter 2

## A.1 The procedure for creating disordered tiling configurations

Fig A.1 shows the procedure to create disordered tiling configurations used to perform rheological simulations.

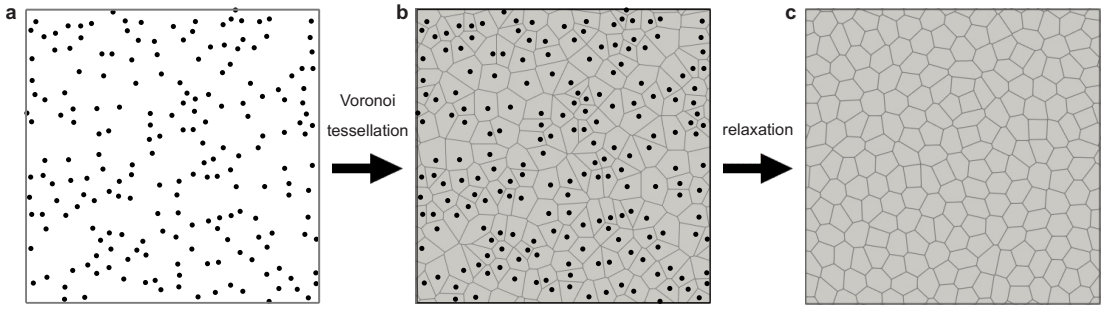


Figure A.1: The procedure of creating disordered tilings of polygons. (a) We first created a random point pattern of $N$ non-overlapping points within a square box. (b) These points are used as seeds for Voronoi tessellation subject to periodic boundary condition. (c) The energy of the system was relaxed to a local energy minimum using the FIRE algorithm.

## A.2 Connection between stress response and rheology

Fig A.2 shows a typical average shear stress $\tau(t)$ in response to an applied oscillatory simple shear with the strain $\epsilon = \epsilon_0 \sin(\omega_0 t)$. The shear stress response can be represented as

$$\tau(t) = \tau_0 \sin(\omega_0 t + \delta) = \tau_0 \cos(\delta) \sin(\omega_0 t) + \tau_0 \sin(\delta) \cos(\omega_0 t). \tag{A.1}$$

The storage shear modulus is related to the in-phase response and is defined as $G' = (\tau_0/\epsilon_0) \cos \delta$. The loss shear modulus is related to the out-of-phase response and is defined as $G'' = (\tau_0/\epsilon_0) \sin \delta$ [107].

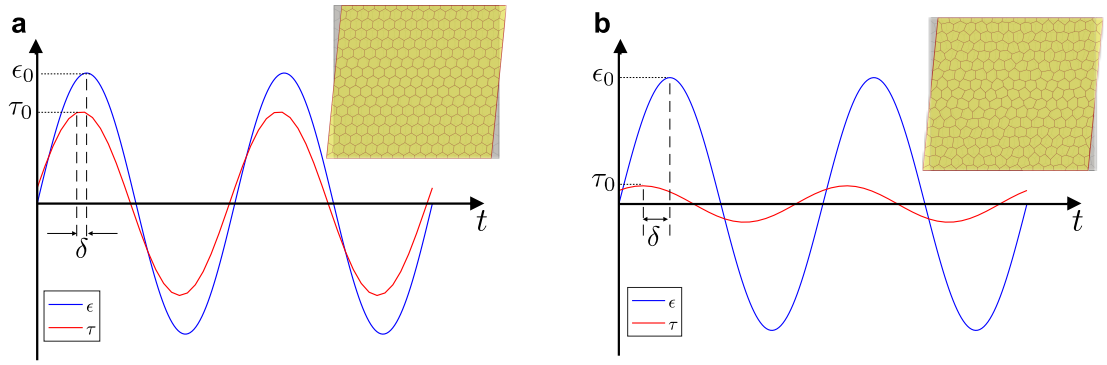


Figure A.2: Typical shear stress (red curve) as a function of time in response to a periodic shear strain (blue curve) in (a) the solid phase and (b) the fluid phase. The shear stress is averaged over all cells.

## A.3 Approach of the response stress towards the steady state

Here, we show an example of how the steady state shear stress $\tilde{\tau}(\omega_0)$ is measured in response to the applied oscillatory simple shear with a time period $T_0$ =

$27.7\gamma/\left(KA_0\right) = 2\pi/\omega_0$ for the shape parameter $p_0 = 3.723$ in hexagonal tiling, which is very close to the critical point $p_c \approx 3.722$ for the solid-fluid transition. The shear stress signal $\tau(t)$ was divided into blocks of length $T = 3T_0$, each containing 3 cycles of the time period of the driving shear deformation (see Fig A.3). Within each block $n$, we performed the Fourier transform of $\tau(t)$ and obtained $\tilde{\tau}_n(\omega)$ as

$$\tilde{\tau}_n(\omega) = \frac{1}{T}\int_{(n-1)T}^{nT} \tau(t)e^{i\omega t}dt, \tag{A.2}$$

where $n$ is a positive integer. The value of $\tilde{\tau}_n(\omega_0)$ converges exponentially to the steady state value (see Fig A.3), where the relaxation time is related to the characteristic timescales of the viscoelastic models (see Fig 3c and 3d in the main text). For values of $p_0$ far away from $p_c$, the system quickly reaches a steady state (within 3–6 cycles). As $p_0$ approaches $p_c$ the relaxation times become much longer, which is reflecting the diverging characteristic timescales of the viscoelastic models (see Fig 3c and 3d in the main text).

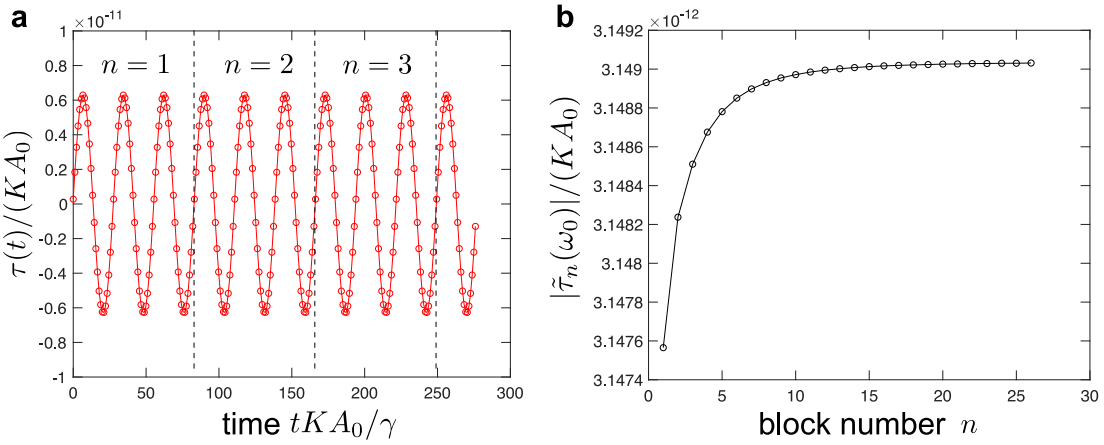


Figure A.3: Approach of the response shear stress towards the steady state. (a) The shear stress signal $\tau(t)$ was divided into blocks indicated by the vertical dashed lines. (b) Fourier transform of the response shear stress $\tilde{\tau}_n(\omega_0)$ at the driving frequency, $\omega_0$, as a function of the block number, $n$.

## A.4 Effect of residual hydrostatic stress on the spring constants in the solid phase for hexagonal tilings

In the solid phase, we studied the rheology of the hexagonal tiling with each cell of area $A_C = A_0$ but with the perimeter $P_C$ unequal to the preferred perimeter $P_0$, which induces residual hydrostatic stress in equilibrium. This residual stress can be eliminated if the lattice is uniformly rescaled by a factor $\alpha$, which minimizes the following dimensionless energy per cell,

$$e_C(\alpha) = \frac{1}{2}\left(\alpha^2 - 1\right)^2 + \frac{\tilde{\Gamma}}{2}\left(\alpha p_C - p_0\right)^2, \tag{A.3}$$

where $e_C = \frac{E_C}{KA_0^2}$, $\tilde{\Gamma} = \frac{\Gamma}{KA_0}$, $p_C = \frac{P_C}{\sqrt{A_0}} = \sqrt[4]{192} \approx 3.722$, i.e., $\alpha$ is the root of equation $e_C'(\alpha) = 0$. In the solid phase, $\alpha < 1$, and the system shrinks to relax the residual stress. At the solid-fluid transition point, $\alpha = 1$ since the area and perimeter of each cell match their preferred values simultaneously. If the residual stress is eliminated by rescaling the box, the rheology of the system subject to a simple shear can still be described by the SLS model, although the fitted values of spring constants are different, as shown in Fig A.4.

## A.5 Collapse of storage and loss shear moduli in the fluid phase for hexagonal tilings

In Fig 2f in the main text, we showed the collapse of storage and loss shear moduli for the fluid phase for hexagonal tilings in the low frequency regime. Here we show the collapse in the high frequency range (see Fig A.5), where we took into account that the relevant characteristic timescale scales as $\eta_2/E_2 \sim \gamma/(KA_0)$.

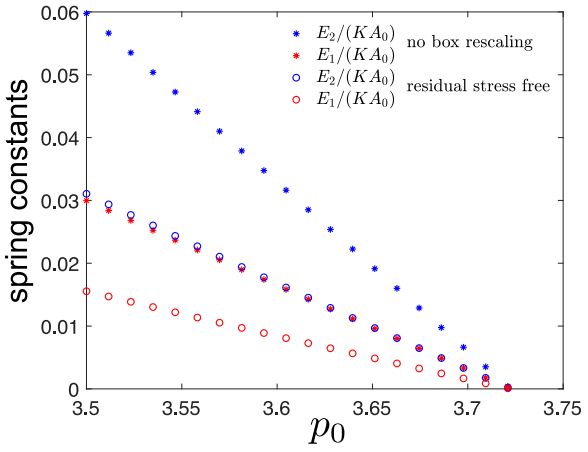


Figure A.4: The fitted spring constants in the solid phase for hexagonal tiling when the simulation box is not rescaled (closed symbols) and rescaled (open symbols) to eliminate residual stresses.

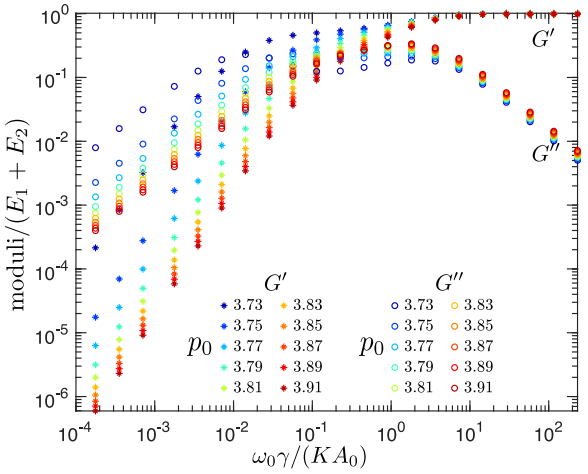


Figure A.5: The collapse of the storage ($G'$) and loss ($G''$) shear moduli curves in the high frequency regime for different values of $p_0$ for the fluid phase.

## A.6 Effects of the initial perturbation of hexagonal tilings on the spring and dashpot constants in the fluid phase

We note that the rheological behavior in the fluid phase for hexagonal tilings is sensitive to the magnitude $\sigma_D$ of the initial perturbation that was used to obtain different local energy minima configurations. In the main text, we showed the fitted values of spring and dashpot constants (Fig 3) for the local energy minima configurations that were obtained by displacing each vertex coordinate of the hexagonal tiling by a Gaussian random variable with zero mean and standard deviation $\sigma_D = 1.5 \times 10^{-4}\sqrt{A_0}$. Here, we show that the fitted values of the spring and dashpot constants are somewhat sensitive to the magnitude $\sigma_D$ of the random perturbation (see Fig A.6).

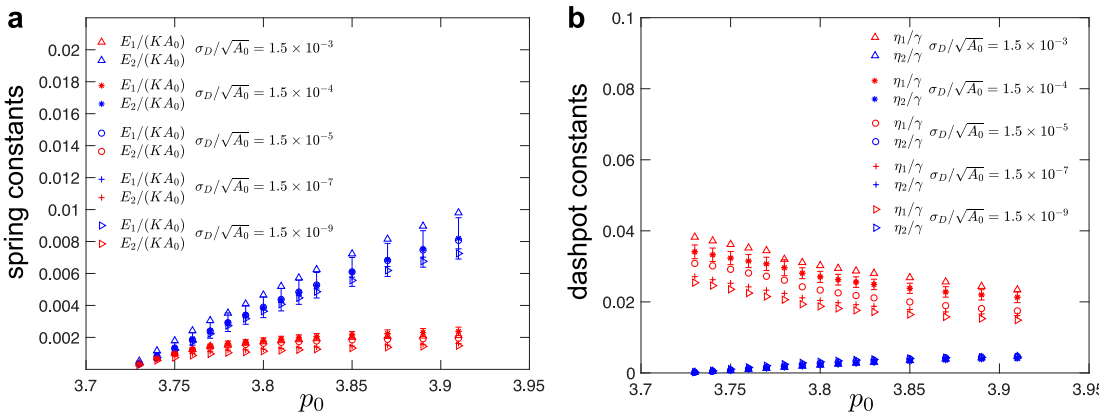


Figure A.6: Fitted values of (a) spring and (b) dashpot constants for hexagonal tilings under simple shear deformation as a function of the target cell-shape parameter, $p_0$, and the magnitude $\sigma_D$ of the random perturbation that was used to obtain different local energy minima configurations in the fluid phase. Errorbars correspond to the standard deviation for simulations with $\sigma_D = 1.5 \times 10^{-4}\sqrt{A_0}$ that were repeated for configurations that correspond to different local energy minima.

## A.7 Tuning phase transition with different modes of pre-deformation.

In the main text, we showed that the solid-fluid transition point for hexagonal tilings can be tuned by uniaxially pre-compressing/stretching the system. Here, we discuss other pre-deformation modes that can also tune the transition.

We first derive the shear modulus due to affine deformation following a similar formalism as in Ref. [89]. There are two equivalent ways of derivation. The first one is to calculate the energy density of the system perturbed by an additional simple shear $\hat{\boldsymbol{F}} = \left(\begin{smallmatrix} 1 & \epsilon \\ 0 & 1 \end{smallmatrix}\right)$ where $\epsilon \ll 1$. For example, for the hexagonal tiling without any pre-deformation (i.e., regular hexagons), one can first calculate the vertex positions of a regular hexagon after being deformed by the affine transformation $\hat{\boldsymbol{F}}$. Then the perimeter of the deformed hexagon can be derived as

$$\frac{P}{6L_0} = 1 + \frac{3}{16}\epsilon^2 + o\left(\epsilon^4\right) \tag{A.4}$$

where $L_0 = \sqrt{2A_0}/\sqrt{3\sqrt{3}}$ is the edge length of a regular hexagon before deformation. The area of the hexagon does not change after the simple shear deformation. With the knowledge of the perimeter and area of the deformed hexagon, one can calculate and expand the energy density from Eq. (1) in a power series in $\epsilon$ as

$$\frac{E}{NA_0} = \frac{1}{2}3\sqrt{3}\Gamma\left(1 - \frac{p_0}{\sqrt{8\sqrt{3}}}\right)\epsilon^2 + o\left(\epsilon^4\right) \equiv \frac{1}{2}G_{\text{affine}}\epsilon^2 + o\left(\epsilon^4\right), \tag{A.5}$$

where we omitted the constant term. The quadratic term characterizes the linear response of the system, which gives the shear modulus as in Eq. (7) in the main text. The second approach is to directly use the expression for the stress tensor Eq. (3). After obtaining the vertex positions of a hexagon perturbed by a simple shear $\hat{\boldsymbol{F}}$, one can calculate the shear stress and expand in a power series as $\tau = \hat{\sigma}_{xy} = G_{\text{affine}}\epsilon + o\left(\epsilon^2\right)$.

The coefficient of the leading order term in $\epsilon$ is the shear modulus, which coincides with the modulus from the energy calculation. Similar derivation of the shear modulus can be carried out for the pre-deformed hexagonal tilings.

If the hexagonal tiling is pre-deformed biaxially according to the deformation gradient $\hat{\boldsymbol{F}} = \left(\begin{smallmatrix} a & 0 \\ 0 & a \end{smallmatrix}\right)$, then the shear modulus due to the affine deformation becomes

$$G_{\text{affine}} = 3\sqrt{3}\Gamma\left(1 - \frac{p_0}{a\sqrt{8\sqrt{3}}}\right). \tag{A.6}$$

By setting $G_{\text{affine}}$ to 0, the phase boundary in the $a - p_0$ plane is

$$p_c(a) = a\sqrt{8\sqrt{3}}. \tag{A.7}$$

Similarly, consider a pure shear pre-deformation described by the deformation gradient $\hat{\boldsymbol{F}} = \left(\begin{smallmatrix} a & 0 \\ 0 & 1/a \end{smallmatrix}\right)$. The shear modulus due to the affine deformation then becomes

$$G_{\text{affine}} = \frac{2\sqrt{2}\left(1 + \sqrt{1+3a^4} + 3a^4\sqrt{1+3a^4}\right)\left(2\sqrt{2}\ 3^{1/4}(1+\sqrt{1+3a^4}) - 3ap_0\right)\Gamma}{3^{7/4}a(1+3a^4)^{3/2}}, \tag{A.8}$$

and the phase boundary is

$$p_c(a) = \sqrt{8\sqrt{3}}\ \frac{(1+\sqrt{1+3a^4})}{3a}. \tag{A.9}$$

The phase diagrams for a hexagonal tiling that is under biaxial or pure shear pre-deformation are shown in Fig A.7. The phase boundary in the $a - p_0$ plane follows Eq. (A.7) for biaxial pre-deformation and Eq. (A.9) for pure shear pre-deformation. The system can be rigidified by stretching or shearing.

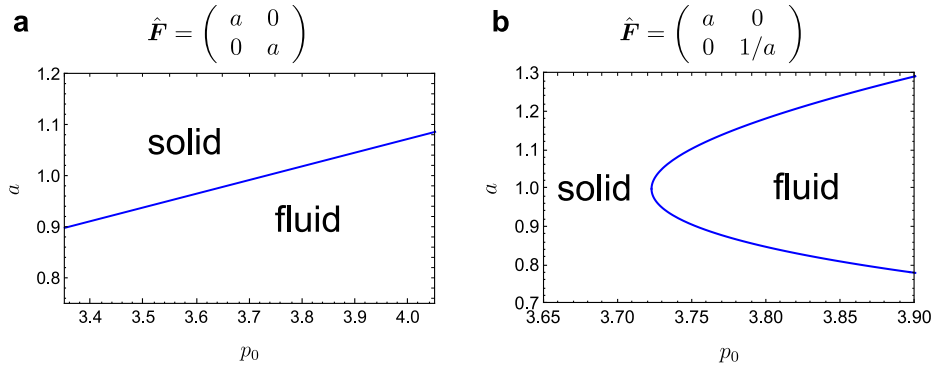


Figure A.7: Phase diagrams when the system is under (a) biaxial deformation and (b) pure shear.

## A.8 Spectrum of the normal modes for hexagonal tilings

We calculated the eigenvalues $\lambda$ of the Hessian matrix $\frac{\partial^2 E}{\partial \mathbf{r}_i \partial \mathbf{r}_j}$ associated with the energy functional of the vertex model for hexagonal tiling. We associate each positive eigenvalue $\lambda$ with a corresponding eigenfrequency $\omega = \sqrt{\lambda}$, which describes the oscillations of that mode as the system is perturbed about its stable point. Fig A.8 shows the cumulative density of states, which is defined as [23]

$$N(\omega) = \int_{0^+}^{\infty} D(\omega')d\omega' + N(\lambda = 0)\theta(\omega), \tag{A.10}$$

where $D(\omega)$ is density of states, $N(\lambda = 0)$ is the fraction of zero eigenvalues and $\theta(\omega)$ is the Heaviside step function. In the solid phase, there are no zero modes other than the two translational rigid body motions. In the fluid phase, however, approximately half of the eigenmodes are zero modes. As $p_0$ approaches the critical value $p_c$ in both solid and fluid phase, $N(\omega)$ curves move to the left so the system becomes softer, which is consistent with the dependence of the spring constants on $p_0$ shown in Fig 3a in the main text.

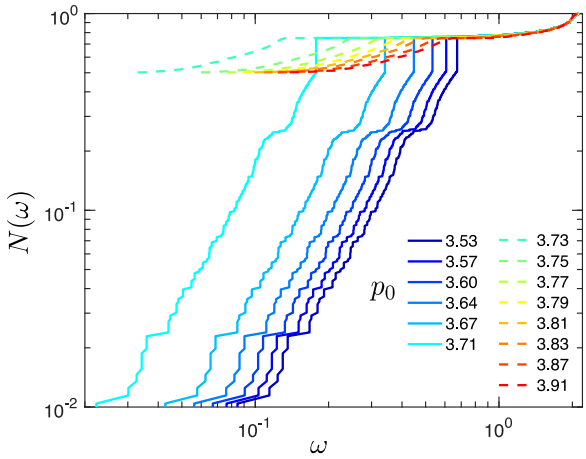


Figure A.8: Cumulative density of states in the solid phase (solid lines) and in the fluid phase (dashed lines) for hexagonal tilings.

## A.9 Raw data of storage and loss shear moduli for disordered tilings

Fig A.9 shows the raw data of storage and loss shear moduli for disordered tilings for a range of values of $p_0$. Each color represents the storage and loss shear moduli for one disordered tiling configuration. These data are used to calculate the average storage and loss shear moduli for each value of $p_0$. From the raw data one can see large variability in storage and loss moduli when $p_0$ is close to the critical value of the solid-fluid transition. When $p_0 = 3.93$ and $p_0 = 3.95$, there is a mixture of solid and fluid configurations since some storage moduli plateau at a nonzero constant value and some vanish in the low frequency limit.

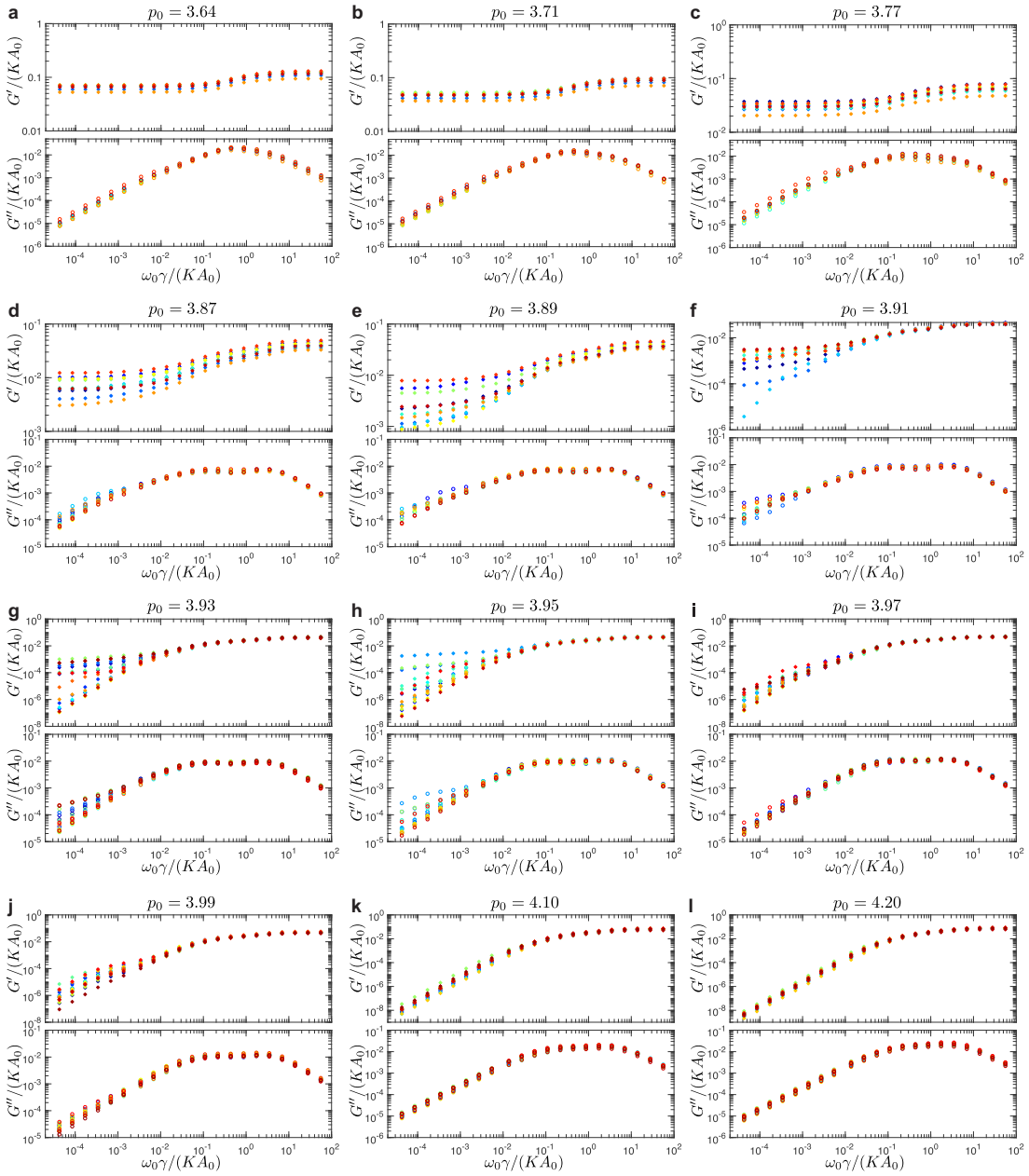


Figure A.9: Raw data of storage ($G'$) and loss ($G''$) shear moduli for disordered tilings. The variability in storage and loss moduli increases as $p_0$ approaches the critical value of the solid-fluid transition.

## A.10 Raw data of storage and loss bulk moduli for disordered tilings

Fig A.10 shows the raw data of storage and loss bulk moduli for disordered tilings at a few representative values of $p_0$. The storage and loss moduli have high variability when $p_0$ is close to the critical value of solid-fluid transition ($p_0 = 3.93$).

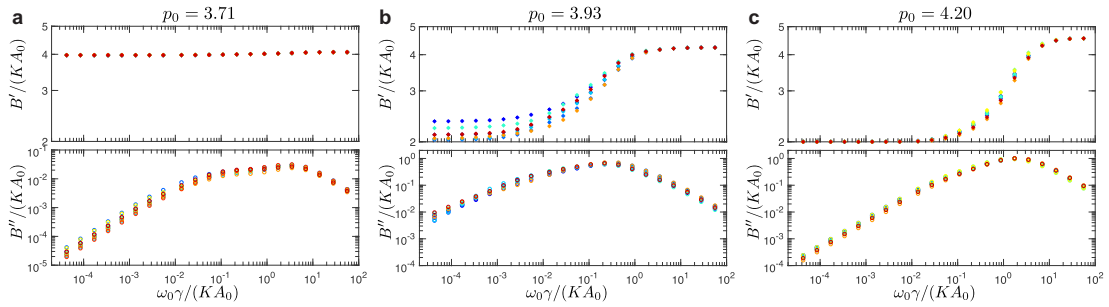


Figure A.10: Raw data of storage ($B'$) and loss ($B''$) bulk moduli for disordered tilings.

## A.11 Comparison of fits of shear moduli based on different spring-dashpot models for disordered tilings

Fig A.11 shows the fits of average storage and loss shear moduli based on different spring-dashpot models for disordered tilings at $p_0 = 3.71$. Adding more Maxwell elements in parallel to the Standard Linear Solid model increases the accuracy of fits. In Fig A.11 with the most accurate fit presented here, however, the fitted curve of loss modulus goes up and down through the simulation curve. This manifests the characteristic of fit with high order polynomials and indicates that addition of more Maxwell elements does not fully capture the behavior of the shear moduli obtained from the simulations.

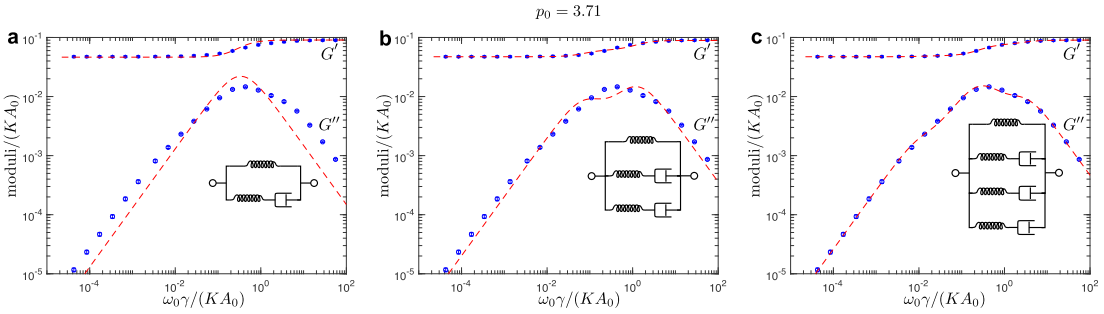


Figure A.11: Fits of average shear moduli based on different spring-dashpot models for disordered tilings at $p_0 = 3.71$. Red dashed lines are the fits. Blue dots represent the moduli data obtained from the simulations. (a) shows the fits based on the Standard Linear Solid (SLS) model. The fits in (b) and (c) are based on spring-dashpot models with additional Maxwell elements in parallel to the SLS model. The insets of each plot show the representation of the corresponding spring-dashpot models.

## A.12 System size effect for disordered tilings

Fig A.12 shows the storage and loss shear moduli for disordered tilings of different sizes at $p_0 = 3.71$. The system sizes have no effect at high frequency of shearing. At intermediate frequency, the loss modulus has an anomalous scaling exponent, i.e., $\sim \omega_0^\alpha$ with $\alpha \approx 0.73$, which changes from being linear in low frequency. This crossover moves to lower frequencies as the system size increases.

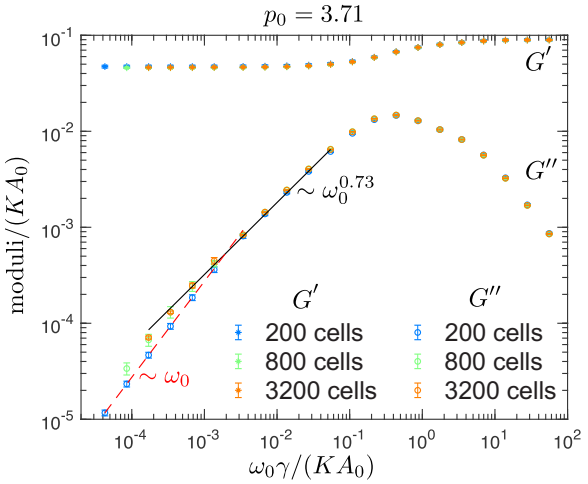


Figure A.12: Storage and loss shear moduli for disordered tilings of different system sizes at $p_0 = 3.71$.

# Appendix B

# Calculation of forces, Hessian matrix, and stresses in the vertex model

## B.1 Elastic force on a vertex

In this appendix, we outline the derivation of the expression for the elastic force $\mathbf{f}_i^{\mathrm{e}}$ on a vertex $i$. The elastic force on vertex $i$ is

$$\mathbf{f}_i^{\mathrm{e}} = -\nabla_{\mathbf{R}_i} E, \tag{B.1}$$

where

$$E = \sum_C \left[ \frac{K}{2} \left( A_C - A_0 \right)^2 + \frac{\Gamma}{2} \left( P_C - P_0 \right)^2 \right] \tag{B.2}$$

is the energy function of the vertex model. In these appendices, we use Latin subscript indices to denote different vertices and cells, and Greek superscript indices to denote $x$ and $y$ components of a vector.

The area of the cell $C$ can be expressed as

$$\begin{aligned} A_C &= \frac{1}{2}\sum_{i\in C}\left(\mathbf{R}_i \times \mathbf{R}_{i+1}\right)\cdot \mathbf{e}_z, \\ A_C &= \frac{1}{2}\sum_{i\in C}\varepsilon_{\alpha\beta} R_i^{\alpha} R_{i+1}^{\beta}. \end{aligned} \tag{B.3}$$

In the above equations, the summation is over all vertices $i$ that belong to cell $C$. Vertices $i$ are assumed to be labeled from 0 to $N_C - 1$ in a counterclockwise sense and the index $i+1$ is calculated modulo $N_C$, i.e., for $i = N_C - 1$ the value of $i+1$ is 0. In Eq. (B.3), the $\mathbf{R}_i$ is the position vector of vertex $i$, $\mathbf{e}_z$ is the unit-length vector perpendicular to the plane of the tissue (assumed to be the $xy-$plane), $\varepsilon_{\alpha\beta}$ is the two-dimensional Levi-Civita symbol, and summation over repeated Greek indices is implied. Similarly, the perimeter of the cell $C$ is

$$\begin{aligned} P_C &= \sum_{i\in C}\left|\mathbf{R}_{i+1} - \mathbf{R}_i\right| \\ &= \sum_{i\in C}\left[\left(R_{i+1}^{\alpha} - R_i^{\alpha}\right)\left(R_{i+1}^{\alpha} - R_i^{\alpha}\right)\right]^{1/2}, \end{aligned} \tag{B.4}$$

with the same rules as in the case of the area term in Eq. (B.3).

The elastic force on vertex $i$ is then

$$\begin{aligned} \mathbf{f}_i^{\mathrm{e}} &= -\sum_{C\in\mathcal{N}_i}\Big[K\left(A_C - A_0\right)\left(\nabla_{\mathbf{R}_i} A_C\right) \\ &\qquad + \Gamma\left(P_C - P_0\right)\left(\nabla_{\mathbf{R}_i} P_C\right)\Big], \\ \mathbf{f}_i^{\mathrm{e}} &\equiv \sum_{C\in\mathcal{N}_i}\mathbf{f}_{C\to i}^{\mathrm{e}} \end{aligned} \tag{B.5}$$

where $\mathcal{N}_i$ includes the set of all cells that share vertex $i$ and we defined $\mathbf{f}_{C\to i}^{\mathrm{e}}$ as the elastic force contribution on the vertex $i$ due to cell $C$.

It is straightforward to show that for the vertex $i$ that belongs to cell $C$ the derivatives are

$$\begin{aligned}
\nabla_{\mathbf{R}_i} A_C &= \frac{1}{2}\delta_{C,i}\left(\mathbf{R}_{i+1} - \mathbf{R}_{i-1}\right) \times \mathbf{e}_z, \\
\frac{\partial A_C}{\partial R_i^\alpha} &= \frac{1}{2}\delta_{C,i}\varepsilon_{\alpha\beta}\left(R_{i+1}^\beta - R_{i-1}^\beta\right), \\
\frac{\partial A_C}{\partial R_i^\alpha} &= \frac{1}{2}\delta_{C,i}\varepsilon_{\alpha\beta}\left(l_{i,i+1}^\beta - l_{i,i-1}^\beta\right),
\end{aligned} \tag{B.6}$$

and

$$\begin{aligned}
\nabla_{\mathbf{R}_i} P_C &= \delta_{C,i}\left(\frac{\mathbf{R}_i - \mathbf{R}_{i-1}}{|\mathbf{R}_i - \mathbf{R}_{i-1}|} - \frac{\mathbf{R}_{i+1} - \mathbf{R}_i}{|\mathbf{R}_{i+1} - \mathbf{R}_i|}\right), \\
\frac{\partial P_C}{\partial R_i^\alpha} &= \delta_{C,i}\left(\frac{R_i^\alpha - R_{i-1}^\alpha}{|\mathbf{R}_i - \mathbf{R}_{i-1}|} - \frac{R_{i+1}^\alpha - R_i^\alpha}{|\mathbf{R}_{i+1} - \mathbf{R}_i|}\right), \\
\frac{\partial P_C}{\partial R_i^\alpha} &= -\delta_{C,i}\left(\hat{l}_{i,i-1}^\alpha + \hat{l}_{i,i+1}^\alpha\right),
\end{aligned} \tag{B.7}$$

where we introduced the vector $\mathbf{l}_{i,j} = \mathbf{R}_j - \mathbf{R}_i$ along the junction connecting vertices $i$ and $j$, normalized unit vector $\hat{\mathbf{l}} = \mathbf{l}/|\mathbf{l}|$, and

$$\delta_{C,i} = \begin{cases} 1 & \text{if vertex } i \text{ belongs to cell } C \\ 0 & \text{otherwise} \end{cases}. \tag{B.8}$$

The elastic force contribution $\mathbf{f}_{C\to i}^{\mathrm{e}}$ on the vertex $i$ due to cell $C$ can thus be expressed as

$$\begin{aligned}
\mathbf{f}_{C\to i}^{\mathrm{e}} &= -\frac{1}{2}\delta_{C,i}\, K\left(A_C - A_0\right)\left(\mathbf{l}_{i,i+1} - \mathbf{l}_{i,i-1}\right) \times \mathbf{e}_z \\
&\quad + \delta_{C,i}\,\Gamma\left(P_C - P_0\right)\left(\hat{\mathbf{l}}_{i,i-1} + \hat{\mathbf{l}}_{i,i+1}\right)
\end{aligned} \tag{B.9}$$

Note that the derivatives $\nabla_{\mathbf{R}_i} A_C$ and $\nabla_{\mathbf{R}_i} P_C$ only depend on the lengths and orientations of cell-cell junctions that contain vertex $i$ [see Eqs. (B.6) and (B.7)].

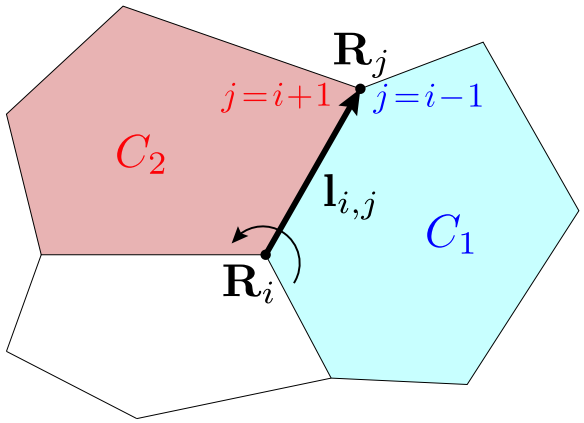


Figure B.1: An efficient way of calculating the elastic force on vertex $i$, $\mathbf{f}_i^{\mathrm{e}}$, is to loop over all cell-cell junctions that originate at $i$ in the counterclockwise direction. For each junction, the two cells that share it contribute to the total force. These contributions are the two terms in the sum in Eq. (B.10). For consistency, we adopt a convention that when looking along the junction away from the vertex $i$, the cell to the right (blue) is labeled as $C_1$, and the cell to the left (red) is labeled as $C_2$. Note that since vertices within each cell are ordered counterclockwise, the endpoint of the junction, i.e., the vertex $j$ appears in cell 1 (2) as $i-1$ ($i+1$) in the cell's internal labeling.

Thus the elastic force $\mathbf{f}_i^{\mathrm{e}}$ can also be expressed as a summation over the cell-cell junctions as

$$\begin{aligned} \mathbf{f}_i^{\mathrm{e}} = &+ \sum_{j\in\mathcal{S}_i} \frac{1}{2} K \left(A_{C_1(j)} - A_{C_2(j)}\right) \mathbf{l}_{i,j} \times \mathbf{e}_z \\ &+ \sum_{j\in\mathcal{S}_i} \Gamma \left(\Delta P_{C_1(j)} + \Delta P_{C_2(j)}\right) \hat{\mathbf{l}}_{i,j}, \end{aligned} \tag{B.10}$$

where $\Delta P_C = (P_C - P_0)$. The set $\mathcal{S}_i$ contains all vertices, $j$, connected by cell-cell junctions to the vertex $i$. Here, we adopt a convention that when looking along the junction away from the vertex $i$, the cells to the right and left are labeled as $C_1(j)$ and $C_2(j)$, respectively (see Fig. B.1). In the numerical implementation, we calculated the elastic force $\mathbf{f}_i^{\mathrm{e}}$ using Eq. (B.10) because we can efficiently loop over all cell-cell junctions that belong to the vertex $i$.

## B.2 Hessian matrix of the vertex model

In this appendix, we outline the derivation of the expressions for the Hessian matrix of the vertex model. To allow for the most general case, we express the energy of the vertex model as

$$E = \sum_C \frac{K_C}{2}\left(A_C - A_0^C\right)^2 + \sum_C \frac{\Gamma_C}{2} P_C^2 - \sum_{\langle i,j\rangle} \Lambda_{ij} |\mathbf{l}_{i,j}|, \tag{B.11}$$

where $\Lambda_{ij}$ is the line tension and $|\mathbf{l}_{i,j}| \equiv |\mathbf{R}_j - \mathbf{R}_i|$ is the length of the junction connecting vertices $i$ and $j$. The summation $\langle i,j\rangle$ is over all pairs of vertices $i$ and $j$ connected by junctions. In the case when parameters $K_C$, $\Gamma_C$, $A_0^C$, $P_0^C$ and $\Lambda_{ij}$ are not cell-specific, one immediately reads off $P_0 = \frac{\Lambda}{\Gamma}$ and, after adding the constant term $\frac{1}{2}\Gamma P_0^2$, readily recovers Eq. (3.22). Since in general scenarios the line tension can vary across junctions, we will use Eq. (B.11) as the expression for the energy of the vertex model for further derivation.

For a system with $N$ vertices, the Hessian of the vertex model is a real symmetric matrix of size $2N \times 2N$. Its elements are

$$\hat{H}_{IJ} = \frac{\partial^2 E}{\partial x_I \partial x_J}\Big|_{\mathbf{r}=\mathbf{r}^{\mathrm{eq}}}, \tag{B.12}$$

where $I, J \in \{1, \ldots, 2N\}$, and $I = 2(i-1) + \alpha$, with $i \in \{1, \ldots, N\}$ and $\alpha \in \{1, 2\}$. In other words, for $I = 2i - 1$, $x_I \equiv R_i^x$ and for $I = 2i$, $x_I \equiv R_i^y$. Identical relations hold for index $J$. Elements of the Hessian matrix are calculated for a configuration in mechanical equilibrium, i.e., for $\mathbf{r} = \mathbf{r}^{\mathrm{eq}}$. One finds,

$$\begin{aligned}\frac{\partial^2 E}{\partial R_k^\alpha \partial R_m^\beta} &= \sum_C K_C \left[\frac{\partial A_C}{\partial R_k^\alpha}\frac{\partial A_C}{\partial R_m^\beta} + \left(A_C - A_0^C\right)\frac{\partial^2 A_C}{\partial R_k^\alpha \partial R_m^\beta}\right] \\ &\quad + \sum_C \Gamma_C \left[\frac{\partial P_C}{\partial R_k^\alpha}\frac{\partial P_C}{\partial R_m^\beta} + \sum_C \Gamma_C P_C \frac{\partial^2 P_C}{\partial R_k^\alpha \partial R_m^\beta}\right]\end{aligned}$$

$$-\sum_{\langle i,j\rangle}\Lambda_{ij}\frac{\partial^2|\mathbf{l}_{i,j}|}{\partial R_k^\alpha \partial R_m^\beta}. \tag{B.13}$$

The expression for $\partial A_C/\partial R_k^\alpha$ and $\partial P_C/\partial R_k^\alpha$ are given in Eqs. (B.6) and (B.7), respectively. It is straightforward to show that

$$\frac{\partial^2 A_C}{\partial R_k^\alpha \partial R_m^\beta} = \frac{1}{2}\delta_{C,k}\delta_{C,m}\varepsilon_{\alpha\beta}\left(\delta_{m-1,k}-\delta_{m+1,k}\right), \tag{B.14}$$

where

$$\delta_{i,j} = \begin{cases} 1 \text{ if } i=j \\ 0 \text{ if } i\neq j \end{cases} \tag{B.15}$$

is the Kronecker delta. Similarly,

$$\begin{aligned}\frac{\partial^2 P_C}{\partial R_k^\alpha \partial R_m^\beta} &= -\delta_{C,k}\delta_{C,m}\left(\delta_{m,k}-\delta_{m-1,k}\right)\left[\frac{l_{m-1,m}^\alpha l_{m-1,m}^\beta}{|\mathbf{l}_{m-1,m}|^3}-\frac{\delta_{\alpha\beta}}{|\mathbf{l}_{m-1,m}|}\right] \\ &\quad +\delta_{C,k}\delta_{C,m}\left(\delta_{m+1,k}-\delta_{m,k}\right)\left[\frac{l_{m,m+1}^\alpha l_{m,m+1}^\beta}{|\mathbf{l}_{m,m+1}|^3}-\frac{\delta_{\alpha\beta}}{|\mathbf{l}_{m,m+1}|}\right].\end{aligned} \tag{B.16}$$

Finally,

$$\begin{aligned}\frac{\partial^2|\mathbf{l}_{i,j}|}{\partial R_k^\alpha \partial R_m^\beta} &= -\left(\delta_{i,k}-\delta_{j,k}\right)\left(\delta_{i,m}-\delta_{j,m}\right)\left[\frac{\left(R_j^\alpha-R_i^\alpha\right)\left(R_j^\beta-R_i^\beta\right)}{|\mathbf{R}_j-\mathbf{R}_i|^3}-\frac{\delta_{\alpha\beta}}{|\mathbf{R}_j-\mathbf{R}_i|}\right], \\ \frac{\partial^2|\mathbf{l}_{i,j}|}{\partial R_k^\alpha \partial R_m^\beta} &= -\left(\delta_{i,k}-\delta_{j,k}\right)\left(\delta_{i,m}-\delta_{j,m}\right)\left[\frac{l_{i,j}^\alpha l_{i,j}^\beta}{|\mathbf{l}_{i,j}|^3}-\frac{\delta_{\alpha\beta}}{|\mathbf{l}_{i,j}|}\right].\end{aligned} \tag{B.17}$$

## B.3 External driving force due to shear of the periodic simulation box in the vertex model

In this appendix, we outline the derivation of the expression for the external driving force $\bar{\mathbf{f}}^{\mathrm{pb}}$ due to the shear of the rectangular periodic simulation box with edge lengths

$\ell_x$ and $\ell_y$. We use the energy function for the vertex model given in Eq. (B.11) and seek to find the expression for

$$\bar{f}_I^{\rm pb} = -\frac{\partial^2 E}{\partial x_I \partial \epsilon}\Big|_{\mathbf{r}=\mathbf{r}^{\rm eq},\epsilon=0}, \tag{B.18}$$

where $\epsilon$ measures the shear of the simulation box, and as in Eq. (B.12), $I \in \{1,\ldots,2N\}$ labels vertex coordinates. Similar to the derivation of the Hessian matrix given in Appendix B.2, one finds

$$\begin{aligned}\frac{\partial^2 E}{\partial R_k^\alpha \partial \epsilon} &= \sum_C K_C \left[\frac{\partial A_C}{\partial R_k^\alpha}\frac{\partial A_C}{\partial \epsilon} + \left(A_C - A_0^C\right)\frac{\partial^2 A_C}{\partial R_k^\alpha \partial \epsilon}\right] \\ &\quad + \sum_C \Gamma_C \left[\frac{\partial P_C}{\partial R_k^\alpha}\frac{\partial P_C}{\partial \epsilon} + P_C \frac{\partial^2 P_C}{\partial R_k^\alpha \partial \epsilon}\right] \\ &\quad - \sum_{\langle i,j\rangle} \Lambda_{ij} \frac{\partial^2 |\mathbf{l}_{i,j}|}{\partial R_k^\alpha \partial \epsilon},\end{aligned} \tag{B.19}$$

with the same meaning of the summation indices. Note that the shear degree of freedom $\epsilon$ appears only for cell junctions that cross the periodic boundary. The energy of the vertex model depends on $\epsilon$ through the $x$-component of the distance vectors,

$$l_{m,n}^x = R_n^x - R_m^x + q_{m,n}^x \ell_x + \epsilon q_{m,n}^y \ell_y, \tag{B.20}$$

where [32]

$$q_{m,n}^x = \begin{cases} 0 & \text{if the junction connecting vertices } m \text{ and } n \text{ does not cross} \\ & \text{the right or left boundaries} \\ +1\,(-1) & \text{if the junction connecting vertices } m \text{ and } n \text{ crosses the right} \\ & \text{(left) boundary} \end{cases}, \tag{B.21a}$$

$$q^y_{m,n} = \begin{cases} 0 & \text{if the junction connecting vertices } m \text{ and } n \text{ does not cross the top or bottom boundaries} \\ +1\,(-1) & \text{if the junction connecting vertices } m \text{ and crosses the top (bottom) boundary} \end{cases}. \tag{B.21b}$$

Using the chain rule, the derivative with respect to $\epsilon$ is

$$\frac{\partial}{\partial \epsilon} = \sum_{\langle m,n \rangle} \frac{\partial l^x_{m,n}}{\partial \epsilon} \frac{\partial}{\partial l^x_{m,n}} = \sum_{\langle m,n \rangle} q^y_{m,n} \ell_y \frac{\partial}{\partial l^x_{m,n}}. \tag{B.22}$$

Using Eqs. (B.6) and (B.7) and the chain rule in Eq. (B.22), one can show that

$$\frac{\partial^2 A_C}{\partial R^\alpha_k \partial \epsilon} = \sum_{\langle m,n \rangle \in C} \frac{1}{2} \delta_{C,k} q^y_{m,n} \ell_y \varepsilon_{\alpha x} (\delta_{m,k}\delta_{n,k+1} + \delta_{m,k-1}\delta_{n,k}), \tag{B.23}$$

and

$$\frac{\partial^2 P_C}{\partial R^\alpha_k \partial \epsilon} = -\sum_{\langle m,n \rangle \in C} \delta_{C,k} q^y_{m,n} \ell_y \quad \left[ \delta_{m,k-1}\delta_{n,k} \left( \frac{l^\alpha_{k-1,k} l^x_{k-1,k}}{|\mathbf{l}_{k-1,k}|^3} - \frac{\delta_{\alpha,x}}{|\mathbf{l}_{k-1,k}|} \right) \right.$$
$$\left. -\delta_{m,k}\delta_{n,k+1} \left( \frac{l^\alpha_{k,k+1} l^x_{k,k+1}}{|\mathbf{l}_{k,k+1}|^3} - \frac{\delta_{\alpha,x}}{|\mathbf{l}_{k,k+1}|} \right) \right], \tag{B.24}$$

where the summation is restricted over all junctions $\langle m, n \rangle$ that belong to cell $C$. Similarly, one can find that

$$\frac{\partial^2 |\mathbf{l}_{i,j}|}{\partial R^\alpha_k \partial \epsilon} = -q^y_{i,j} \ell_y \left(\delta_{j,k} - \delta_{i,k}\right) \left( \frac{l^\alpha_{i,j} l^x_{i,j}}{l^3_{i,j}} - \frac{\delta_{\alpha,x}}{l_{ij}} \right). \tag{B.25}$$

## B.4 Stress tensor for each cell in the Vertex Model

In this appendix, we provide a detailed derivation of the expression for the stress tensor $\hat{\boldsymbol{\sigma}}_C$ for cell $C$ in the vertex model. Note that the derivation follows the steps

introduced in Ref. [106], and we further emphasize the difference between internal and external forces to demonstrate that the internal dissipation forces directly produce stresses, while the external dissipation forces produce stresses indirectly via the force balance with internal forces.

In the continuum limit, the mechanical equilibrium can be expressed as $\nabla \cdot \hat{\boldsymbol{\sigma}} + \mathbf{f}^{\text{ext}} = 0$, where $\hat{\boldsymbol{\sigma}}(\mathbf{R})$ is the symmetric stress tensor, $\mathbf{f}^{\text{ext}}(\mathbf{R})$ is the external force applied to the system, and $\mathbf{R}$ is a position vector. Note that the vertex model with overdamped dynamics is considered to be in a quasi-mechanical equilibrium. For a system that is in mechanical equilibrium, we also have $\hat{\boldsymbol{\sigma}} = \nabla \cdot (\mathbf{R} \otimes \hat{\boldsymbol{\sigma}}) + \mathbf{R} \otimes \mathbf{f}^{\text{ext}}$, where $\otimes$ represents the tensor product. By integrating this relation over an arbitrary area element we obtain

$$\begin{aligned}
\int_A dA\, \hat{\boldsymbol{\sigma}} &= \int_A dA\, \left( \nabla \cdot (\mathbf{R} \otimes \hat{\boldsymbol{\sigma}}) + \mathbf{R} \otimes \mathbf{f}^{\text{ext}} \right), \\
\int_A dA\, \hat{\boldsymbol{\sigma}} &= \int_{\partial A} ds\, \mathbf{R} \otimes (\hat{\boldsymbol{\sigma}} \cdot \hat{\mathbf{n}}) + \int_A dA\, \mathbf{R} \otimes \mathbf{f}^{\text{ext}}, \\
\int_A dA\, \hat{\boldsymbol{\sigma}} &= \int_{\partial A} ds\, \mathbf{R} \otimes \mathbf{t} + \int_A dA\, \mathbf{R} \otimes \mathbf{f}^{\text{ext}},
\end{aligned} \tag{B.26}$$

where we used the Stokes theorem to convert the integral over area $A$ into the integral over the boundary $\partial A$ with the outwards pointing unit normal vector $\hat{\mathbf{n}}$ and the length element $ds$. In Eq. (B.26) we also introduced boundary traction forces $\mathbf{t} = \hat{\boldsymbol{\sigma}} \cdot \hat{\mathbf{n}}$. Note that if the area element in Eq. (B.26) is restricted to a subset of the system, then the traction forces $\mathbf{t}$ are resulting from the internal forces between this area element and the rest of the system. Finally, we note that for a system that is mechanical equilibrium the position vectors $\mathbf{R}$ can be measured relative to an arbitrary origin $\mathbf{R}_O$. To demonstrate this, we introduce $\mathbf{R} = \tilde{\mathbf{R}} + \mathbf{R}_O$ and rewrite Eq. (B.26) as

$$\int_A dA\, \hat{\boldsymbol{\sigma}} = \int_{\partial A} ds\, \tilde{\mathbf{R}} \otimes \mathbf{t} + \int_A dA\, \tilde{\mathbf{R}} \otimes \mathbf{f}^{\text{ext}}$$

$$
\begin{aligned}
& + \mathbf{R}_O \otimes \left( \int_{\partial A} ds\, \mathbf{t} + \int_A dA\, \mathbf{f}^{\text{ext}} \right), \\
\int_A dA\, \hat{\boldsymbol{\sigma}} &= \int_{\partial A} ds\, \tilde{\mathbf{R}} \otimes \mathbf{t} + \int_A dA\, \tilde{\mathbf{R}} \otimes \mathbf{f}^{\text{ext}},
\end{aligned} \tag{B.27}
$$

where we took into account the force balance between boundary tractions and external forces, i.e., $\int_{\partial A} ds\, \mathbf{t} + \int_A dA\, \mathbf{f}^{\text{ext}} = 0$.

The general formalism discussed above can be applied to a cell $C$ with area $A_C$ in the vertex model to derive the stress tensor $\hat{\boldsymbol{\sigma}}_C$. Before continuing, we introduce the geometric center of the cell $C$ with $N_C$ vertices as $\mathbf{R}_C = \frac{1}{N_C} \sum_{i \in C} \mathbf{R}_i$, where the summation is over all vertices $i$ that belong to the cell $C$. We also define the position of vertices $i$ relative to the cell center $C$ as $\tilde{\mathbf{R}}_i = \mathbf{R}_i - \mathbf{R}_C$. The stress tensor $\hat{\boldsymbol{\sigma}}_C$ for cell $C$ can then be expressed as

$$
\begin{aligned}
\hat{\boldsymbol{\sigma}}_C &= \frac{1}{A_C} \int_A dA\, \hat{\boldsymbol{\sigma}}, \\
\hat{\boldsymbol{\sigma}}_C &= \frac{1}{A_C} \int_{\partial A} ds\, \tilde{\mathbf{R}} \otimes \mathbf{t} + \frac{1}{A_C} \int_A dA\, \tilde{\mathbf{R}} \otimes \mathbf{f}^{\text{ext}}.
\end{aligned} \tag{B.28}
$$

In the vertex model, the degrees of freedom are vertices. Thus the integrals in Eq. (B.28) can be rewritten as

$$
\hat{\boldsymbol{\sigma}}_C = \frac{1}{A_C} \sum_{i \in C} \tilde{\mathbf{R}}_i \otimes \mathbf{T}_{i \to C} + \frac{1}{A_C} \sum_{i \in C} \tilde{\mathbf{R}}_i \otimes \mathbf{F}^{\text{ext}}_{i \to C}. \tag{B.29}
$$

Here, $\mathbf{T}_{i \to C}$ and $\mathbf{F}^{\text{ext}}_{i \to C}$ are traction forces and external forces on the cell $C$ due to the vertex $i$, respectively.

Next we discuss how to relate the traction forces $\mathbf{T}_{i \to C}$ and external forces $\mathbf{F}^{\text{ext}}_{i \to C}$ to the elastic ($\mathbf{f}^{\text{e}}_i$) and dissipative ($\mathbf{f}^{\text{id}}_i$, $\mathbf{f}^{\text{ed}}_i$) forces acting on the vertex $i$. First, we note that each vertex $i$ is in a force balance, i.e.,

$$
\mathbf{0} = \mathbf{f}^{\text{e}}_i + \mathbf{f}^{\text{id}}_i + \mathbf{f}^{\text{ed}}_i,
$$

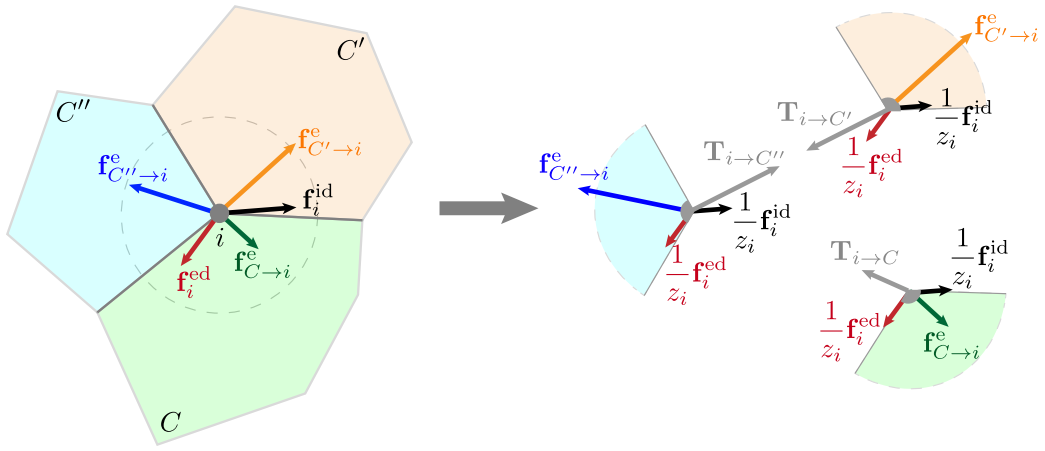


Figure B.2: The total force on a vertex is a sum of the mechanical forces from surrounding cells (blue, orange, and green) and internal (black) and external (red) dissipative forces. In order to compute the stress on each cell, it is convenient to make a virtual split of the vertex between all cells sharing it, as shown in the right panel. The force balance is then used for each subvertex to compute the reaction forces (grey) that develop due to the interactions between subvertices.

$$\mathbf{0} \;=\; \sum_{C\in\mathcal{N}_i} \mathbf{f}^{\mathrm{e}}_{C\to i} + \mathbf{f}^{\mathrm{id}}_i + \mathbf{f}^{\mathrm{ed}}_i, \tag{B.30}$$

where $\mathbf{f}^{\mathrm{e}}_{C\to i}$ is the elastic force contribution on the vertex $i$ due to cell $C$ and the set $\mathcal{N}_i$ contains $z_i$ cells that share vertex $i$. Then, we draw a free body diagram, where we split each vertex $i$ to $z_i$ subvertices (see Fig. B.2). Each subvertex belongs to one of the $z_i$ cells that share the vertex $i$. The subvertex that belongs to the cell $C$ experiences the elastic force $\mathbf{f}^{\mathrm{e}}_{C\to i}$. For simplicity, we assume that internal and external dissipative forces are distributed equally among the $z_i$ subvertices. Thus, each subvertex experiences the internal dissipative force $\mathbf{f}^{\mathrm{id}}_i/z_i$ and the external dissipative force $\mathbf{f}^{\mathrm{ed}}_i/z_i$. Internal forces between subvertices may also develop. The traction force $\mathbf{T}_{i\to C}$ thus represents the resultant force between the subvertex that belongs to the cell $C$ and all other subvertices. Each subvertex is in force balance and thus we can extract the traction force as

$$\mathbf{T}_{i\to C} = -\mathbf{f}^{\mathrm{e}}_{C\to i} - \frac{1}{z_i}\mathbf{f}^{\mathrm{id}}_i - \frac{1}{z_i}\mathbf{f}^{\mathrm{ed}}_i. \tag{B.31}$$

It is easy to check that the sum of all internal forces between subvertices, i.e., $\sum_{C\in\mathcal{N}_i}\mathbf{T}_{i\to C}=\mathbf{0}$, vanishes due to Newton's third law. Finally, we note that the external force $\mathbf{F}^{\rm ext}_{i\to C}$ arises due to the external dissipation between the subvertex that belongs to the cell $C$ and the substrate, i.e.,

$$\mathbf{F}^{\rm ext}_{i\to C}=\frac{1}{z_i}\mathbf{f}^{\rm ed}_i. \tag{B.32}$$

Using the expressions for the traction force $\mathbf{T}_{i\to C}$ in Eq. (B.31) and the external force $\mathbf{F}^{\rm ext}_{i\to C}$ in Eq. (B.32), we can express the stress tensor $\hat{\boldsymbol{\sigma}}_C$ for the cell $C$ in Eq. (B.29) as

$$\begin{aligned}
\hat{\boldsymbol{\sigma}}_C &= \frac{1}{A_C}\sum_{i\in C}\tilde{\mathbf{R}}_i\otimes\left(\mathbf{T}_{i\to C}+\mathbf{F}^{\rm ext}_{i\to C}\right),\\
\hat{\boldsymbol{\sigma}}_C &= \frac{1}{A_C}\sum_{i\in C}\tilde{\mathbf{R}}_i\otimes\left(-\mathbf{f}^{\rm e}_{C\to i}-\frac{1}{z_i}\mathbf{f}^{\rm id}_i-\frac{1}{z_i}\mathbf{f}^{\rm ed}_i+\frac{1}{z_i}\mathbf{f}^{\rm ed}_i\right),\\
\hat{\boldsymbol{\sigma}}_C &= -\frac{1}{A_C}\sum_{i\in C}\tilde{\mathbf{R}}_i\otimes\mathbf{f}^{\rm e}_{C\to i}-\frac{1}{A_C}\sum_{i\in C}\tilde{\mathbf{R}}_i\otimes\frac{1}{z_i}\mathbf{f}^{\rm id}_i,\\
\hat{\boldsymbol{\sigma}}_C &\equiv \hat{\boldsymbol{\sigma}}^{\rm e}_C+\hat{\boldsymbol{\sigma}}^{\rm id}_C.
\end{aligned} \tag{B.33}$$

In the above equation, the first time corresponds to the stress tensor $\hat{\boldsymbol{\sigma}}^{\rm e}_C$ for cell $C$ due to elastic forces, and the second term corresponds to the stress tensor $\hat{\boldsymbol{\sigma}}^{\rm id}_C$ for cell $C$ due to internal dissipative forces.

For the vertex model, the elastic force $\mathbf{f}^{\rm e}_{C\to i}$ on the vertex $i$ due to cell $C$ is given in Eq. (B.9) the stress tensor due to elastic forces can be expressed as

$$\begin{aligned}
\hat{\boldsymbol{\sigma}}^{\rm e}_C &= -\frac{1}{A_C}\sum_{i\in C}\tilde{\mathbf{R}}_i\otimes\mathbf{f}^{\rm e}_{C\to i},\\
\hat{\boldsymbol{\sigma}}^{\rm e}_C &= +\frac{K(A_C-A_0)}{2A_C}\sum_{i\in C}\tilde{\mathbf{R}}_i\otimes\left[(\mathbf{l}_{i,i+1}-\mathbf{l}_{i,i-1})\times\mathbf{e}_z\right]\\
&\quad -\frac{\Gamma\left(P_C-P_0\right)}{A_C}\sum_{i\in C}\tilde{\mathbf{R}}_i\otimes\left(\hat{\mathbf{l}}_{i,i-1}+\hat{\mathbf{l}}_{i,i+1}\right),
\end{aligned} \tag{B.34}$$

$$\hat{\boldsymbol{\sigma}}_C^{\mathrm{e}} \equiv \hat{\boldsymbol{\sigma}}_C^{\mathrm{e,area}} + \hat{\boldsymbol{\sigma}}_C^{\mathrm{e,per}}.$$

In the above equation, the first term describes the contribution to the elastic stress tensor $\hat{\boldsymbol{\sigma}}_C^{\mathrm{e,area}}$ due to the mismatch of the cell area $A_C$ from the target area $A_0$. Via direct calculation of the tensor components, one can show that this stress tensor can be expressed as

$$\hat{\boldsymbol{\sigma}}_C^{\mathrm{e,area}} = -\Pi_C \hat{\boldsymbol{I}}, \tag{B.35}$$

where $\Pi_C = -\frac{\partial E}{\partial A_C} = -K\left(A_C - A_0\right)$ is the hydrostatic pressure inside the cell $C$ and $\hat{\boldsymbol{I}}$ is the unit tensor.

The second term in Eq. (B.34) describes contribution to the elastic stress tensor $\hat{\boldsymbol{\sigma}}_C^{\mathrm{e,per}}$ due to the mismatch of the cell perimeter $P_C$ from the target perimeter $P_0$. This term can be further simplified by taking into account that the summation over vertices $i$ is cyclic to write

$$\begin{aligned}
\hat{\boldsymbol{\sigma}}_C^{\mathrm{e,per}} &= -\frac{\Gamma\left(P_C - P_0\right)}{A_C} \sum_{i \in C} \tilde{\mathbf{R}}_i \otimes \left(\hat{\mathbf{l}}_{i,i-1} + \hat{\mathbf{l}}_{i,i+1}\right), \\
\hat{\boldsymbol{\sigma}}_C^{\mathrm{e,per}} &= -\frac{\Gamma\left(P_C - P_0\right)}{A_C} \sum_{i \in C} \left(\tilde{\mathbf{R}}_{i+1} \otimes \hat{\mathbf{l}}_{i+1,i} + \tilde{\mathbf{R}}_i \otimes \hat{\mathbf{l}}_{i,i+1}\right), \\
\hat{\boldsymbol{\sigma}}_C^{\mathrm{e,per}} &= -\frac{\Gamma\left(P_C - P_0\right)}{A_C} \sum_{i \in C} \left(-\tilde{\mathbf{R}}_{i+1} + \tilde{\mathbf{R}}_i\right) \otimes \hat{\mathbf{l}}_{i,i+1}, \\
\hat{\boldsymbol{\sigma}}_C^{\mathrm{e,per}} &= +\frac{\Gamma\left(P_C - P_0\right)}{A_C} \sum_{i \in C} \mathbf{l}_{i,i+1} \otimes \hat{\mathbf{l}}_{i,i+1}, \\
\hat{\boldsymbol{\sigma}}_C^{\mathrm{e,per}} &= +\frac{\Gamma\left(P_C - P_0\right)}{A_C} \sum_{i \in C} \hat{\mathbf{l}}_{i,i+1} \otimes \mathbf{l}_{i,i+1}.
\end{aligned} \tag{B.36}$$

The final expression above can be rewritten as

$$\hat{\boldsymbol{\sigma}}_C^{\mathrm{e,per}} = \frac{1}{2A_C} \sum_{e \in C} \mathbf{T}_e \otimes \mathbf{l}_e, \tag{B.37}$$

where we introduced the tension $\mathbf{T}_e = \frac{\partial E}{\partial \mathbf{l}_e} = 2\Gamma\left(P_C - P_0\right)\hat{\mathbf{l}}_e$ along the junction $e$, and the summation is over all junctions $e$ that belong to cell $C$. The total stress tensor $\hat{\boldsymbol{\sigma}}^{\mathrm{e}}_C$ for cell $C$ due to elastic forces can thus be expressed concisely as

$$\hat{\boldsymbol{\sigma}}^{\mathrm{e}}_C = -\Pi_C \hat{\boldsymbol{I}} + \frac{1}{2A_C}\sum_{e\in C} \mathbf{T}_e \otimes \mathbf{l}_e. \tag{B.38}$$

Finally, we note that the in the absence of torque on a cell due to internal dissipative forces $\mathbf{f}^{\mathrm{id}}_i$, the stress tensor $\hat{\boldsymbol{\sigma}}^{\mathrm{id}}_C$ is symmetric [106]. This allows us to symmetrize the stress tensor as

$$\hat{\boldsymbol{\sigma}}^{\mathrm{id}}_C = -\frac{1}{2z_i A_c}\sum_{i\in C}\left(\tilde{\mathbf{R}}_i \otimes \mathbf{f}^{\mathrm{id}}_i + \mathbf{f}^{\mathrm{id}}_i \otimes \tilde{\mathbf{R}}_i\right). \tag{B.39}$$

# Appendix C

# Additional details and simulation setup for Chapter 4

## C.1 Discussion of the displacements continuity at the interface of the film and the substrate

When we wrote down the traction [see Eq. (4.20)] from the substrate in section 4.2, we assumed that the substrate's top surface has the same displacements as the central surface of the film, which are denoted as $(u(x), w(x))$. However, the displacement continuity requires that the substrate's top surface and the film's lower surface share the same displacements, which are $\left(u(x) + \frac{h}{2}w'(x), w(x)\right)$ from the kinematics of Föppl-von Kármán plate theory. Thus, the traction from the substrate, more precisely, should be given by the Fourier components as

$$\tilde{T}_y(k) = (K_1 + K_2\frac{h}{2}|k|)|k|\tilde{w}(k) - K_2 ik\tilde{u}(k) \tag{C.1a}$$

$$\tilde{T}_x(k) = (K_3 + K_4\frac{h}{2}|k|)ik\tilde{w}(k) + K_4|k|\tilde{u}(k), \tag{C.1b}$$

where $K_1 = K_4 = \frac{2E_s(1-\nu_s)}{(1+\nu_s)(3-4\nu_s)}, K_2 = K_3 = \frac{E_s(1-2\nu_s)}{(1+\nu_s)(3-4\nu_s)}$,$\tilde{w}(k), \tilde{u}(k)$ are the Fourier components of out-of-plane and in-plane displacements of the film respectively. For simplicity in notation, we denote $K_1' = K_1 + K_2\frac{h}{2}|k|$ and $K_3' = K_3 + K_4\frac{h}{2}|k|$.

The substrate's energy of Eq. (4.21) should be changed to,

$$\mathcal{U}_\mathrm{s} = \frac{1}{2}\sum_k \tilde{T}_y(k)\tilde{w}(-k) + \tilde{T}_x(k)\left(\tilde{u}(-k) + \frac{h}{2}(-ik)\tilde{w}(-k)\right) \tag{C.2}$$

We consider the same total energy density of Eq. (4.24) and set the variation to 0, which leads to the governing equations as

$$\begin{aligned} &Bk^4\tilde{w}(k) + E_0\sum_{k_1} k(k-k_1)\tilde{w}(k-k_1)\tilde{\epsilon}_{xx}(k_1) \\ &+(K_1' + \frac{h}{2}K_3'|k|)|k|\tilde{w}(k) - (K_2 + \frac{h}{2}K_4|k|)ik\tilde{u}(k) = \tilde{f}_y(k) + \frac{h}{2}ik\tilde{f}_x(k), \qquad \text{(C.3a)} \\ &E_0(-ik)\tilde{\epsilon}_{xx}(k) + (K_3 + \frac{h}{2}K_4|k|)ik\tilde{w}(k) + K_4|k|\tilde{u}(k) = \tilde{f}_x(k), \qquad \text{(C.3b)} \end{aligned}$$

which only adds a small correction to the stiffness of Fourier modes on the order of $\sim hk$ compared to Eq. (4.25a,4.25b). Since the dominant Fourier modes in the response spectrum are near the characteristic mode of wrinkles, this correction is $\sim hk_0 \sim \left(\frac{E_s}{E_f}\right)^{1/3}$, which is negligible when $\frac{E_f}{E_s} \gg 1$. Therefore, it is reasonable to assume the top surface of the substrate has displacement $(u(x), w(x))$ and work with Eq. (4.25a,4.25b) as the governing equations for force balance.

## C.2 Setup of finite element method (FEM) simulations

For all the results of FEM simulations in this paper, we used FEniCS open-source package [138]. According to the finite strain theory [123], the current configuration $\mathbf{x}$ is related to the initial configuration $\mathbf{X}_0$ by $\mathbf{x} = \mathbf{X}_0 + \mathbf{u}(\mathbf{X}_0)$, where $\mathbf{u}(\mathbf{X_0}) =$

$[u_1(\mathbf{X}_0), u_2(\mathbf{X}_0)]$ is the displacement field defined at the initial configuration. The deformation gradient tensor is defined as $\hat{\mathbf{F}} = \partial\mathbf{x}/\partial\mathbf{X}_0 = \hat{\mathbf{I}} + \partial\mathbf{u}/\partial\mathbf{X}_0$, where $\hat{\mathbf{I}}$ is the unit tensor.

To generate wrinkling instability, compression and growth of the film are equivalent when $E_f/E_s \gg 1$ [88]. Thus, we introduce a uni-axial growth $g$ in the film in the horizontal direction to effectively compress the film. The corresponding deformation gradient of growth is

$$\hat{\mathbf{F}}^{\mathbf{0}}_{\mathbf{g}} = \begin{bmatrix} g & 0 \\ 0 & 1 \end{bmatrix}. \tag{C.4}$$

where $g > 1$ in the film and $g = 1$ in the substrate. We consider the total deformation gradient $\hat{\mathbf{F}}^{\mathbf{0}}$ as a multiplication of an elastic part $\hat{\mathbf{F}}^{\mathbf{0}}_{\mathbf{e}}$ and the growth part $\hat{\mathbf{F}}^{\mathbf{0}}_{\mathbf{g}}$, i.e., $\hat{\mathbf{F}}^{\mathbf{0}} = \hat{\mathbf{F}}^{\mathbf{0}}_{\mathbf{e}}\hat{\mathbf{F}}^{\mathbf{0}}_{\mathbf{g}}$ [139], a schematic of which is shown in the Fig. C.1. $\hat{\mathbf{F}}^{\mathbf{0}}$ is identity matrix since no external deformation is applied and

$$\hat{\mathbf{F}}^{\mathbf{0}}_{\mathbf{e}} = \begin{bmatrix} 1+\epsilon_{xx} & 0 \\ 0 & 1 \end{bmatrix} \tag{C.5}$$

where $\epsilon_{xx}$ is the normal strain in horizontal direction. Thus, $\epsilon_{xx} = \frac{1-g}{g}$ and the loading parameter $\eta_x$ in Eq. (4.1) is $\eta_x = \frac{g-1}{g}$. Above the instability threshold, an additional

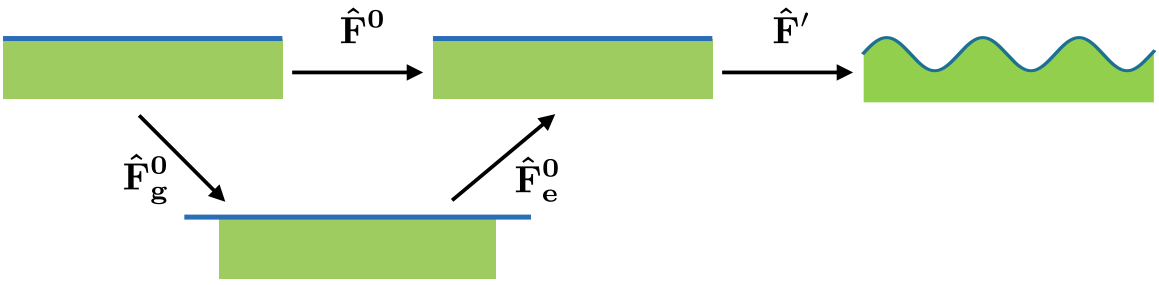


Figure C.1: A schematic of the decomposition of deformation gradient when growth is introduced in the film. Before wrinkling, the total deformation gradient $\hat{\mathbf{F}}^{\mathbf{0}}$ has decomposition $\hat{\mathbf{F}}^{\mathbf{0}} = \hat{\mathbf{F}}^{\mathbf{0}}_{\mathbf{e}}\hat{\mathbf{F}}^{\mathbf{0}}_{\mathbf{g}}$. $\hat{\mathbf{F}}'$ is the wrinkling deformation on top of $\hat{\mathbf{F}}^{\mathbf{0}}$.

deformation gradient $\hat{\mathbf{F}}'$ is superposed on top of the initial elastic deformation gradient

$\hat{\mathbf{F}}^{\mathbf{0}}_{\mathbf{e}}$, which gives the total elastic deformation gradient as $\hat{\mathbf{F}}_{\mathbf{e}} = \hat{\mathbf{F}}'\hat{\mathbf{F}}^{\mathbf{0}}_{\mathbf{e}}$. We model the film and substrate as a neo-Hookean solid, the energy density of which is

$$\psi = \frac{\mu}{2}(I_c - 2) - \mu \ln(J) + \frac{\lambda}{2}\ln(J)^2, \tag{C.6}$$

where $\mu$ and $\lambda$ are the Lame constants and are different for the film and the substrate, $I_c = \text{trace}(\hat{\mathbf{F}}^{\mathbf{T}}_{\mathbf{e}}\hat{\mathbf{F}}_{\mathbf{e}})$ and $J = \det(\hat{\mathbf{F}}_{\mathbf{e}})$. Note that neo-Hookean solid is equivalent to linear elastic materials in small strain limit. The total potential energy is given by

$$\Pi = \int \psi dx - \int \mathbf{f} \cdot \mathbf{u} dx, \tag{C.7}$$

where $\mathbf{f}$ is the external force, $\mathbf{u}$ represents the displacement field. The FEM simulations seek the solution of the variational equation $\delta\Pi = 0$. We apply fixed boundary condition to the bottom boundary and periodic boundary conditions to the left and right. The boundary condition is consistent with the Fourier mode formalism. Besides, the displacements in the substrate decay exponentially from the top. Thus, a substrate with height of multiple wavelengths of the wrinkles and a fixed boundary at the bottom is sufficient.

In the absence of external forces, we calculate the instability threshold $\eta_{x,cr}$ for given simulation parameters by finding the compression $\eta_x$ at which the flat state of bilayer structures becomes unstable. Instability occurs when the smallest eigenvalue of the Jacobian $\delta^2\Pi$ changes from positive to negative. We use SLEPC library to solve the eigenvalue problem. To obtain the wrinkled state when $\eta_x > \eta_{x,cr}$, we perturb the initial guess along the direction of the eigenvector that corresponds to the smallest eigenvalue. The wrinkled state, denoted as $\mathbf{u_w}$, satisfies $\delta\psi(\mathbf{u_w}) = 0$.

In the presence of external forces, the equations of the variational problem become

$$\delta\psi = \mathbf{f}. \tag{C.8}$$

When we use simulation results to verify the linear response theory, we linearize the left-hand side of Eq. (C.8) around the wrinkled state $\mathbf{u_w}$. We solve the linearized equations $\delta^2\psi(\mathbf{u_w})\mathbf{u_a} = \mathbf{f}$, where $\delta^2\psi(\mathbf{u_w})$ is the Jacobian evaluated at $\mathbf{u_w}$, $\mathbf{u_a}$ is the additional displacement due to the external forces $\mathbf{f}$. Note that when we study the shift of wrinkles in section 4.3.4, we solve the nonlinear problem of Eq. (C.8) with the wrinkled state $\mathbf{u_w}$ as the initial guess and tiny external forces $\mathbf{f}$. We keep the system's nonlinearity because linear response diverges even when external forces are infinitesimal [see Eq. (4.39b) for zero stiffness of odd characteristic mode].

The convergent analysis of FEM simulation results is shown in Fig. C.2. We measure the additional vertical displacements at the same location with different mesh sizes. The results from the finest mesh size are used as a reference to calculate the error. Fig. C.2 shows the error as a function of the mesh size. Since we use the second-order element, the error curve roughly converges with an exponent of 3, which is indicated by the blue dashed line.

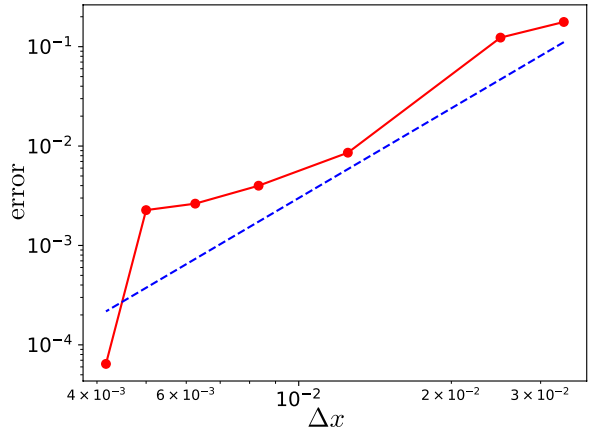


Figure C.2: The error of FEM simulations (red line) as a function of the smallest mesh size $\Delta x$. We apply a vertical point force at the peak of wrinkles and measure the additional vertical displacement at the peak. For the results in this figure, we use $E_f/E_s = 10^2$, and the system has 5 waves. The blue curve indicates that the exponent of the convergent rate is 3.

# Bibliography


[1] S. R. Nagel, "Experimental soft-matter science," *Reviews of modern physics*, vol. 89, no. 2, p. 025002, 2017.

[2] F. H. Stillinger and P. G. Debenedetti, "Glass transition thermodynamics and kinetics," *Annu. Rev. Condens. Matter Phys.*, vol. 4, no. 1, pp. 263–285, 2013.

[3] D. Bonn, M. M. Denn, L. Berthier, T. Divoux, and S. Manneville, "Yield stress materials in soft condensed matter," *Reviews of Modern Physics*, vol. 89, no. 3, p. 035005, 2017.

[4] M. Marchetti, J. Joanny, S. Ramaswamy, T. Liverpool, J. Prost, M. Rao, and R. A. Simha, "Hydrodynamics of soft active matter," *Rev. Mod. Phys.*, vol. 85, no. 3, p. 1143, 2013.

[5] T. Lecuit, P.-F. Lenne, and E. Munro, "Force generation, transmission, and integration during cell and tissue morphogenesis," *Annual Review of Cell and Developmental Biology*, vol. 27, pp. 157–184, 2011.

[6] C.-P. Heisenberg and Y. Bellaïche, "Forces in tissue morphogenesis and patterning," *Cell*, vol. 153, no. 5, pp. 948–962, 2013.

[7] E. Hannezo and C.-P. Heisenberg, "Mechanochemical feedback loops in development and disease," *Cell*, vol. 178, no. 1, pp. 12–25, 2019.

[8] N. I. Petridou and C.-P. Heisenberg, "Tissue rheology in embryonic organization," *EMBO J.*, vol. 38, no. 20, p. e102497, 2019.

[9] M. H. Ross and W. Pawlina, *Histology*. Lippincott Williams & Wilkins, 2006.

[10] D. Krndija, F. El Marjou, B. Guirao, S. Richon, O. Leroy, Y. Bellaiche, E. Hannezo, and D. M. Vignjevic, "Active cell migration is critical for steady-state epithelial turnover in the gut," *Science*, vol. 365, no. 6454, pp. 705–710, 2019.

[11] L. Wolpert, C. Tickle, and A. M. Arias, *Principles of development*. Oxford University Press, USA, 2015.

[12] R. A. Weinberg, *The biology of cancer*. Garland Science, 2013.

[13] G. Forgacs, R. A. Foty, Y. Shafrir, and M. S. Steinberg, "Viscoelastic properties of living embryonic tissues: a quantitative study," *Biophysical Journal*, vol. 74, no. 5, pp. 2227–2234, 1998.

[14] P. Friedl and D. Gilmour, "Collective cell migration in morphogenesis, regeneration and cancer," *Nature Reviews Molecular Cell Biology*, vol. 10, no. 7, pp. 445–457, 2009.

[15] R. Alert and X. Trepat, "Physical models of collective cell migration," *Annual Review of Condensed Matter Physics*, vol. 11, pp. 77–101, 2020.

[16] M. Poujade, E. Grasland-Mongrain, A. Hertzog, J. Jouanneau, P. Chavrier, B. Ladoux, A. Buguin, and P. Silberzan, "Collective migration of an epithelial monolayer in response to a model wound," *Proc. Natl. Acad. Sci. U.S.A.*, vol. 104, no. 41, pp. 15988–15993, 2007.

[17] X. Trepat, M. R. Wasserman, T. E. Angelini, E. Millet, D. A. Weitz, J. P. Butler, and J. J. Fredberg, "Physical forces during collective cell migration," *Nat. Phys.*, vol. 5, no. 6, pp. 426–430, 2009.

[18] D. T. Tambe, C. C. Hardin, T. E. Angelini, K. Rajendran, C. Y. Park, X. Serra-Picamal, E. H. Zhou, M. H. Zaman, J. P. Butler, D. A. Weitz, *et al.*, "Collective cell guidance by cooperative intercellular forces," *Nat. Mater.*, vol. 10, no. 6, pp. 469–475, 2011.

[19] A. Brugués, E. Anon, V. Conte, J. H. Veldhuis, M. Gupta, J. Colombelli, J. J. Muñoz, G. W. Brodland, B. Ladoux, and X. Trepat, "Forces driving epithelial wound healing," *Nat. Phys.*, vol. 10, pp. 683–690, 2014.

[20] R. Etournay, M. Popović, M. Merkel, A. Nandi, C. Blasse, B. Aigouy, H. Brandl, G. Myers, G. Salbreux, F. Jülicher, *et al.*, "Interplay of cell dynamics and epithelial tension during morphogenesis of the drosophila pupal wing," *eLife*, vol. 4, p. e07090, 2015.

[21] T. E. Angelini, E. Hannezo, X. Trepat, M. Marquez, J. J. Fredberg, and D. A. Weitz, "Glass-like dynamics of collective cell migration," *Proc. Natl. Acad. Sci. U.S.A.*, vol. 108, no. 12, pp. 4714–4719, 2011.

[22] J.-A. Park, J. H. Kim, D. Bi, J. A. Mitchel, N. T. Qazvini, K. Tantisira, C. Y. Park, M. McGill, S.-H. Kim, B. Gweon, *et al.*, "Unjamming and cell shape in the asthmatic airway epithelium," *Nat. Mater.*, vol. 14, no. 10, pp. 1040–1048, 2015.

[23] D. Bi, J. Lopez, J. M. Schwarz, and M. L. Manning, "A density-independent rigidity transition in biological tissues," *Nat. Phys.*, vol. 11, no. 12, pp. 1074–1079, 2015.

[24] D. Bi, X. Yang, M. C. Marchetti, and M. L. Manning, "Motility-driven glass and jamming transitions in biological tissues," *Phys. Rev. X*, vol. 6, no. 2, p. 021011, 2016.

[25] L. Atia, D. Bi, Y. Sharma, J. A. Mitchel, B. Gweon, S. A. Koehler, S. J. DeCamp, B. Lan, J. H. Kim, R. Hirsch, *et al.*, "Geometric constraints during epithelial jamming," *Nat. Phys.*, vol. 14, no. 6, pp. 613–620, 2018.

[26] D. M. Sussman, M. Paoluzzi, M. C. Marchetti, and M. L. Manning, "Anomalous glassy dynamics in simple models of dense biological tissue," *EPL (Europhysics Lett.)*, vol. 121, no. 3, p. 36001, 2018.

[27] M. Czajkowski, D. M. Sussman, M. C. Marchetti, and M. L. Manning, "Glassy dynamics in models of confluent tissue with mitosis and apoptosis," *Soft Matter*, vol. 15, no. 44, pp. 9133–9149, 2019.

[28] S. Henkes, K. Kostanjevec, J. M. Collinson, R. Sknepnek, and E. Bertin, "Dense active matter model of motion patterns in confluent cell monolayers," *Nat. Commun.*, vol. 11, no. 1, pp. 1–9, 2020.

[29] B. Szabo, G. Szöllösi, B. Gönci, Z. Jurányi, D. Selmeczi, and T. Vicsek, "Phase transition in the collective migration of tissue cells: experiment and model," *Phys. Rev. E*, vol. 74, no. 6, p. 061908, 2006.

[30] M. Sadati, N. T. Qazvini, R. Krishnan, C. Y. Park, and J. J. Fredberg, "Collective migration and cell jamming," *Differentiation*, vol. 86, no. 3, pp. 121–125, 2013.

[31] S. Garcia, E. Hannezo, J. Elgeti, J.-F. Joanny, P. Silberzan, and N. S. Gov, "Physics of active jamming during collective cellular motion in a monolayer," *Proc. Natl. Acad. Sci. U.S.A.*, vol. 112, no. 50, pp. 15314–15319, 2015.

[32] M. Merkel and M. L. Manning, "A geometrically controlled rigidity transition in a model for confluent 3d tissues," *New J. Phys.*, vol. 20, no. 2, p. 022002, 2018.

[33] J. A. Mitchel, A. Das, M. J. O'Sullivan, I. T. Stancil, S. J. DeCamp, S. Koehler, O. H. Ocaña, J. P. Butler, J. J. Fredberg, M. A. Nieto, *et al.*, "In primary airway epithelial cells, the unjamming transition is distinct from the epithelial-to-mesenchymal transition," *Nat. Commun.*, vol. 11, no. 1, pp. 1–14, 2020.

[34] B. Bénazéraf, P. Francois, R. E. Baker, N. Denans, C. D. Little, and O. Pourquié, "A random cell motility gradient downstream of fgf controls elongation of an amniote embryo," *Nature*, vol. 466, no. 7303, pp. 248–252, 2010.

[35] A. K. Lawton, A. Nandi, M. J. Stulberg, N. Dray, M. W. Sneddon, W. Pontius, T. Emonet, and S. A. Holley, "Regulated tissue fluidity steers zebrafish body elongation," *Development*, vol. 140, no. 3, pp. 573–582, 2013.

[36] A. Mongera, P. Rowghanian, H. J. Gustafson, E. Shelton, D. A. Kealhofer, E. K. Carn, F. Serwane, A. A. Lucio, J. Giammona, and O. Campàs, "A fluid-to-solid jamming transition underlies vertebrate body axis elongation," *Nature*, vol. 561, no. 7723, pp. 401–405, 2018.

[37] N. Desprat, A. Guiroy, and A. Asnacios, "Microplates-based rheometer for a single living cell," *Review of Scientific Instruments*, vol. 77, no. 5, p. 055111, 2006.

[38] G. Salbreux, G. Charras, and E. Paluch, "Actin cortex mechanics and cellular morphogenesis," *Trends Cell Biol.*, vol. 22, no. 10, pp. 536–545, 2012.

[39] H. Berthoumieux, J.-L. Maître, C.-P. Heisenberg, E. K. Paluch, F. Jülicher, and G. Salbreux, "Active elastic thin shell theory for cellular deformations," *New J. Phys.*, vol. 16, no. 6, p. 065005, 2014.

[40] A. R. Harris, L. Peter, J. Bellis, B. Baum, A. J. Kabla, and G. T. Charras, "Characterizing the mechanics of cultured cell monolayers," *Proc. Natl. Acad. Sci. U.S.A.*, vol. 109, no. 41, pp. 16449–16454, 2012.

[41] A. Bonfanti, J. Fouchard, N. Khalilgharibi, G. Charras, and A. Kabla, "A unified rheological model for cells and cellularised materials," *R. Soc. Open Sci.*, vol. 7, no. 1, p. 190920, 2020.

[42] D. Matoz-Fernandez, E. Agoritsas, J.-L. Barrat, E. Bertin, and K. Martens, "Nonlinear rheology in a model biological tissue," *Phys. Rev. Lett.*, vol. 118, no. 15, p. 158105, 2017.

[43] T. Nagai and H. Honda, "A dynamic cell model for the formation of epithelial tissues," *Philosophical Magazine B*, vol. 81, no. 7, pp. 699–719, 2001.

[44] R. Farhadifar, J.-C. Röper, B. Aigouy, S. Eaton, and F. Jülicher, "The influence of cell mechanics, cell-cell interactions, and proliferation on epithelial packing," *Curr. Biol.*, vol. 17, no. 24, pp. 2095–2104, 2007.

[45] A. G. Fletcher, M. Osterfield, R. E. Baker, and S. Y. Shvartsman, "Vertex models of epithelial morphogenesis," *Biophys. J.*, vol. 106, pp. 2291–2304, 2014.

[46] D. L. Barton, S. Henkes, C. J. Weijer, and R. Sknepnek, "Active vertex model for cell-resolution description of epithelial tissue mechanics," *PLOS Comput. Biol.*, vol. 13, no. 6, p. e1005569, 2017.

[47] J. Huang, J. O. Cochran, S. M. Fielding, M. C. Marchetti, and D. Bi, "Shear-driven solidification and nonlinear elasticity in epithelial tissues," *arXiv preprint arXiv:2109.10374*, 2021.

[48] M. Moshe, M. J. Bowick, and M. C. Marchetti, "Geometric frustration and solid-solid transitions in model 2d tissue," *Phys. Rev. Lett.*, vol. 120, no. 26, p. 268105, 2018.

[49] M. Popović, V. Druelle, N. Dye, F. Jülicher, and M. Wyart, "Inferring the flow properties of epithelial tissues from their geometry," *New J. Phys.*, vol. 23, p. 033004, 2021.

[50] P.-F. Lenne and V. Trivedi, "Sculpting tissues by phase transitions," *Nat. Commun.*, vol. 13, p. 664, 2022.

[51] M. Merkel, K. Baumgarten, B. P. Tighe, and M. L. Manning, "A minimal-length approach unifies rigidity in underconstrained materials," *Proc. Natl. Acad. Sci. U.S.A.*, vol. 116, no. 14, pp. 6560–6568, 2019.

[52] S. Tong, N. K. Singh, R. Sknepnek, and A. Košmrlj, "Linear viscoelastic properties of the vertex model for epithelial tissues," *PLoS Comput. Biol.*, vol. 18, no. 5, p. e1010135, 2022.

[53] J. Huang, J. O. Cochran, S. M. Fielding, M. C. Marchetti, and D. Bi, "Shear-driven solidification and nonlinear elasticity in epithelial tissues," *Phys. Rev. Lett.*, vol. 128, p. 178001, 2022.

[54] I. Tah, T. Sharp, A. Liu, and D. M. Sussman, "Quantifying the link between local structure and cellular rearrangements using information in models of biological tissues," *Soft Matter*, 2021.

[55] P. C. Sanematsu, G. Erdemci-Tandogan, H. Patel, E. Retzlaff, J. D. Amack, and L. Manning, "3d viscoelastic drag forces drive changes to cell shapes during organogenesis in the zebrafish embryo," *bioRxiv*, 2021.

[56] N. W. Ashcroft and N. D. Mermin, *Solid State Physics*. Holt-Saunders, 1976.

[57] G. Pessot, H. Löwen, and A. M. Menzel, "Dynamic elastic moduli in magnetic gels: Normal modes and linear response," *J. Chem. Phys.*, vol. 145, no. 10, p. 104904, 2016.

[58] V. V. Palyulin, C. Ness, R. Milkus, R. M. Elder, T. W. Sirk, and A. Zaccone, "Parameter-free predictions of the viscoelastic response of glassy polymers from non-affine lattice dynamics," *Soft Matter*, vol. 14, no. 42, pp. 8475–8482, 2018.

[59] I. Kriuchevskyi, V. V. Palyulin, R. Milkus, R. M. Elder, T. W. Sirk, and A. Zaccone, "Scaling up the lattice dynamics of amorphous materials by orders of magnitude," *Phys. Rev. B*, vol. 102, no. 2, p. 024108, 2020.

[60] H. Honda and G. Eguchi, "How much does the cell boundary contract in a monolayered cell sheet?," *J. Theor. Biol.*, vol. 84, no. 3, pp. 575–588, 1980.

[61] A. G. Fletcher, J. M. Osborne, P. K. Maini, and D. J. Gavaghan, "Implementing vertex dynamics models of cell populations in biology within a consistent computational framework," *Prog. Biophys. Mol. Biol.*, vol. 113, no. 2, pp. 299–326, 2013.

[62] M. Popović, V. Druelle, N. A. Dye, F. Jülicher, and M. Wyart, "Inferring the flow properties of epithelial tissues from their geometry," *New J. Phys.*, vol. 23, no. 3, p. 033004, 2021.

[63] A. Das, S. Sastry, and D. Bi, "Controlled neighbor exchanges drive glassy behavior, intermittency, and cell streaming in epithelial tissues," *Phys. Rev. X*, vol. 11, no. 4, p. 041037, 2021.

[64] C. Duclut, J. Paijmans, M. M. Inamdar, C. D. Modes, and F. Jülicher, "Nonlinear rheology of cellular networks," *Cells & Development*, vol. 168, p. 203746, 2021.

[65] S. Tong, R. Sknepnek, and A. Košmrlj, "Linear viscoelastic response of the vertex model with internal and external dissipation: Normal modes analysis," *Physical Review Research*, vol. 5, no. 1, p. 013143, 2023.

[66] H. G. Allen, *Analysis and design of structural sandwich panels*. Pergamon Press, New York, 1969.

[67] N. Bowden, S. Brittain, A. G. Evans, J. W. Hutchinson, and G. M. Whitesides, "Spontaneous formation of ordered structures in thin films of metals supported on an elastomeric polymer," *Nature*, vol. 393, no. 6681, p. 146, 1998.

[68] E. Cerda and L. Mahadevan, "Geometry and physics of wrinkling," *Physical review letters*, vol. 90, no. 7, p. 074302, 2003.

[69] X. Chen and J. W. Hutchinson, "Herringbone buckling patterns of compressed thin films on compliant substrates," *Journal of applied mechanics*, vol. 71, no. 5, pp. 597–603, 2004.

[70] Z. Huang, W. Hong, and Z. Suo, "Nonlinear analyses of wrinkles in a film bonded to a compliant substrate," *Journal of the Mechanics and Physics of Solids*, vol. 53, no. 9, pp. 2101–2118, 2005.

[71] H. Jiang, D.-Y. Khang, J. Song, Y. Sun, Y. Huang, and J. A. Rogers, "Finite deformation mechanics in buckled thin films on compliant supports," *Proceedings of the National Academy of Sciences*, vol. 104, no. 40, pp. 15607–15612, 2007.

[72] B. Audoly and A. Boudaoud, "Buckling of a stiff film bound to a compliant substrate—part i:: Formulation, linear stability of cylindrical patterns, secondary bifurcations," *Journal of the Mechanics and Physics of Solids*, vol. 56, no. 7, pp. 2401–2421, 2008.

[73] S. Cai, D. Breid, A. J. Crosby, Z. Suo, and J. W. Hutchinson, "Periodic patterns and energy states of buckled films on compliant substrates," *Journal of the Mechanics and Physics of Solids*, vol. 59, no. 5, pp. 1094–1114, 2011.

[74] F. Brau, H. Vandeparre, A. Sabbah, C. Poulard, A. Boudaoud, and P. Damman, "Multiple-length-scale elastic instability mimics parametric resonance of nonlinear oscillators," *Nature Physics*, vol. 7, no. 1, p. 56, 2011.

[75] D.-H. Kim and J. A. Rogers, "Stretchable electronics: materials strategies and devices," *Advanced materials*, vol. 20, no. 24, pp. 4887–4892, 2008.

[76] B. Xu, A. Akhtar, Y. Liu, H. Chen, W.-H. Yeo, S. I. Park, B. Boyce, H. Kim, J. Yu, H.-Y. Lai, *et al.*, "An epidermal stimulation and sensing platform for sensorimotor prosthetic control, management of lower back exertion, and electrical muscle activation," *Advanced Materials*, vol. 28, no. 22, pp. 4462–4471, 2016.

[77] J. Dervaux, Y. Couder, M.-A. Guedeau-Boudeville, and M. B. Amar, "Shape transition in artificial tumors: from smooth buckles to singular creases," *Physical review letters*, vol. 107, no. 1, p. 018103, 2011.

[78] D. P. Richman, R. M. Stewart, J. W. Hutchinson, and V. S. Caviness, "Mechanical model of brain convolutional development," *Science*, vol. 189, no. 4196, pp. 18–21, 1975.

[79] M. Kücken and A. C. Newell, "A model for fingerprint formation," *EPL (Europhysics Letters)*, vol. 68, no. 1, p. 141, 2004.

[80] E. Hohlfeld and L. Mahadevan, "Unfolding the sulcus," *Physical review letters*, vol. 106, no. 10, p. 105702, 2011.

[81] A. E. Shyer, T. Tallinen, N. L. Nerurkar, Z. Wei, E. S. Gil, D. L. Kaplan, C. J. Tabin, and L. Mahadevan, "Villification: how the gut gets its villi," *Science*, vol. 342, no. 6155, pp. 212–218, 2013.

[82] D. Terwagne, M. Brojan, and P. M. Reis, "Smart morphable surfaces for aerodynamic drag control," *Advanced materials*, vol. 26, no. 38, pp. 6608–6611, 2014.

[83] J. Y. Chung, J. P. Youngblood, and C. M. Stafford, "Anisotropic wetting on tunable micro-wrinkled surfaces," *Soft Matter*, vol. 3, no. 9, pp. 1163–1169, 2007.

[84] P.-C. Lin, S. Vajpayee, A. Jagota, C.-Y. Hui, and S. Yang, "Mechanically tunable dry adhesive from wrinkled elastomers," *Soft Matter*, vol. 4, no. 9, pp. 1830–1835, 2008.

[85] S. Nagashima, H. D. Ha, A. Košmrlj, H. A. Stone, M.-W. Moon, *et al.*, "Spontaneous formation of aligned dna nanowires by capillarity-induced skin folding," *Proceedings of the National Academy of Sciences*, vol. 114, no. 24, pp. 6233–6237, 2017.

[86] L. Pocivavsek, R. Dellsy, A. Kern, S. Johnson, B. Lin, K. Y. C. Lee, and E. Cerda, "Stress and fold localization in thin elastic membranes," *Science*, vol. 320, no. 5878, pp. 912–916, 2008.

[87] K. Efimenko, M. Rackaitis, E. Manias, A. Vaziri, L. Mahadevan, and J. Genzer, "Nested self-similar wrinkling patterns in skins," *Nature materials*, vol. 4, no. 4, pp. 293–297, 2005.

[88] M. Holland, B. Li, X. Feng, and E. Kuhl, "Instabilities of soft films on compliant substrates," *Journal of the Mechanics and Physics of Solids*, vol. 98, pp. 350–365, 2017.

[89] D. Staple, R. Farhadifar, J.-C. Röper, B. Aigouy, S. Eaton, and F. Jülicher, "Mechanics and remodelling of cell packings in epithelia," *Eur. Phys. J. E*, vol. 33, no. 2, pp. 117–127, 2010.

[90] D. Bi, J. H. Lopez, J. Schwarz, and M. L. Manning, "Energy barriers and cell migration in densely packed tissues," *Soft Matter*, vol. 10, no. 12, pp. 1885–1890, 2014.

[91] A. Hernandez, M. F. Staddon, M. J. Bowick, M. C. Marchetti, and M. Moshe, "Geometric rigidity and anomalous elasticity of cellular tissue vertex model," *arXiv preprint arXiv:2109.10407*, 2021.

[92] L. Yan and D. Bi, "Multicellular rosettes drive fluid-solid transition in epithelial tissues," *Phys. Rev. X*, vol. 9, no. 1, p. 011029, 2019.

[93] X. Wang, M. Merkel, L. B. Sutter, G. Erdemci-Tandogan, M. L. Manning, and K. E. Kasza, "Anisotropy links cell shapes to tissue flow during convergent extension," *Proc. Natl. Acad. Sci. U.S.A.*, vol. 117, no. 24, pp. 13541–13551, 2020.

[94] E. Bitzek, P. Koskinen, F. Gähler, M. Moseler, and P. Gumbsch, "Structural relaxation made simple," *Phys. Rev. Lett.*, vol. 97, no. 17, p. 170201, 2006.

[95] A. Hočevar and P. Ziherl, "Degenerate polygonal tilings in simple animal tissues," *Phys. Rev. E*, vol. 80, no. 1, p. 011904, 2009.

[96] S. Torquato and H. Haslach Jr, "Random heterogeneous materials: microstructure and macroscopic properties," *Appl. Mech. Rev.*, vol. 55, no. 4, pp. B62–B63, 2002.

[97] P. Virtanen, R. Gommers, T. E. Oliphant, M. Haberland, T. Reddy, D. Cournapeau, E. Burovski, P. Peterson, W. Weckesser, J. Bright, S. J. van der Walt, M. Brett, J. Wilson, K. J. Millman, N. Mayorov, A. R. J. Nelson, E. Jones, R. Kern, E. Larson, C. J. Carey, İ. Polat, Y. Feng, E. W. Moore, J. VanderPlas, D. Laxalde, J. Perktold, R. Cimrman, I. Henriksen, E. A. Quintero, C. R. Harris, A. M. Archibald, A. H. Ribeiro, F. Pedregosa, P. van Mulbregt, and SciPy 1.0

Contributors, "SciPy 1.0: Fundamental Algorithms for Scientific Computing in Python," *Nature Methods*, vol. 17, pp. 261–272, 2020.

[98] E. M. Purcell, "Life at low reynolds number," *American journal of physics*, vol. 45, no. 1, pp. 3–11, 1977.

[99] S. Walcott and S. X. Sun, "A mechanical model of actin stress fiber formation and substrate elasticity sensing in adherent cells," *Proc. Natl. Acad. Sci. U.S.A.*, vol. 107, no. 17, pp. 7757–7762, 2010.

[100] P. Sens, "Rigidity sensing by stochastic sliding friction," *EPL (Europhysics Lett.)*, vol. 104, no. 3, p. 38003, 2013.

[101] U. S. Schwarz and S. A. Safran, "Physics of adherent cells," *Reviews of Modern Physics*, vol. 85, no. 3, p. 1327, 2013.

[102] S. Curran, C. Strandkvist, J. Bathmann, M. de Gennes, A. Kabla, G. Salbreux, and B. Baum, "Myosin ii controls junction fluctuations to guide epithelial tissue ordering," *Developmental Cell*, vol. 43, no. 4, pp. 480–492, 2017.

[103] B. Leimkuhler and C. Matthews, *Molecular Dynamics.* Springer, 2016.

[104] K. K. Chiou, L. Hufnagel, and B. I. Shraiman, "Mechanical stress inference for two dimensional cell arrays," *PLoS Comput. Biol.*, vol. 8, no. 5, p. e1002512, 2012.

[105] X. Yang, D. Bi, M. Czajkowski, M. Merkel, M. L. Manning, and M. C. Marchetti, "Correlating cell shape and cellular stress in motile confluent tissues," *Proc. Natl. Acad. Sci. U.S.A.*, vol. 114, no. 48, pp. 12663–12668, 2017.

[106] A. Nestor-Bergmann, G. Goddard, S. Woolner, and O. E. Jensen, "Relating cell shape and mechanical stress in a spatially disordered epithelium using a vertex-based model," *Math. Med. Biol.*, vol. 35, no. Supplement_1, pp. i1–i27, 2018.

[107] R. G. Larson, *The Structure and Rheology of Complex Fluids*, vol. 150. Oxford University Press New York, 1999.

[108] T. P. Wyatt, J. Fouchard, A. Lisica, N. Khalilgharibi, B. Baum, P. Recho, A. J. Kabla, and G. T. Charras, "Actomyosin controls planarity and folding of epithelia in response to compression," *Nat. Mater.*, vol. 19, no. 1, pp. 109–117, 2020.

[109] N. Murisic, V. Hakim, I. G. Kevrekidis, S. Y. Shvartsman, and B. Audoly, "From discrete to continuum models of three-dimensional deformations in epithelial sheets," *Biophysical Journal*, vol. 109, no. 1, pp. 154–163, 2015.

[110] M. C. Gibson, A. B. Patel, R. Nagpal, and N. Perrimon, "The emergence of geometric order in proliferating metazoan epithelia," *Nature*, vol. 442, no. 7106, pp. 1038–1041, 2006.

[111] D. M. Sussman and M. Merkel, "No unjamming transition in a voronoi model of biological tissue," *Soft matter*, vol. 14, no. 17, pp. 3397–3403, 2018.

[112] N. Noll, M. Mani, I. Heemskerk, S. J. Streichan, and B. I. Shraiman, "Active tension network model suggests an exotic mechanical state realized in epithelial tissues," *Nat. Phys.*, vol. 13, no. 12, pp. 1221–1226, 2017.

[113] C. Kane and T. Lubensky, "Topological boundary modes in isostatic lattices," *Nat. Phys.*, vol. 10, no. 1, pp. 39–45, 2014.

[114] T. Lubensky, C. Kane, X. Mao, A. Souslov, and K. Sun, "Phonons and elasticity in critically coordinated lattices," *Rep. Prog. Phys.*, vol. 78, no. 7, p. 073901, 2015.

[115] J. Paulose, B. G.-g. Chen, and V. Vitelli, "Topological modes bound to dislocations in mechanical metamaterials," *Nat. Phys.*, vol. 11, no. 2, pp. 153–156, 2015.

[116] D. Z. Rocklin, S. Zhou, K. Sun, and X. Mao, "Transformable topological mechanical metamaterials," *Nat. Commun.*, vol. 8, no. 1, pp. 1–9, 2017.

[117] X. Mao and T. C. Lubensky, "Maxwell lattices and topological mechanics," *Annual Review of Condensed Matter Physics*, vol. 9, pp. 413–433, 2018.

[118] R. Vincent, E. Bazellières, C. Pérez-González, M. Uroz, X. Serra-Picamal, and X. Trepat, "Active tensile modulus of an epithelial monolayer," *Phys. Rev. Lett.*, vol. 115, no. 24, p. 248103, 2015.

[119] B. N. Parlett, *The Symmetric Eigenvalue Problem*. SIAM, 1998.

[120] E. Lerner, G. Düring, and M. Wyart, "A unified framework for non-brownian suspension flows and soft amorphous solids," *Proc. Natl. Acad. Sci. U.S.A.*, vol. 109, no. 13, pp. 4798–4803, 2012.

[121] E. Lerner, G. Düring, and M. Wyart, "Simulations of driven overdamped frictionless hard spheres," *Comput. Phys. Commun.*, vol. 184, no. 3, pp. 628–637, 2013.

[122] A. Lemaître and C. Maloney, "Sum rules for the quasi-static and visco-elastic response of disordered solids at zero temperature," *J. Stat. Phys.*, vol. 123, no. 2, pp. 415–453, 2006.

[123] M. E. Gurtin, E. Fried, and L. Anand, *The Mechanics and Thermodynamics of Continua*. Cambridge University Press, 2010.

[124] C. R. Harris, K. J. Millman, S. J. van der Walt, R. Gommers, P. Virtanen, D. Cournapeau, E. Wieser, J. Taylor, S. Berg, N. J. Smith, R. Kern, M. Picus, S. Hoyer, M. H. van Kerkwijk, M. Brett, A. Haldane, J. F. del Río, M. Wiebe, P. Peterson, P. Gérard-Marchant, K. Sheppard, T. Reddy, W. Weckesser,

H. Abbasi, C. Gohlke, and T. E. Oliphant, "Array programming with NumPy," *Nature*, vol. 585, p. 357, 2020.

[125] O. E. Jensen and C. K. Revell, "Couple stresses and discrete potentials in the vertex model of cellular monolayers," *arXiv preprint arXiv:2205.09637*, 2022.

[126] M. F. Staddon, K. E. Cavanaugh, E. M. Munro, M. L. Gardel, and S. Banerjee, "Mechanosensitive junction remodeling promotes robust epithelial morphogenesis," *Biophys. J.*, vol. 117, no. 9, pp. 1739–1750, 2019.

[127] S. Tlili, J. Yin, J.-F. Rupprecht, M. Mendieta-Serrano, G. Weissbart, N. Verma, X. Teng, Y. Toyama, J. Prost, and T. Saunders, "Shaping the zebrafish myotome by intertissue friction and active stress," *Proc. Natl. Acad. Sci. U.S.A.*, vol. 116, no. 51, pp. 25430–25439, 2019.

[128] R. Sknepnek, S. Henkes, I. Djafer-Cherif, and C. J. Weijer, "Generating active t1 transitions through mechanochemical feedback," *arXiv preprint arXiv:2106.12394*, 2021.

[129] J. Comelles, S. Soumya, L. Lu, E. Le Maout, S. Anvitha, G. Salbreux, F. Jülicher, M. M. Inamdar, and D. Riveline, "Epithelial colonies in vitro elongate through collective effects," *eLife*, vol. 10, 2021.

[130] M. Krajnc, T. Stern, and C. Zankoc, "Active instability and nonlinear dynamics of cell-cell junctions," *Phys. Rev. Lett.*, vol. 127, no. 19, p. 198103, 2021.

[131] S. P. Timoshenko and J. M. Gere, *Theory of elastic stability*. MacGraw-Hill, New York, 1961.

[132] L. Landau and E. Lifshitz, *Statistical Physics: Volume 5*, vol. 5. Elsevier, 2013.

[133] H. Lan, Q. Wang, R. Fernandez-Gonzalez, and J. J. Feng, "A biomechanical model for cell polarization and intercalation during drosophila germband extension," *Physical biology*, vol. 12, no. 5, p. 056011, 2015.

[134] G. B. Blanchard, A. G. Fletcher, and L. J. Schumacher, "The devil is in the mesoscale: mechanical and behavioural heterogeneity in collective cell movement," in *Seminars in Cell & Developmental Biology*, vol. 93, pp. 46–54, Elsevier, 2019.

[135] G. Zhang, R. Mueller, A. Doostmohammadi, and J. M. Yeomans, "Active intercellular forces in collective cell motility," *Journal of the Royal Society Interface*, vol. 17, no. 169, p. 20200312, 2020.

[136] X. Li, A. Das, and D. Bi, "Mechanical heterogeneity in tissues promotes rigidity and controls cellular invasion," *Phys. Rev. Lett.*, vol. 123, no. 5, p. 058101, 2019.

[137] M. Serra, S. Streichan, M. Chuai, C. J. Weijer, and L. Mahadevan, "Dynamic morphoskeletons in development," *Proceedings of the National Academy of Sciences*, vol. 117, no. 21, pp. 11444–11449, 2020.

[138] A. Logg, K.-A. Mardal, and G. Wells, *Automated solution of differential equations by the finite element method: The FEniCS book*, vol. 84. Springer Science & Business Media, 2012.

[139] A. Goriely, *The mathematics and mechanics of biological growth*, vol. 45. Springer, 2017.